Measurement of the $t\bar{t}$ Production Cross-Section at $\sqrt{s} = 1.96$ TeV Using Lifetime Tagging

by

Alexander Khanov

Submitted in Partial Fulfillment
of the
Requirements for the Degree
Doctor of Philosophy

Supervised by

Professor Regina Demina

Department of Physics and Astronomy
The College
Arts and Sciences

University of Rochester
Rochester, New York

2004

Curriculum Vitae

The author was born in Moscow, Russia, on September 12, 1966. He attended Moscow Physical and Technical Institute from 1983 to 1989, and graduated with a Master of Sciences degree in 1989. He entered the Kansas State University in the Spring of 2000 and began graduate studies in Physics. He moved to the University of Rochester in the Summer of 2003, and pursued his research in Experimental High Energy Physics under the direction of Professor Regina Demina. He received a full tuition scholarship, a research assistantship, and a Marshak Fellowship of the Department of Physics and Astronomy.

Acknowledgments

I wish to express my deepest gratitude to Professor Regina Demina for convincing me to enter graduate school after so many years since my M.S. degree, giving me a chance to work in the greatest experiment I could think of, guiding me through the whole analysis, and always being ready to offer any kind of help I needed.

I am very grateful to the University of Rochester for providing me an opportunity to accomplish this project.

I thank people of DØ and the Tevatron for making my work possible.

I thank DØ top group conveners for pushing the analysis, and especially Lisa Chabalina for her immense help and numerous contributions. This work is built upon a huge effort of many people in the group, and I would like to thank them all.

I thank DØ b-id group and Mark Strovink for their close attention and encouragement for the development of the CSIP tagging algorithm, the core of my analysis.

I thank DØ tracking group, members of the Tracking Algorithm Recommendation Committee, and personally Gaston Gutierrez and Valentin Kuznetsov for their efforts towards excellent DØ tracking.

I thank the Kansas State University and the KSU High Energy Physics group for a wonderful experience of studies at a U.S. graduate school.

And finally, I thank my parents and my wife Flera for their love and support.

Abstract

A measurement of the $t\bar{t}$ production cross section in the lepton+jets channels with the DØ detector at $\sqrt{s}$ =1.96 TeV using the lifetime-tagging techniques is presented. The $t\bar{t}$ cross section is estimated from the combination of the e+jets and μ+jets channels. The obtained result $\sigma_{t\bar{t}} = 7.47^{+1.22}_{-1.14}\,(\mathrm{stat})\,^{+1.65}_{-1.03}\,(\mathrm{syst})\,\pm 0.49\,(\mathrm{lumi})\,\mathrm{pb}$ is consistent with the Standard Model expectation.

Contents

List of Figures

List of Tables

Chapter 1

The Standard Model

The “Standard Model” [1, 2, 3] is the name for a theoretical framework which includes the theory of strong interactions (Quantum ChromoDynamics or QCD) and combined theory of weak and electromagnetic interactions. Together, the two theories describe the world as made of few fundamental particles that interact due to exchange of force carriers.

As known from quantum mechanics, there are two types of particles – fermions and bosons, distinguished according to their spin (intrinsic angular momentum). Fermions, particles with half-integer spin, aggregate in systems with totally asymmetric wave functions, while bosons, particles with integer spin, make systems with symmetric wave functions.

According to the Standard Model, the nature splits responsibilities between fermions and bosons in a very clear way: fermions constitute the building blocks of matter and bosons mediate the forces between them. There are two kinds of fundamental fermions: leptons and quarks. The quarks are subject to strong, weak, and electromagnetic interactions, and leptons are only involved in the weak and electromagnetic interactions.

There are six varieties of leptons and six corresponding quarks, all of them being spin 1/2 fermions. They can be combined in pairs, referred to as “generations”. There are six leptons: three of them with a mass and an electric charge (electron e, muon μ, and tau τ), and three with a very small mass and without electric charge (electron-neutrino ν_e, muon-neutrino ν_μ, and tau-neutrino ν_τ). There are then six quarks: (u)p/(d)own, (c)harm/(s)trange, and (t)op/(b)ottom. Only the first generation particles are stable, others quickly decay into them. The lepton and quark properties are summarized in Table 1.1.

The force carriers are represented by spin 1 bosons (called gauge bosons). The electromagnetic force is transmitted by photons γ. The weak force is transmitted by three intermediate vector bosons W^+, W^-, and Z^0. Finally, the strong force occurs due to gluons g. The properties of the gauge bosons are summarized in Table 1.2.

Other particles (mesons and baryons) appear to be built of quarks bound together with gluons. The mesons are combinations of a quark and an antiquark, and baryons are made of three quarks.

Mathematically, both QCD and electroweak theory are gauge field theories meaning that the Lagrangian in both theories is invariant under gauge transformation that can be associated to a particular symmetry group. From this point of view, gauge bosons pose as field operators acting on fermion wave functions. The property associated with the weak interaction (and affected by $W^{\pm}$ operators) is called isospin. The electroweak theory treats differently left-handed and right-handed fermions: the left-handed fermions form isospin doublets ((e^L,ν_e^L),(u^L,d^L), etc) while the right-handed ones are isospin singlets (e^R,ν_e^R,u^R,d^R, etc).

The quarks and gluons cannot be observed as individual particles: as they are pulled apart, the energy of the strong field becomes big enough to force a quark-antiquark pair production. As a result, an emitted quark (or gluon) undergoes what is called fragmentation. The result of the fragmentation is a stream of collinear particles with the total momentum close to the one of the original quark (gluon). Such an object (called a “jet”) is what is observed in particle detectors. An important exception is the case when the quark is very heavy, as it will be discussed in the next chapter.

The Standard Model has been by now carefully tested in many experiments and was found capable of predicting a vast range of phenomena. An excellent review of the Standard Model cornerstones as well as experiments that have confirmed it can be found in [4].

G1	G2	G3	charge
leptons			
e m=0.511 MeV	μ m=105.7 MeV	τ m=1.78 GeV	-1
ν_e m<3 eV	ν_μ m<0.19 MeV	ν_τ m<18.2 MeV	0
quarks			
u m=1.5-4.5 MeV	c m=1-1.4 GeV	t m=178.0 GeV	+2/3
d m=5-8.5 MeV	s m=80-155 MeV	b m=4-4.5 GeV	−1/3

Table 1.1: Three generations of matter particles in the Standard Model.

	charge	mass
g (gluon)	0	0
γ (photon)	0	0
$W^{\pm}$	±1	80.4 GeV
Z	0	91.2 GeV

Table 1.2: Force carriers in the Standard Model.

Chapter 2

The top quark

The top quark is the sixth quark in the Standard Model. It is the heaviest one, with the mass of an atom of gold.

2.1 The top quark discovery

The journey towards the top quark began in 1973 when a three generation scheme was proposed by Kobayashi and Maskava in order to explain CP violation in the $K^0\bar{K}^0$ system [5]. Soon after that the Υ states were discovered, and the fifth quark, b, was introduced [6].

The existence of the sixth quark became obvious soon after the discovery of the bottom quark. The most prominent evidence came from the observation of the forward-backward asymmetry in $e^+e^- \to Z/\gamma \to b\bar{b}$ process that is sensitive to the

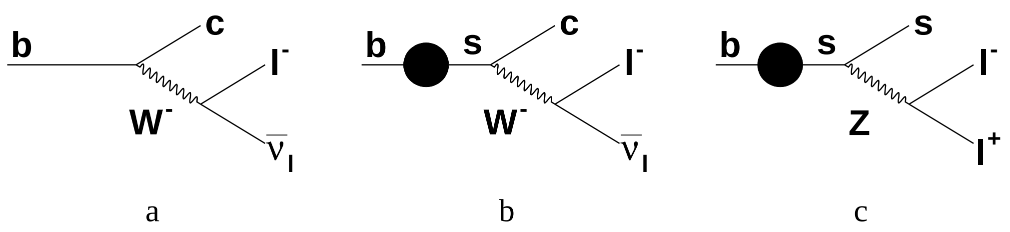

Figure 2.1: The Feynman diagrams describing the *b*-quark decay in the Standard Model (a) and in the case when the *b*-quark is an isospin singlet (b,c).

isospin of the left-handed and right-handed *b*-quarks. Combining this result with the measurement of a partial $Z \rightarrow b\bar{b}$ production width, the third component of the isospin for the left-handed and right-handed *b*-quarks was found to be close to -0.5 and 0, respectively, which according to the Standard Model indicated presence of a quark doublet, the *b*-quark being one of its components [7].

An additional proof came from comparison of production rates for the $b \rightarrow cl^+l^-$ and $b \rightarrow sl^+l^-$ processes. If the *b*-quark were an isospin singlet, it could not decay into *c*-quark and a lepton pair through a standard weak process shown in Fig. 2.1, a. The only possibility would be that *b*-quark converts (“mixes”) to a lighter quark which, being an isospin doublet, decays weakly (Fig. 2.1, b). But in this case there should exist another process (Fig. 2.1, c) which would lead to a $b \rightarrow sl^+l^-$ production at a comparable rate [8]. However, such a process (“flavor changing neutral current”) was found to be suppressed by several orders of magnitude[9], which indicated that *b* is a part of a doublet.

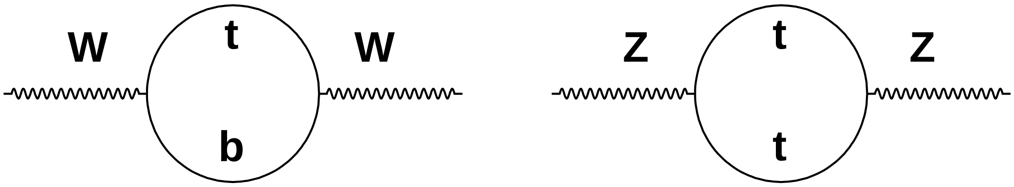

Figure 2.2: The Feynman diagrams describing radiative corrections to the W- and Z-boson production.

Indirect evidence of the top quark came from radiative corrections to masses of gauge bosons. In the Standard Model, the ratio

$$\rho = \frac{M_W^2}{M_Z^2 \cos^2 \theta_W} \tag{2.1}$$

in the Born approximation is equal to 1. Here M_W, M_Z are masses of gauge bosons, and θ_W is the Weinberg angle – an important parameter of the electroweak theory describing the mixing of gauge bosons. In the presence of diagrams shown in Fig. 2.2 this ratio acquires a correction proportional to the squared mass of the top quark [10]. Unfortunately the precision to which ρ is known is limited.

The first collaboration to claim the discovery of the top quark was UA1, who quoted the top quark mass of 40±10 GeV in 1984 [11]. The top quark of such mass would be produced in W decays. This result, however, was not confirmed, and in 1990 a lower limit $m_t >$91 GeV was set, ruling out the possibility of the $W \to t\bar{b}$ process [12, 13]. In 1994, the CDF experiment at the Tevatron claimed a 3σ

evidence [14], and finally, in 1995 both CDF and DØ announced the discovery of the top quark with the mass 174 GeV [15, 16].

2.2 The $t\bar{t}$ production cross section in the Standard Model

At the Tevatron energies ($\sqrt{s}$=1.96 TeV) the top quarks are produced mostly in pairs. The motivation of precise measurement of the $t\bar{t}$ production cross section $\sigma_{t\bar{t}}$ is three-fold. If consistent with the theoretical predictions, it would verify the Standard Model. It would be even more exciting though, if a significant inconsistency with the Standard Model were observed. This would imply a new physics either in the production (a presence of a $t\bar{t}$ resonance) or in the top quark decay. Finally, a detailed understanding of the $t\bar{t}$ production can be extrapolated to the future high energy physics projects. At the Large Hadron Collider [17], in particular, $t\bar{t}$ will be a dominating background to many interesting physics processes including production of a Higgs boson [18], the most interesting and not yet discovered object directly related to the origin of the mass. Considering that many of these channels show up as an excess over the background, the knowledge of $\sigma_{t\bar{t}}$ is essential.

Because the top quark is heavy, the $t\bar{t}$ production cross section in the QCD can be calculated perturbatively, meaning that the cross section is developed as a series of powers of α_s, the effective QCD coupling parameter. It must be mentioned here that this approach in QCD is usually difficult because the integrals diverge. The problem is attacked through regularization (introducing an integrating cut-off) and renormalization (eliminating dependency of calculated quantities on the cut-off value by absorbing it into redefinition of the quark masses and coupling parameters). As a consequence, α_s becomes dependent on the choice of the renormalization scheme. Since the mass of the top quark is much higher than the typical QCD scale $\Lambda_{QCD} \sim 0.2$ GeV (the energy at which α_s becomes large and expansion series no longer converge), the perturbative approach works well (but calculations are still involved).

The lowest order of the perturbative theory (leading order, LO, or Born approximation) already provides a reasonable figure, accounting for 70-80% of the total $t\bar{t}$ production cross section. In the Born approximation, the $t\bar{t}$ production at the Tevatron happens due to two processes: quark-antiquark annihilation $q\bar{q} \to t\bar{t}$ and gluon/gluon fusion $gg \to t\bar{t}$ [19]. The Feynman diagrams describing these processes are shown in Fig 2.3. At the Tevatron energies and the top quark mass of ~175 GeV the quark-antiquark annihilation constitutes about 90% of the total cross section and the rest is coming from the gluon/gluon fusion.

In the early 1990s, the first next-to-leading order (NLO) calculations were performed [20]. However, as first Tevatron data has arrived, it became clear that the theoretical prediction was lower than the measured cross section. The result quoted

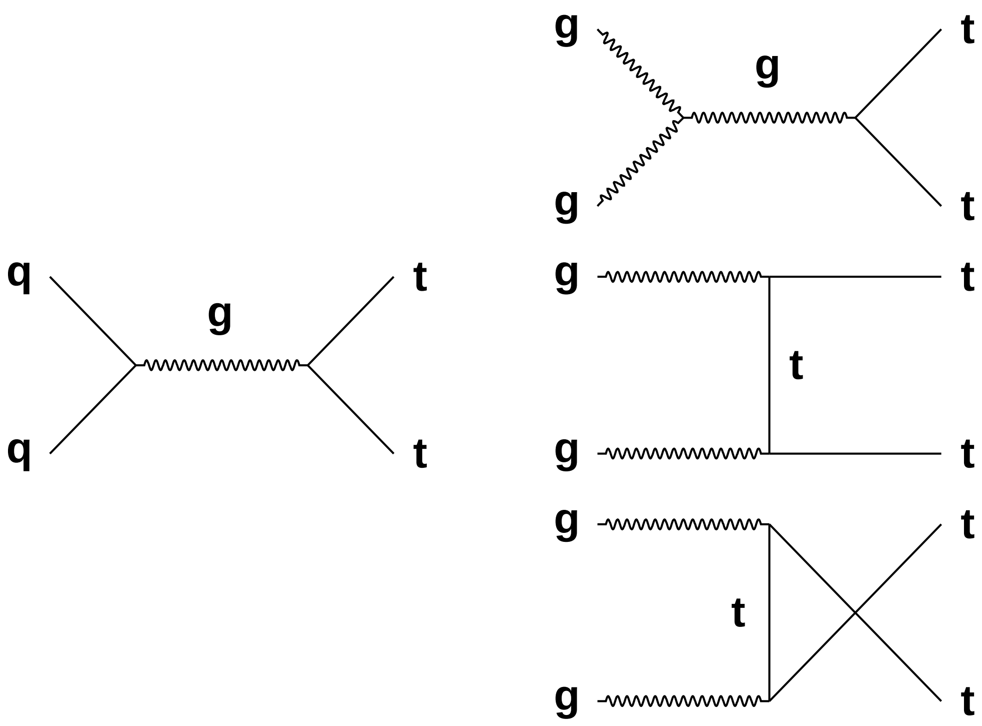

Figure 2.3: The Feynman diagrams describing the leading order $t\bar{t}$ production at the Tevatron: quark-antiquark annihilation (left) and gluon/gluon fusion (right).

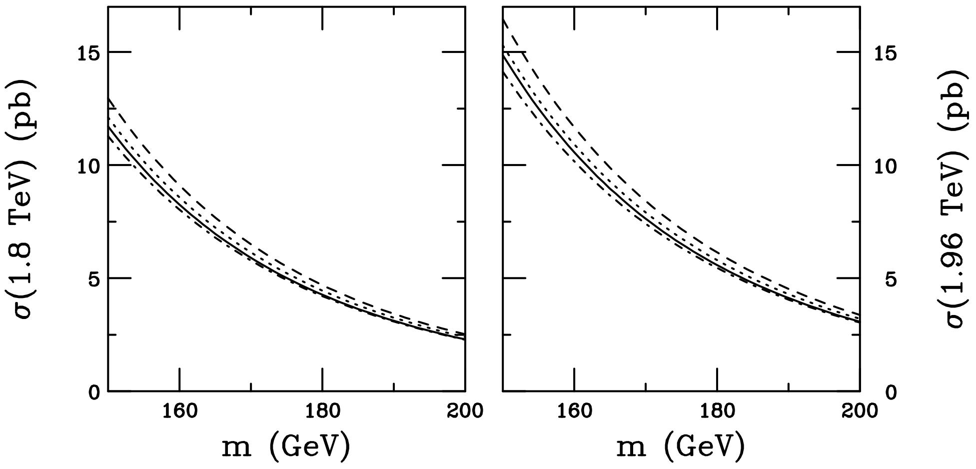

Figure 2.4: The $t\bar{t}$ cross sections in $p\bar{p}$ collisions at $\sqrt{s}$=1.8 TeV (left) and 1.96 TeV (right) as functions of the top quark mass. The NLO (solid) and approximate NNLO (dotted) results are shown together with two calculations for different kinematic models (dashed and dot-dashed lines).

by the Tevatron experiments is 5.7 ± 1.6 pb for DØ and $6.5^{+1.7}_{-1.4}$ pb for CDF [21], and the NLO calculations yielded $\sim$ 5 pb [22]. While the accuracy of the first measurements was not enough to claim inconsistency, many theorists found the excess of experimental results over the prediction disturbing. This led to improved calculations extended to the higher orders. The theoretical prediction for the $t\bar{t}$ cross section is shown in Fig. 2.4 [23] for the center-of-mass energy of 1.8 TeV (left) and 1.96 TeV (right) as a function of the top quark mass. The solid line is the NLO calculation, and the dotted line is the next-to-next-leading order (NNLO) calculation.

Finally, it must be mentioned that the calculated $t\bar{t}$ production cross section depends on the top quark mass. Strictly speaking, a meaningful comparison of the experimental results to the theoretical prediction is only possible for the simultaneous measurement of the mass and the production cross section.

2.3 The top quark decay channels

The full top quark decay width Γ_t calculated in the Standard Model appears to be about 1.5 GeV. This is far above the QCD scale Λ_{QCD}, which implies that the top quark decays before it can bind to other quarks giving rise to hadronic states [24].

In the Standard Model, the top quark almost always decays into a W-boson and a b-quark. The W-boson in turn decays either leptonically (to a lepton and a neutrino) or hadronically (to a quark-antiquark pair). The probabilities for different final states of the $t\bar{t}$ system are summarized in Table 2.1. In accordance with this scheme, the $t\bar{t}$ channels are classified as dilepton (both W decay leptonically), lepton+jets (one W decays leptonically and another one hadronically), and all-jets (both W decay hadronically). Finally, both b-quarks and quarks from W decays (if any) emit radiation and become jets of particles.

The all-jets channel has the highest branching ratio and therefore the largest statistics. Unfortunately it suffers from huge background due to the copious multijet production. Also, it is difficult to develop an effective trigger for this channel. The dilepton channel is the cleanest one and can be easily triggered upon. However, with the present integrated luminosity available from the Tevatron, only few events can be registered due to the low branching ratio. This dissertation concentrates on the study of the lepton+jets channels, where lepton can be either a muon or an electron. These decay modes constitute ∼30% of all decays.

The study of these channels relies on the following components:

- measurement of a high momentum muon (for the μ+jets channel),
- measurement of a high momentum electron (for the e+jets channel),
- measurement of hadronic jets,
- measurement of “missing” energy due to unregistered (anti)neutrino,
- identification of b-jets (“b-tagging”).

The following chapter provides the details on how the DØ detector is suited for this study.

$t\bar{t} \to W^+bW^-\bar{b}$	$W^+ \to c\bar{s}/u\bar{d}$ 6/9	$W^+ \to e\nu_e$ 1/9	$W^+ \to \mu\nu_\mu$ 1/9	$W^+ \to \tau\nu_\tau$ 1/9
$W^- \to s\bar{c}/d\bar{u}$ 6/9	36/81	6/81	6/81	6/81
$W^- \to e\nu_e$ 1/9	6/81	1/81	1/81	1/81
$W^- \to \mu\nu_\mu$ 1/9	6/81	1/81	1/81	1/81
$W^- \to \tau\nu_\tau$ 1/9	6/81	1/81	1/81	1/81

Table 2.1: The $t\bar{t}$ final states and their branching ratios.

Chapter 3

Experimental apparatus

The DØ experiment is located at the world's premier high-energy accelerator, the Tevatron Collider, at the Fermi National Accelerator Laboratory (Fermilab) in Batavia, Illinois, USA. This chapter briefly describes the technical details of the Tevatron collider and DØ detector, with special emphasis on the silicon vertexing system.

3.1 The Tevatron

The Tevatron [25] is a proton-antiproton collider with a center-of-mass energy of 1.96 TeV which is the world highest available energy. The schematic view of the Tevatron is shown in Fig. 3.1.

The production and acceleration of protons and antiprotons is done in several steps that are described below:

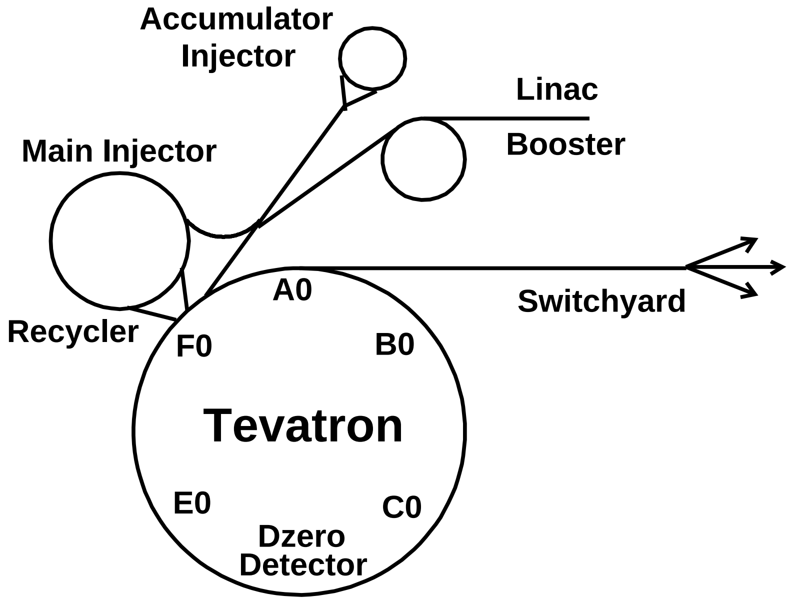

Figure 3.1: Schematic view of the Tevatron.

- H^- ions are accelerated by Cockroft-Walton accelerator to 750 keV;
- H^- ions are accelerated by LINAC (a linear accelerator) to 400 MeV;
- electrons are stripped from H^- ions by carbon foil;
- remaining protons are accelerated by Booster to 8 GeV and inserted in Main Injector;
- protons are accelerated to 120 GeV and impact a nickel target in order to produce antiprotons;
- antiprotons are separated from other secondaries and stored in Accumulator;

- as soon as enough antiprotons have been collected, they are inserted in Main Injector and accelerated to 150 GeV;
- at the same time, protons are accelerated by Main Injector to 150 GeV;
- both protons and antiprotons are inserted in Tevatron and accelerated to 1 TeV.

The proton and antiproton beam meet at two interaction points (B0 and D0), the DØ detector located at the second one. The interaction vertex is spread along the beam according to a Gaussian distribution with a width of about 25 cm. In transverse plane the distribution is almost circular, with a typical Gaussian width of 15 μm.

3.2 The DØ detector

The DØ detector [26, 28] is shown in Fig. 3.2. It consists of four major systems: the muon system, the calorimeters, the preshowers, and the central tracking. They will be shortly described in the following sections, and then special attention will be given to the inner (vertexing) part of the central tracking system.

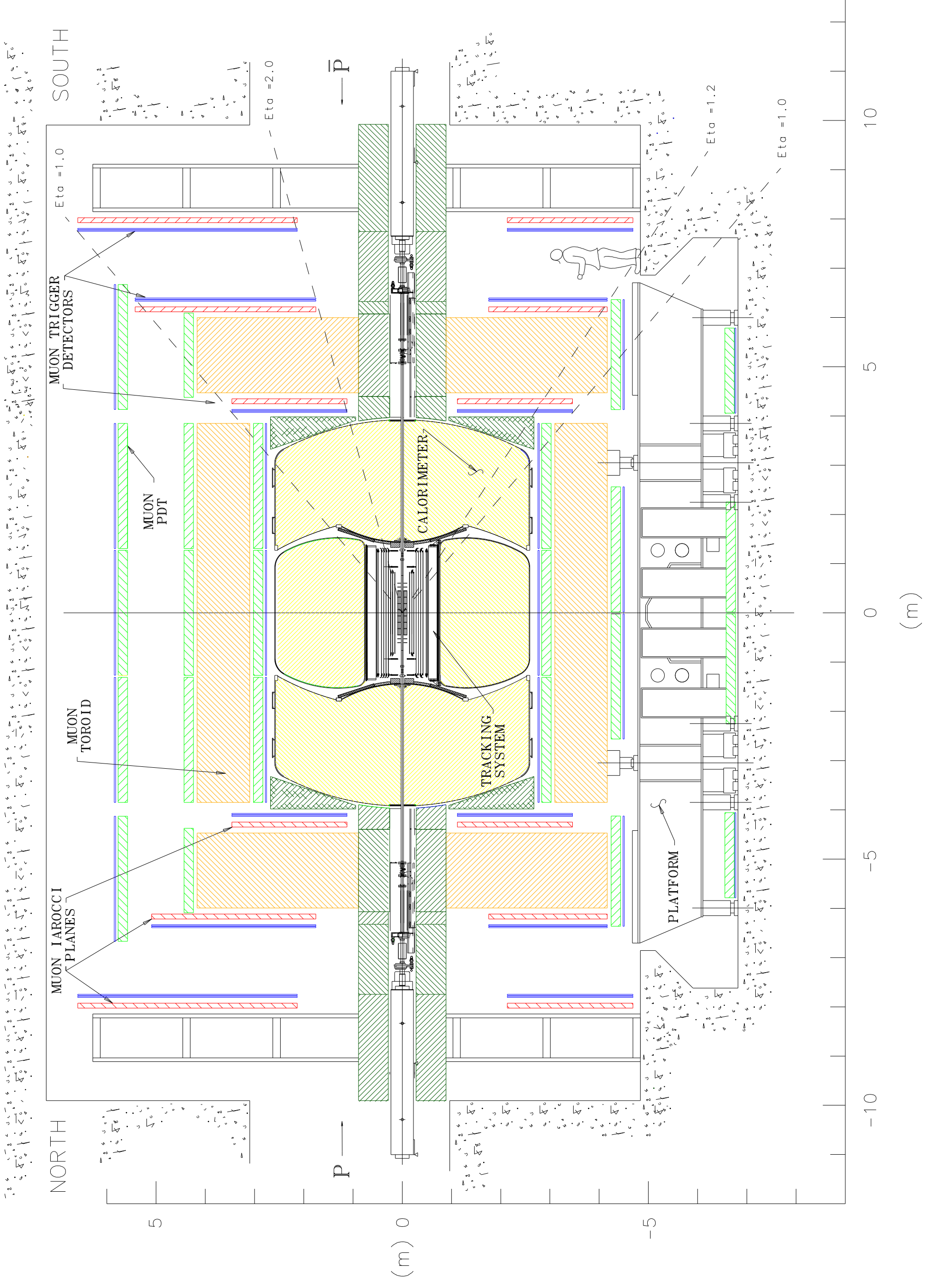

Figure 3.2: Schematic view of the DØ detector.

3.3 DØ coordinate system

The DØ coordinate system [27] is a right-handed Cartesian coordinate system defined such that the z axis points along the outgoing proton beam, the y axis points vertically upwards, and the x axis lies in the horizontal plane, pointing inward toward the center of the Tevatron ring. The origin of the coordinate system lies at the geometrical center of the Central Fiber Tracker (described below).

The azimuthal angle φ is calculated according to

$$\varphi = \begin{cases} \tan^{-1}(y/x), & x > 0, y > 0, \\ \tan^{-1}(y/x) + \pi, & x < 0, \\ \tan^{-1}(y/x) + 2\pi, & x > 0, y < 0. \end{cases} \tag{3.1}$$

The polar angle θ is defined as $\theta = \cot^{-1}(z/r)$, $r = \sqrt{x^2 + y^2}$. A more often used quantity, pseudorapidity η, is related to the polar angle as $\eta = -\ln(\tan(\theta/2))$, or $\sinh\eta = \cot\theta$.

A difference between two directions (φ_1, η_1) and (φ_2, η_2) is often expressed in terms of ΔR distance defined as follows:

$$\begin{aligned} \Delta R &= \sqrt{\Delta\varphi^2 + \Delta\eta^2}, \\ \Delta\varphi &= \min(|\varphi_1 - \varphi_2|, 2\pi - |\varphi_1 - \varphi_2|), \\ \Delta\eta &= |\eta_1 - \eta_2|. \end{aligned} \tag{3.2}$$

3.4 Magnetic field

The magnetic field in DØ [29, 30] is provided by two systems. A toroid magnet, providing a 1.8 T magnetic field, is split in three subsystems, central and two forward. The central part of the detector is embedded in a 2 T magnetic field generated by a superconducting solenoid, with the field lines in the center parallel to the beam axis. The toroid also serves as a return yoke for the solenoid.

3.5 Muon spectrometer

The DØ muon detector [31, 32] includes central and forward part. The central muon system (WAMUS) covers pseudorapidity region $|\eta| < 1$. It consists of 94 proportional drift tube chambers organized in three layers. Layer A is between the calorimeter cryostat and the toroid magnet, and layers B and C are outside the toroid, which gives a possibility for a momentum measurement. Layer A has four decks of drift tubes and layers B and C each have three decks. The drift tubes are 4×2.5 inch rectangles, about 24 tubes per chamber, the wires being oriented along the magnetic field lines. The drift distance resolution is about 1 mm. The WAMUS also includes an inner layer of scintillators ($A-\phi$ counters) and outer layers of scintillators (Cosmic Cap) used for triggering purposes and cosmic muon suppression.

The forward muon system (FAMUS) consists of mini-drift tubes and pixel scintillators. It covers the region $1 < |\eta| < 2$. The forward drift tubes are 1 cm squares, and they also have time division measurement. The layers and the number of decks are the same as for the central system. The coordinate resolution is 0.7 mm per deck.

Due to bending of muon trajectories in toroidal magnetic field in $r-z$ plane (Fig. 3.4), it is possible to calculate the muon momentum using only information from the muon chambers. The momentum resolution of muon tracks measured in toroids is shown in Fig. 3.3 [33]. It can be parameterized as a function of the muon momentum p according to

$$\frac{\sigma(1/p)}{(1/p)} = \frac{\alpha(p-\beta)}{p} \oplus \gamma p, \tag{3.3}$$

where

$\alpha = 0.36 \pm 0.04$, $\beta = 3.1 \pm 0.2$ GeV, $\gamma = 0.0050 \pm 0.0026$ GeV^{-1}, (central);

$\alpha = 0.21 \pm 0.01$, $\beta = 1.79 \pm 0.16$ GeV, $\gamma = 0.0057 \pm 0.0005$ GeV^{-1}, (forward).

3.6 Calorimeter

Geometrically, the DØ calorimeter system [34, 35] is divided into central part (Central Calorimeter, CC) and two endcap calorimeters (EC). CC is 226 cm long, occupies radii from 75 cm to 222 cm and covers $|\eta|$ up to 1.2. It consists of three layers which

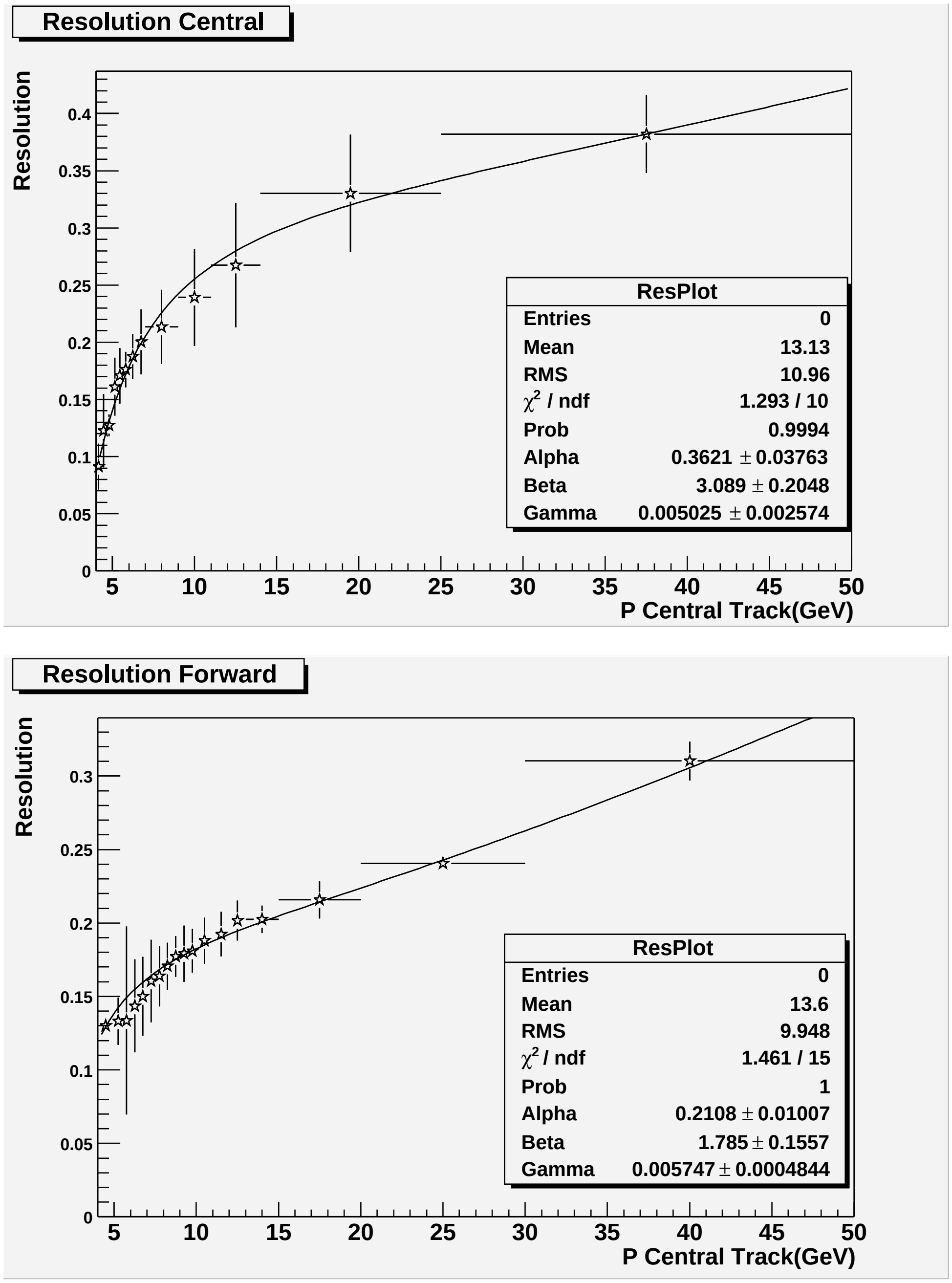

Figure 3.3: The local muon momentum resolution in the central and forward region.

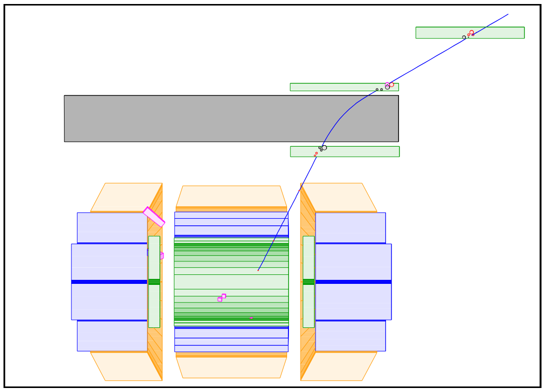

Figure 3.4: A simulation of a muon propagating through the DØ detector.

are made of three types of modules: ElectroMagnetic (EM), Fine Hadronic (FH), and Coarse Hadronic (CH). All modules have the 0.1×0.1 segmentation in $\eta\times\phi$ except for the third layer of the EM module where the 0.05×0.05 segmentation is used.

The end calorimeters extend the η coverage out to 4.5. The segmentation is 0.1×0.1 except for the very forward region ($|\eta| > 3.2$) where it coarsens to 0.2×0.2 and for the third EM layer where it is 0.05×0.05.

The DØ calorimeters are based on the liquid argon as active medium. As an absorber, EM and FH modules use depleted uranium, and CH has copper (CC) or stainless steel (EC) plates. At $\eta=0$, the CC has a total of 7.2 nuclear absorption lengths (λ_A).

The jet energy resolution in the central region ($|\eta| < 0.5$) measured on data from the p_T imbalance of dijet events is shown in Fig. 3.5 [36]. It can be described as

$$\sigma_{p_T}/p_T = \sqrt{C^2 + S^2/p_T + N^2/p_T^2}, \tag{3.4}$$

where

$C = 0.052 \pm 0.008$ %,

$S = 0.902 \pm 0.045$ GeV$^{1/2}$ %,

$N = 0.0 \pm 2.2$ GeV %.

The “raw” energy measured in the calorimeter is not the same as the energy of the original quark (or gluon) that caused the jet. The difference is both due to non-instrumental effects (e.g. loss of energy from low momentum particles that do not reach the calorimeter volume) and non-perfectness of the calorimeter itself. The agreement between the measured and original energy is improved by introducing a correction factor (dependent on the space coordinates of the jet and its raw energy), futher being referred to as *jet energy scale* (Fig. 3.6).

3.7 Preshowers

The preshower detectors [37] function as tracking devices to provide precise position measurement and as calorimeters to assure early energy sampling. They are

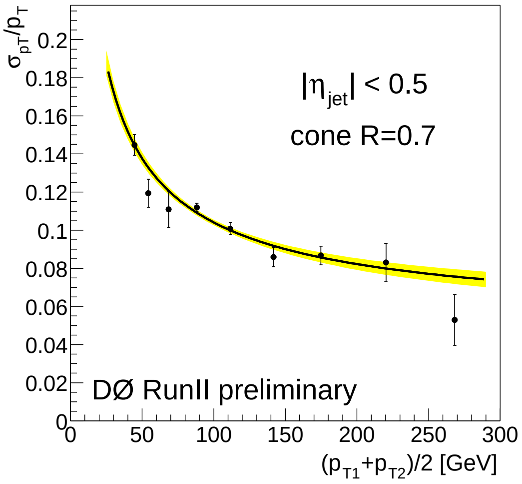

Figure 3.5: The jet energy resolution in the central region ($|\eta| < 0.5$).

positioned in front of CC (Central PreShower, CPS, covering $|\eta| < 1.2$) and EC (Forward PreShower, FPS, covering $1.4 < |\eta| < 2.5$). They are designed to aid electron identification and π^0/γ separation. The information from preshowers has not been used in the present analysis, hence its performance will not be discussed.

3.8 Central tracking system

The tracking in DØ is done inside solenoidal 2 T magnetic field. The central tracking system of DØ consists of two detectors: Silicon Microstrip Tracker (SMT) and Central Fiber Tracker (CFT). The impact parameter resolution for the central tracker

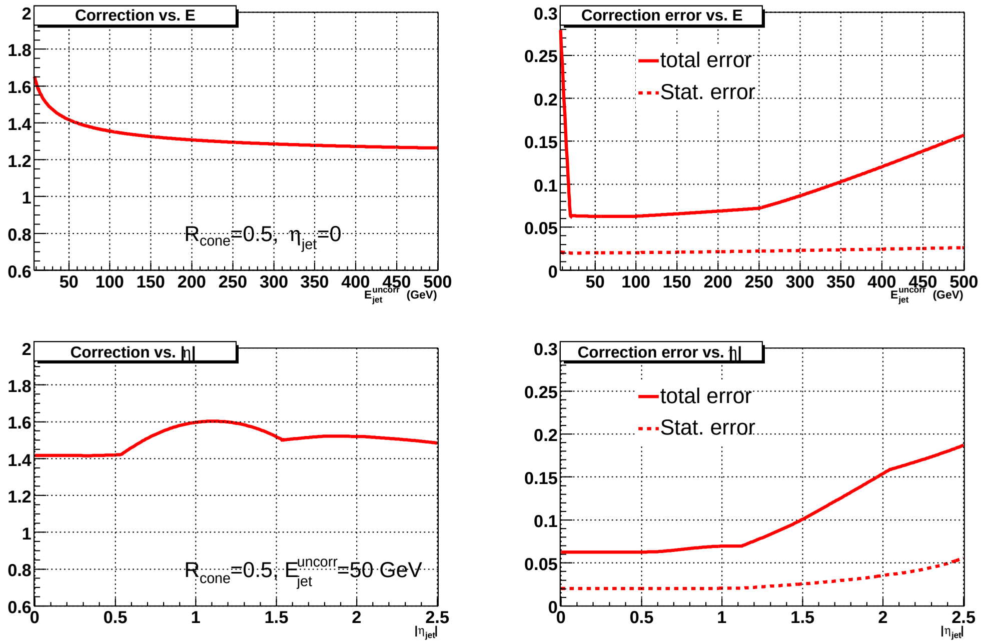

Figure 3.6: The correction factor (left) and its error (right) between raw energy measured in the calorimeter and physical jet energy as a function of jet energy (upper) and $|\eta|$ (lower).

is shown in Fig. 3.7. It can be parameterized as a function of track p_T according to

$$\sigma(d_0) = p_0 + p_1/p_T\,, \tag{3.5}$$

p_0 =8.5 μm p_1 =37.0 μm GeV (Monte Carlo),

p_0 =11.2 μm p_1 =41.8 μm GeV (data).

3.8.1 Central Fiber Tracker

The Central Fiber Tracker [38] provides the outer tracking in the central part of the detector. It is based on scintillating fiber technology with visible light photon counter

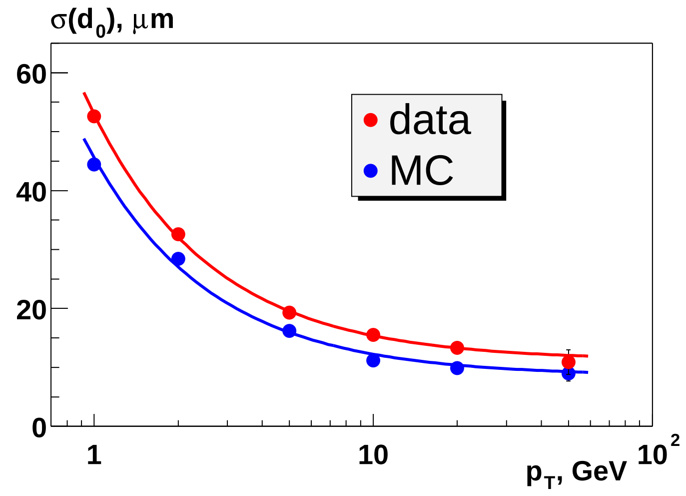

Figure 3.7: The impact parameter resolution in the central region.

(VLPC) readout [40]. CFT consists of eight cylindrical layers positioned at radii from 20 cm to 52 cm. Two inner layers are 166 cm long, and the rest are 252 cm long. The CFT η coverage is shown in Fig. 3.8 for two cases: probability for a track to have hits in all 8 CFT layers (open dots) or in at least 4 out of 8 (filled dots) [41].

Each CFT layer is made of two "doublets" (sub-layers). In each pair of doublets, fibers in the inner doublet are parallel to the beam axis and provide an axial measurement of the track position, while fibers in the outer doublet are placed at a stereo angle (3°) w.r.t. the beam axis, thus in combination with an axial measurement providing a stereo measurement. Each doublet in turn consists of two layers of fibers of 830 μm diameter and 870 μm spacing, offset by a half of the fiber spacing. A track traversing a CFT doublet may hit either one or two fibers thus producing

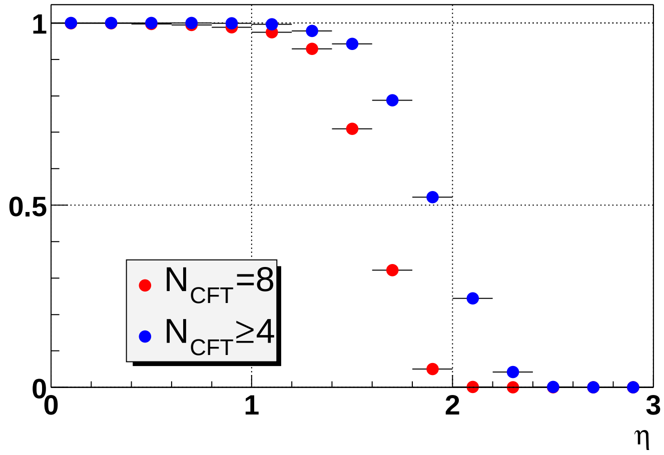

Figure 3.8: Fraction of tracks with 8 and at least 4 CFT hits as a function of track η.

a one- or two-strip cluster. The probabilities to have a one- and two-strip cluster are approximately equal. The signal amplitude is not used (except for the threshold cut-off). Under these circumstances, average hit position resolution in CFT is about 870 μm/4$\sqrt{3}$=125 μm.

3.8.2 Silicon Microstrip Tracker

The Silicon Microstrip Tracker [39] is the inner part of the DØ central tracking system. It provides precise coordinate measurement of the tracks close to the interaction point which is essential in establishing that tracks are coming from decays of long-lived particles. The quality of the measurement depends strongly on the level at which the SMT performance is understood. The correct assignment of errors to the tracks is very important because it makes the basis of all subsequent algorithms and ultimately determines the analysis quality.

The general view of SMT is shown in Fig. 3.9. Geometrically SMT consists of six barrels interleaved with disks (*inner F-disks*). Each barrel is equipped with eight layers of silicon detectors (ladders) organized in four super-layers (referred to as L1, L2, L3, L4 in the order of increasing radius). The SMT barrel layers are positioned at radii from 2.7 cm to 10 cm. The barrel structure provides almost hermetic φ coverage in the central region. However, the SMT barrel part is relatively short (last inner F-disk positioned at 38 cm) compared to the interaction point z spread (σ=25 cm). SMT also has six *outer F-disks* (at $|z|$=43 cm, 48 cm, and 53 cm) and four *H-disks* (at $|z|$=100 cm and 121 cm). This allows SMT to register tracks up to $|\eta| \sim 3$.

Due to its complicated design, and also because the barrel part of SMT is rather short, the SMT η coverage varies significantly with track η and z. In practice it is important to consider two characteristics:

- probability for a track to have at least 2 SMT hits, and therefore a good spatial resolution. For tracks with only one SMT hit the pattern recognition studies show that in many cases this hit is erroneously taken from another track or from noise, so the best strategy in this case is to drop this single SMT hit from a track. The tracks without SMT hits are still useful for the measurement of high p_T isolated leptons and for reconstruction of K_S and Λ decay products

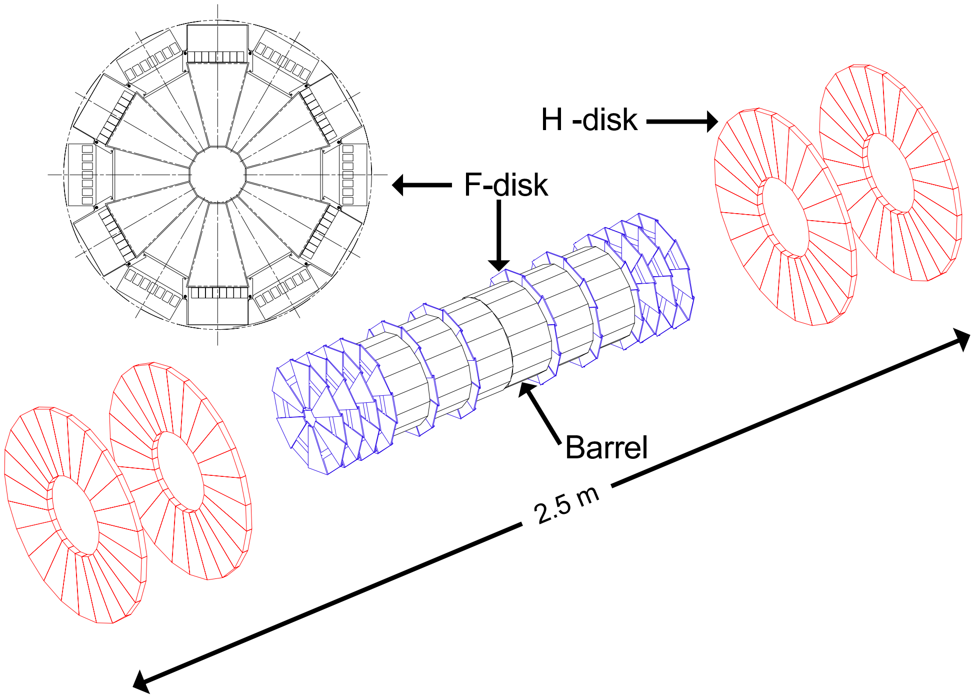

Figure 3.9: View of the SMT detector.

and γ conversions, however, they are impractical for vertexing and heavy flavor identification;

- probability for a track to have at least 4 SMT hits. This is a bare minimum for a track to be reconstructed using only SMT information (without or with only partial support from CFT). It is the only possibility to reconstruct tracks in the forward region, outside the CFT coverage (see Fig. 3.8).

The SMT η coverage curves for the two cases discussed above are shown in Fig. 3.10. The SMT coverage is worst at $\eta = 0$ where tracks escape disks and can fall outside SMT barrel or in cracks between barrels. These curves do not take into account dead SMT detectors.

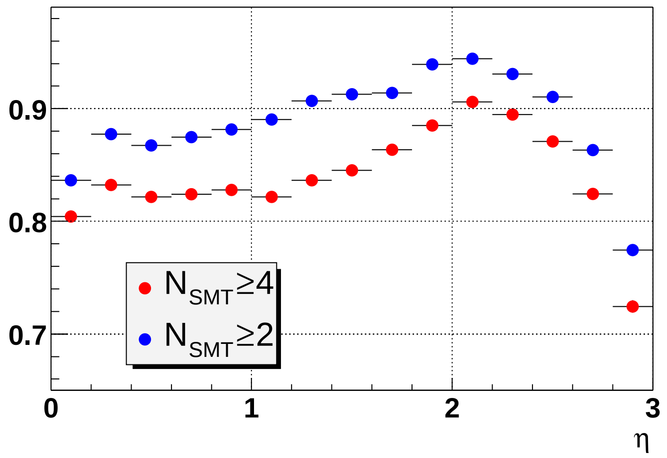

Figure 3.10: Fraction of tracks with at least 2 and at least 4 SMT hits as a function of track η.

3.8.3 SMT detectors

A silicon microstrip detector principle of operation is as follows [47, 48]. When an ionizing particle enters the detector medium, it produces electron-hole pairs along its path. In absence of external electric field these pairs immediately recombine. When an electric field is applied, it separates electrons and holes: the former drift towards the anode (positive electrode), the latter drift towards the cathode (negative electrode). The result is a pulse of charge proportional to the total energy deposited by the penetrating particle, which is detected by a charge-sensitive amplifier attached to the detector.

Electronically, an SMT detector (Fig. 3.11) is a semi-conducting p^+n-diode made of n-type silicon with p-type implants on the detecting side. These implants are made very narrow and covered with aluminum strips to provide the read-out. The space separation between adjacent strips is called pitch.

If no electric field is applied, the area near the junction (p-) side is enriched by charge carriers due to doping (presence of atoms of elements other than silicon). These carriers must be removed by applying negative voltage to the junction side (called reverse-bias). As a result, the bulk of the detector gets depleted (free of floating carriers). The higher the bias voltage, the bigger the depleted area, and at some point it expands through the whole detector volume, thus providing maximum operating efficiency ("full depletion"). Normally the SMT detectors are slightly over-depleted.

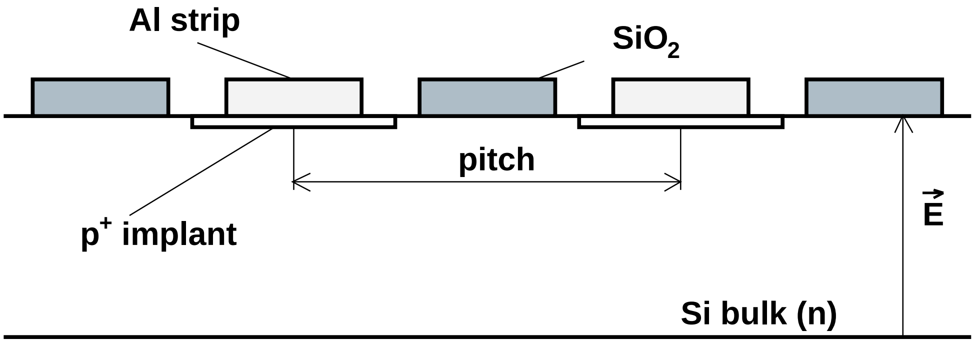

Figure 3.11: A sketch of a silicon microstrip detector.

The charge produced due to ionization is eventually collected by one or several adjacent strips that form a cluster. The SMT clusters are characterized by their total charge, number of strips, and distribution of charge among individual strips (η-function).

While the *p*-side is always equipped with strips, the *n*-side can be done in a number of ways. The simplest (and most robust) way is to make this side as a single electrode (single-sided detectors). Other possibility is to introduce n^+ implants on the *n*-side and read it out as well. There is a modification of this scheme when the *n*-side is covered first with a single electrode, then with a very thin (few microns) insulation layer, and finally with metal strips (double-sided double-metal detectors). Strips on the *n*-side are typically placed at an angle with respect to the *p*-side (called a stereo angle). A combination of measurements on *p*- and *n*-side provides a 3-dimensional measurement. The choice of stereo angle value α is motivated by two competing factors. On one hand, a larger stereo angle provides a better resolution in the direction parallel to the strips on the *p*-side (it is proportional to $\cot\alpha$). However, it also leads to higher ambiguities rate. The effect is shown in Fig. 3.12. N tracks passing close to each other may generate as much as N^2 stereo combinations, only N of them being real.

The DØ SMT barrels are equipped with rectangular shape detectors (*ladders*) of three different types. Layers L2 and L4 have double-sided detectors with axial

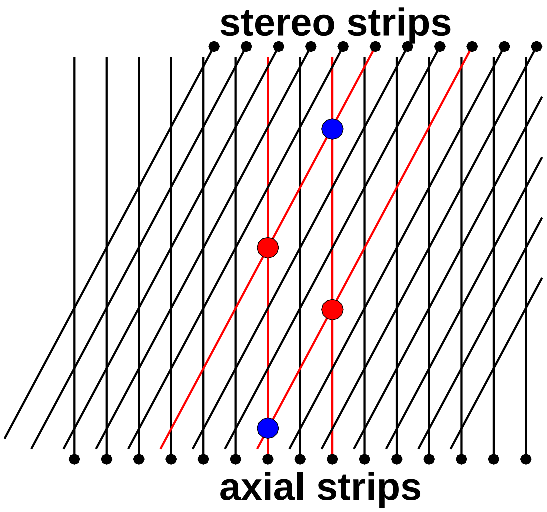

Figure 3.12: Ambiguities in the stereo SMT detector due to several (here two) tracks passing close to each other. Two tracks penetrating the detector near red dots create two clusters on axial side and two clusters on stereo side (shown as red lines). Combining the two pairs of clusters, one gets two ”true” hits (red dots) as well as two ”fake” hits (blue dots).

(parallel to the beam) strips on the *p*-side and stereo strips (at 2° angle with respect to strips at the *p*-side) on the *n*-side. Layers L1 and L3 are equipped with single-sided detectors (barrels 1 and 6) and with double-sided double-metal detectors with stereo angle of 90° (barrels 2 through 5). Each F-disk module has 12 wedge shaped double-sided detectors with a 30 degree stereo angle, and each H-disk module has 24 single-sided wedges arranged in pairs where strips on two adjoint detectors make an angle of 15°. The SMT detector parameters are summarized in Table 3.1.

The single-sided detectors provide an axial (φ) measurement. The (DS,2°) detectors provide a stereo ($\varphi - z$) measurement on most of their surface except a small

	barrels			disks	
	SS	DS, 90°	DS, 2°	F-wedges	H-wedges
total # detectors	48+96	96+192	144+288	144	384
length	6 cm			7.5 cm	14.262 cm
width, min	2.12 cm		3.4 cm	1.670 cm	2.761 cm
width, max	–			5.692 cm	6.478 cm
p-side strip pitch	50 μm			51.76 μm	64.7 μm
n-side strip pitch	–	156 μm	62.5 μm	64.7 μm	–
read out chips/det	3	3+3	5+4	8+6	6+6

Table 3.1: The detector types used in SMT. The pitch size for wedges is given at the outer edge.

corner where due to strip layout only axial measurement is available. The (DS,90°) detectors give a stereo measurement with very accurate z component; however, in addition to the “natural” hit ambiguities discussed above, there is a duplication of z measurements caused by multiplexed read-out (so that each hit poses as two hits offset by a fixed distance equal to a half-length of the detector).

3.8.4 The SMT detector response

The distribution of the total cluster energy E normalized to the traversed particle path is characterized by its most probable value A and Landau width w. It is described by a Landau distribution density function [42]

$$\varphi(E) = \frac{1}{2\pi i}\int_{c-i\infty}^{c+i\infty} exp\left(\frac{E-A}{w}\varepsilon + \varepsilon ln\varepsilon\right) d\varepsilon,\ c > 0, \tag{3.6}$$

convoluted with a zero centered Gaussian with variance σ. As about 3.6 eV is required to create an electron-hole pair, the most probable value of A for a minimum-ionizing particle in a 300 μm thick silicon detector is about 23000 electron-hole pairs. This number has to be converted to the ADC counts. For DØ SMT detectors, the typical values in ADC counts are $A = 25$, $w = 3$, and $\sigma = 3$. Fig. 3.13 shows Landau distributions in data and Monte Carlo obtained for the p-side of 2° detectors [43].

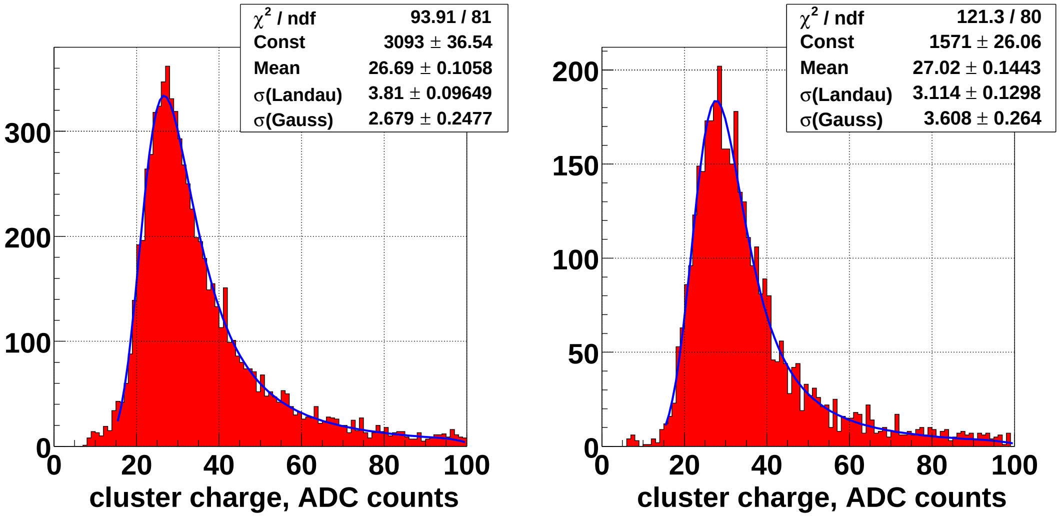

Figure 3.13: The Landau distribution for SMT clusters in data (left) and simulation (right).

The number of strips in a cluster, to first order, corresponds to the detector area "seen" by a particle. This geometrical picture has to be corrected for the cross-talk effect: due to capacitive coupling between adjacent strips, a fraction of charge "leaks" to the neighboring strips and clusters become wider. Additional widening of clusters is due to finite size of the ionization cloud and emission of low momentum electrons

(δ-rays) along the particle trajectory.

The η-function for 2-strip clusters with strip charges q_1 and q_2 (in read-out order) is defined as a ratio of charge on a left strip to the total cluster charge, that is, $\eta = q_1/(q_1+q_2)$. It is determined by the same effects as the cluster size. The ionization cloud increases during the charge drift, and this leads to an asymmetric η-function for inclined tracks. For 3+ strip clusters, the η-function can be determined choosing the pair of consequent strips with the biggest total charge.

Since the SMT detectors are placed in a 2T magnetic field, the charge drift due to electric field is accompanied by a Lorentz shift. Effectively this means that all hit positions are systematically shifted by $\Delta x_L = \Delta w \tan(\theta_L)$, here Δw is the detector thickness (300 μm) and θ_L is the Lorentz angle. The cluster parameter distributions (number of strips, η behavior) as functions of track incident angle are (to the first order of approximation) symmetric around θ_L. In particular, the fraction of 1-strip clusters reaches its maximum at $\theta = \theta_L$, as shown in Fig. 3.14, left, which can be used to measure the Lorentz angle in data. This measurement has been made, and the Lorentz angle in 2° detectors, p-side was found to be $(5.14\pm0.05 \text{ stat})^\circ$ (Fig. 3.14, right) [44].

The SMT detector response has been studied in detail. It was shown that original DØ Monte Carlo model used for simulations does not properly describe the properties of the cluster characteristics, and in particular the η-function. An improved Monte

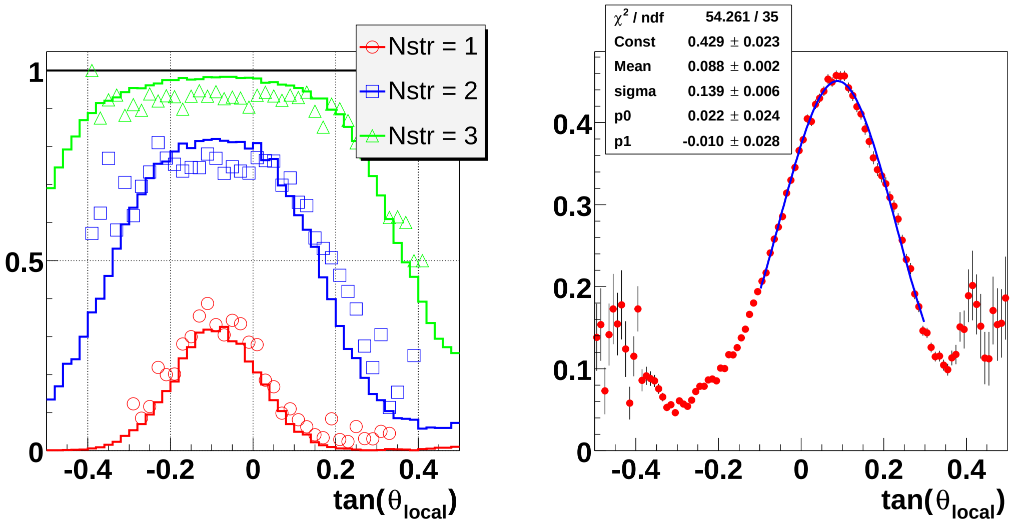

Figure 3.14: The cumulative distributions of a fraction of 1,2, and 3-strip clusters in data (circles, squares, triangles, respectively) and in the proposed Monte Carlo model (solid lines, left); the fit of the maximum position of the fraction of 1-strip clusters in data (right) vs tangent of the local track inclination angle.

Carlo model has been proposed which provides a better description. The new features implemented into this model include tuning of the cross-talk (effect of inducing the charge on the neighboring strips due to interstrip capacity) and a model of the charge cloud development calibrated to the data. As an example, Fig. 3.15 [44] shows η distribution for 3-strip clusters in DØ Monte Carlo model (left) and proposed model (right).

The use of the proposed model is two-fold: first, it allows a realistic simulation of the SMT detector response, and second, it provides a basis for a better estimation of the hit position and its error which is important for pattern recognition and track fit. In particular, the hit position resolution improves if the standard weighted sum of

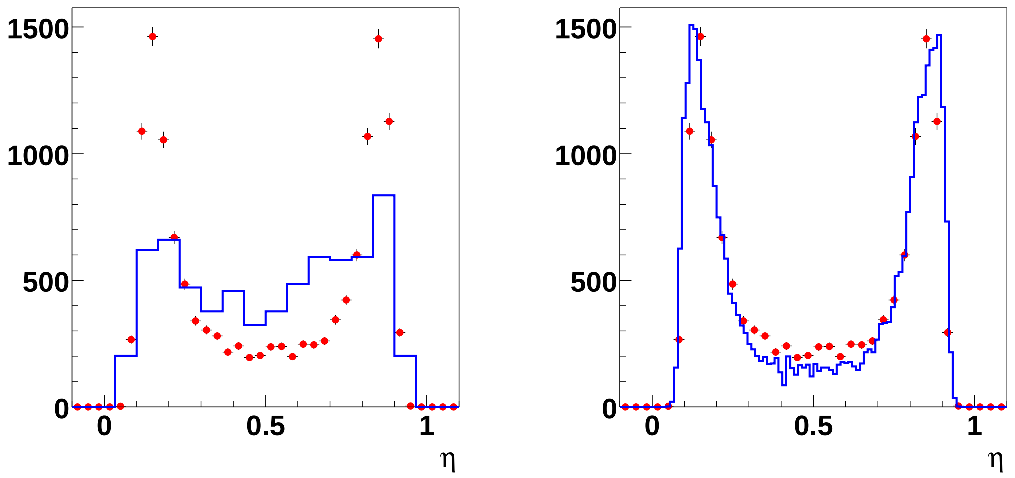

Figure 3.15: The η distribution for 3-strip SMT clusters in standard DØ Monte Carlo model (left) and new model (right) compared to data (red points).

strip positions, $x = x_1 + (x_2 - x_1)(1 - \eta)$, is replaced with [45]

$$x = x_1 + (x_2 - x_1) \int_0^{\eta} \frac{dN}{d\eta'} d\eta'. \tag{3.7}$$

The hit position obtained with the weighted sum deviates from the actual hit position as it shown in Fig. 3.16, left, here the X axis represents the difference between cluster position calculated using weighted sum and “true” hit position. In case of Monte Carlo model (blue points) the true hit position is known from simulation, and in case of data (red points) it is the prediction from the track fit interpolation (given point excluded). The goal is to minimize the deviation using a correction curve similar to the one shown in Fig. 3.16, right. In practice there is a set of correction curves for different track inclination angles, number of strips in the cluster, and detector types. The described functionality has been implemented in the reconstruction code as a look-up table [46].

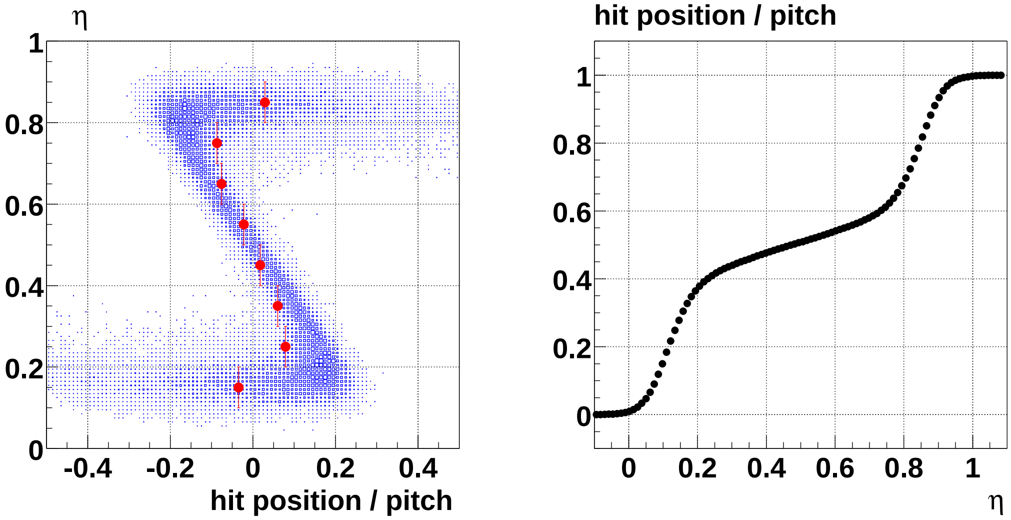

Figure 3.16: The η vs hit position deviation for 2-strip SMT clusters obtained for the Monte Carlo model (blue distribution) and measured on data (red points, left) and the correction curve (right).

Chapter 4

Pattern recognition in the central tracker

The term “pattern recognition in the tracking system” refers to a problem of building tracks out of individual hits. A view of a typical DØ event with reconstructed tracks is shown in Fig. 4.1. Since the number of hits in “busy” events tends to be very large ($10^4 - 10^6$), the problem cannot be solved by brute combinatorial approach. The optimization of the pattern recognition algorithm is very important as it currently consumes more than half of the total DØ event reconstruction time.

The track finding algorithm has to be optimized in view of two distinct problems:

- lepton identification and electron/photon separation require efficient reconstruction and low fake rate for isolated high momentum ($p_T > 20\ GeV$) tracks;

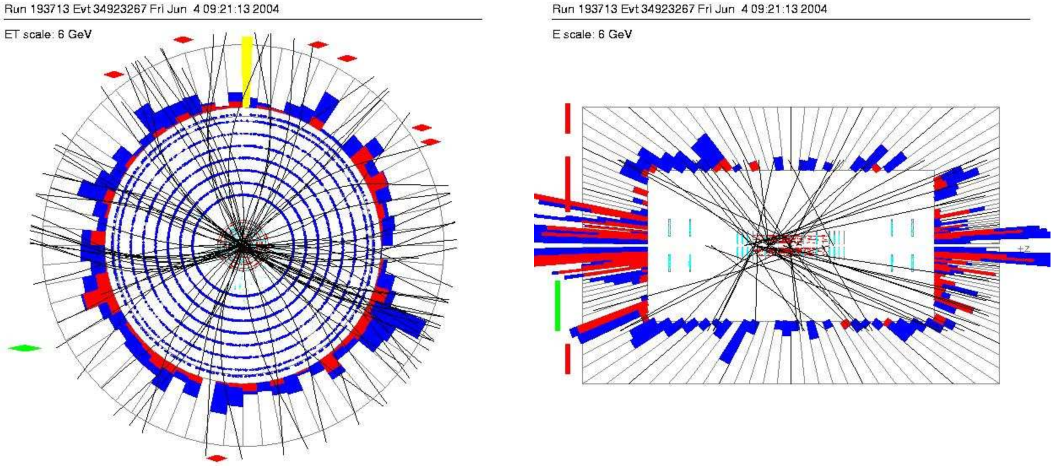

Figure 4.1: A typical DØ event: x-y view (left) and r-z view (right).

- heavy flavor identification requires efficient track finding for relatively low momentum ($p_T > 1\ GeV$) tracks in a dense jet environment.

The pattern recognition in DØ poses a challenging task due to several factors:

- high E_T jets have high local track multiplicity;
- DØ tracking system provides relatively low number of measurements per track, especially in the forward region;
- 3-dimensional tracking is complicated due to the presence of ghost hits, especially in 90° SMT detectors;
- some detectors are non-operating or noisy.

Thus, tracking algorithm must be efficient and fast even in high density environment and it must be robust to noise and detector inefficiencies.

The algorithm developed for DØ tracking, Histogramming Track Finder (HTF) [49], attempts to address these requirements. The details of the algorithm are described below.

4.1 Trajectory parameters

A particle in a uniform magnetic field moves along a helix which can be uniquely described by five parameters P_i. These parameters can be chosen in different ways. A convenient choice is as follows:

- $P_0 =$DCA (distance of closest approach): minimal distance between the helix and the z axis in the x-y plane;
- $P_1 = z_0$: z-position of the particle at the point of closest approach;
- $P_2 = \varphi$: direction of the particle in the transverse plane at the point of closest approach;
- $P_3 = \tan(\theta)$: polar angle of the trajectory;
- $P_4 =$curvature: inverse radius of the trajectory with a sign defined as positive for a right-handed helix and negative otherwise.

The two latter parameters are the same at any point on the trajectory provided the magnetic field is exactly uniform and there is no energy loss due to interaction with material. In reality it is only an approximation, and these parameters, like the rest, are determined at the point of closest approach to the z axis.

The definition based on DCA introduces some ambiguity because a helix approaches the z-axis infinite number of times. In practice only the first half of revolution of a particle is considered, and the point of closest approach is the one that is closest to the particle origin.

4.2 The track finding algorithm description

HTF consists of two successive steps, histogramming preselection and road finding. The first step, based on the Hough transform technique [50], attacks the combinatorics by preselecting groups of hits (track candidates, or templates) of relatively small size. Those groups are later searched for tracks using a Kalman filter [51] based local road finder.

The idea of a Hough transform is as follows. A trajectory originating from (0,0) in transverse plane can be described as

$$\rho r = 2\sin(\phi - \phi_0), \tag{4.1}$$

here ρ is a track curvature, ϕ_0 is track direction at the origin, and (r,ϕ) are polar coordinates of trajectory points. All trajectories passing through a given point in coordinate space correspond to a curve in parameter space (ρ,ϕ_0), as it is illustrated in Fig. 4.2. Vice versa, all parameter space curves corresponding to different trajectory points intersect in one point which gives the parameters (ρ,ϕ_0) of this trajectory. In practice, since hit coordinates are known with finite precision, tracks originate not exactly from (0,0), and due to the multiple scattering and energy loss, the parameter space curves become error bands of finite width. In order to find the intersection of these bands, the parameter space is quantized, that is, divided in (ρ,ϕ_0) cells. For each cell, a counter is introduced which gets increased for each band overlapped with this cell. A trajectory on n points exhibits itself as a peak (local maximum) of height n. Each cell keeps track of hits contributing to it, so sets of hits contributing to peaking cells can be taken as track candidates. The number of operations needed to fill the cells is linearly proportional to the number of hits.

The described method is known to work very well for the case of significant number of hits per track. In DØ however, in some cases (forward SMT tracking), tracks as short as only of 4 hits have to be reconstructed. For such short tracks it is not practical to search for peaks in the histogram, because they are swallowed by combinatorial background. Instead, all cells with four or more entries are considered, and neighboring cells are combined into clusters. Further filtering of such clusters is performed using patterns in (z,r). Finally, the found track candidates are filtered and fitted using Kalman filtering.

The HTF includes two passes. The first pass begins with SMT-only tracks and then tries, if possible, to extrapolate them into CFT. The second pass first builds tracks in CFT and then extrapolates them into SMT. The former pass can find tracks with at least four SMT hits, and the latter one can find tracks with at least seven CFT hits. Together, the two passes provide some redundancy which helps to increase tracking efficiency.

4.3 Track finding performance in Monte Carlo

A pattern recognition algorithm is characterized by track finding efficiency and fake rate. The track finding efficiency ε_{eff} is defined as the ratio of the number of real reconstructed tracks to the total number of tracks in a sample. The fake rate ε_{fake} is the ratio of the number of fake tracks to the total number of reconstructed tracks.

In order to apply these definitions, one needs to distinguish between real reconstructed tracks and fakes. This is done using track matching procedure. Two matching methods have been considered: matching by hits and matching by pulls. A reconstructed track is matched to an original track by hits if more than half of its hits came from this track. A match by pulls is achieved if

$$|P_i^{reco} - P_i^{true}|/\sigma_i < d^{max},\ i = 1\ldots5, \tag{4.2}$$

here P_i^{reco} are reconstructed track parameters, P_i^{true} are original track parameters (known from Monte Carlo), σ_i are reconstructed track parameter errors obtained from the fit, and d^{max} is the matching tolerance (chosen to be 10). A track is considered a fake if it does not match any original track. It may happen that more than one reconstructed track is matched to the same original track. These extra tracks (called "ghosts") also contribute to the fake rate, however their rate is much lower than the rate of unmatched tracks.

The typical track finding efficiency and fake rate in Monte Carlo is shown in Figs. 4.3, 4.4 respectively. Here matching by pulls has been used. The track finding efficiency is calculated for any tracks, which includes tracks that do not have enough hits to be reconstructed, so it is convoluted with the tracker acceptance, as it is reflected in the η dependence of the track finding efficiency. The fake rate increases for very high p_T tracks for which it is no longer possible to correctly determine the curvature, as it can be seen in the left plot of Fig. 4.3.

4.4 Track finding performance in data

Track finding efficiency and fake rate in data cannot be measured directly since neither the number nor parameters of original tracks are known. The track finding efficiency for high p_T isolated particles can be estimated provided these particles are registered with other detectors. As an example, it can be measured for electrons from $Z \to ee$ decay for electrons detected in the EM calorimeter [52]. In order to ensure that the signal in the EM is coming from a real electron, events with two EM objects are selected where the invariant mass of these objects lies within a Z mass window. One of EM candidates (base) is required to match a track, and the other (probe) is checked for a track match. The ratio of the matched probe EM objects to the total number of events gives the electron tracking efficiency. It includes the EM-track matching efficiency that cannot be completely disentangled using this method. A similar approach can be applied to the $Z \to \mu\mu$ events.

The high p_T isolated lepton track finding efficiency is shown in Fig. 4.5 as a function of the lepton transverse momentum for electrons (left) and muons (right). For muons, the results of the data measurement are compared to the Monte Carlo. The efficiency approaches 90% for electrons and 95% for muons at high p_T. The lower efficiency for electrons can be attributed to the radiation of photons (bremsstrahlung).

The methods to estimate fake rate of tracks in data are based on analysis of their

DCA significance (the ratio of DCA to its fitted error). These estimations are discussed in detail in relation to the *b*-tagging which is introduced in the following chapter.

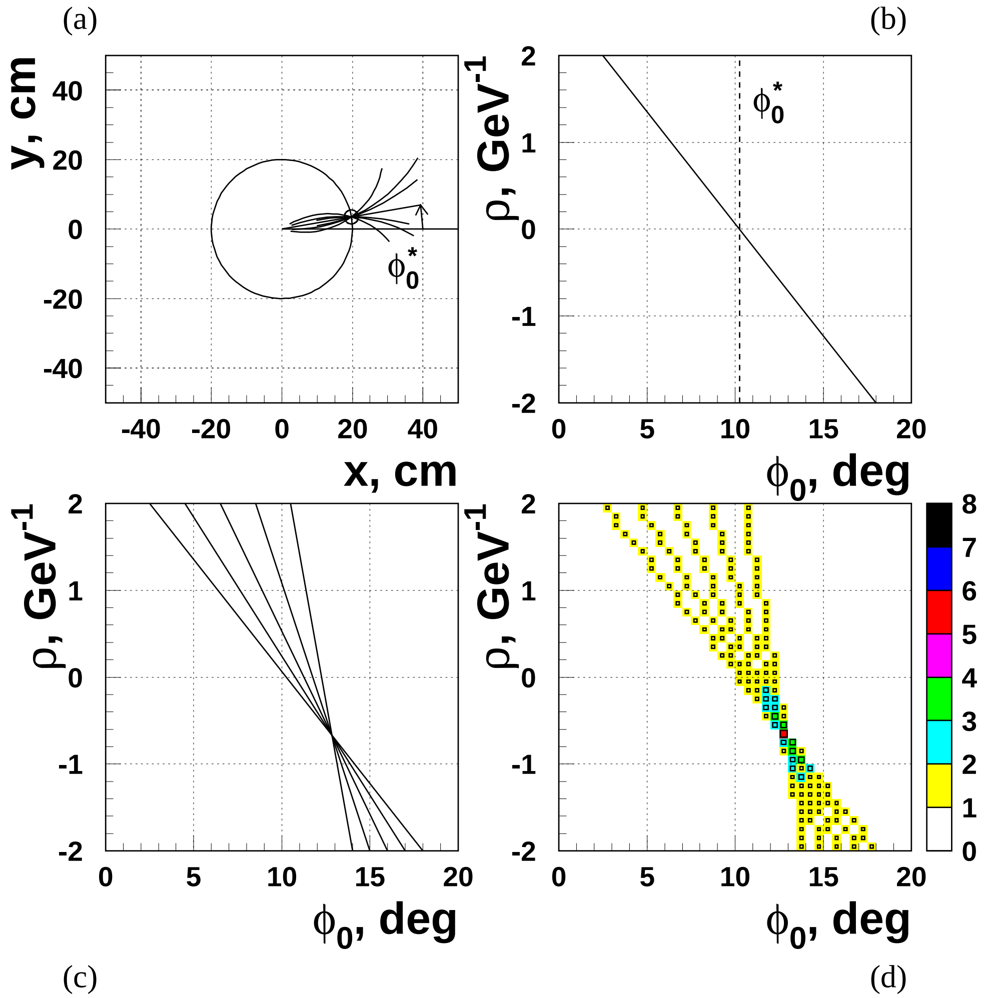

Figure 4.2: The histogramming technique shown for an example of a single track with p_T =1.5 GeV of 5 hits. (a): a set of zero-originating trajectories containing a given hit in coordinate space. (b): a curve in parameter space describing such trajectories. (c): curves from different hits intersect at one point corresponding to the track parameters. (d): the point of intersection corresponds to a peak in a (ρ,ϕ_0) histogram.

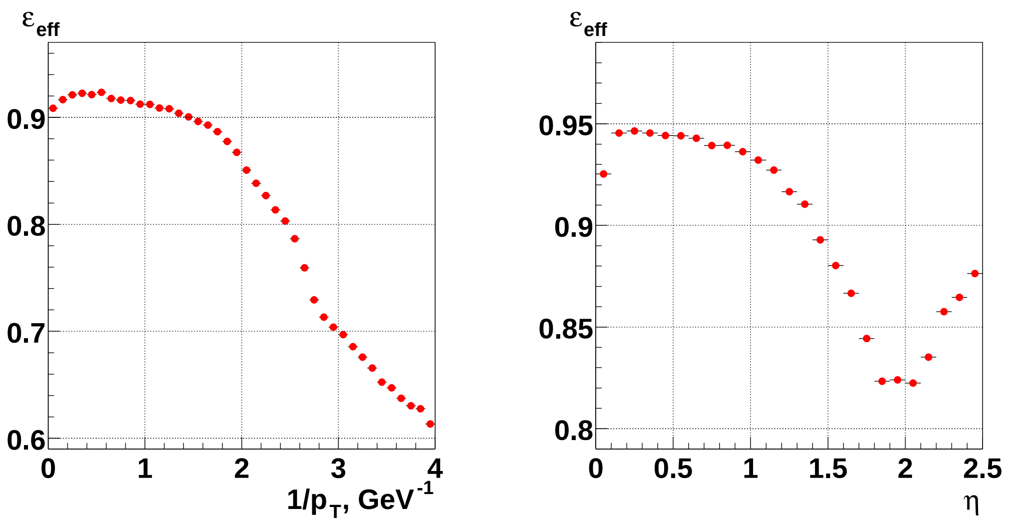

Figure 4.3: The track finding efficiency for all tracks in QCD Monte Carlo as a function of track inverse p_T (for all tracks with $|\eta| < 2.5$, left) and $|\eta|$ (for all tracks with p_T >0.5 GeV, right).

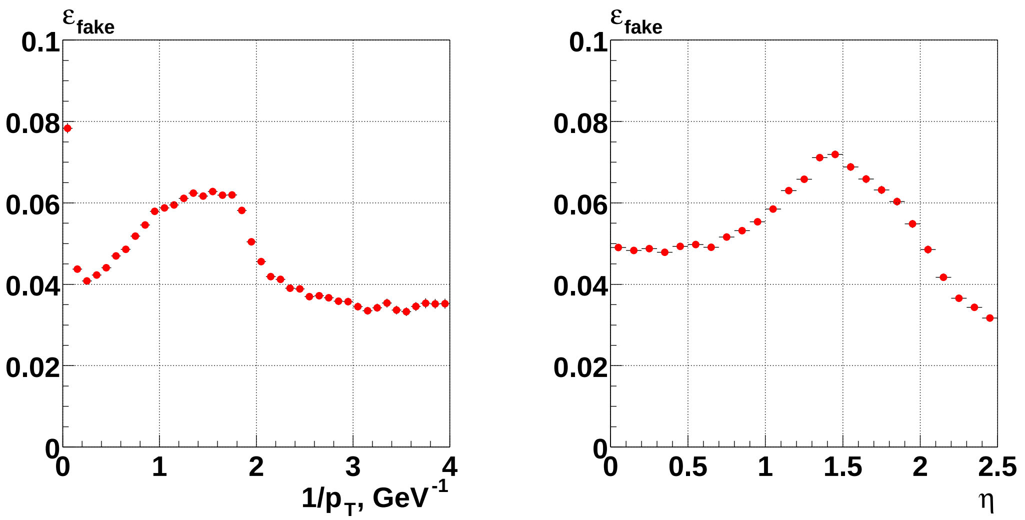

Figure 4.4: The fake rate for all tracks in QCD Monte Carlo as a function of track inverse p_T (for all tracks with $|\eta| < 2.5$, left) and $|\eta|$ (for all tracks with p_T >0.5 GeV, right).

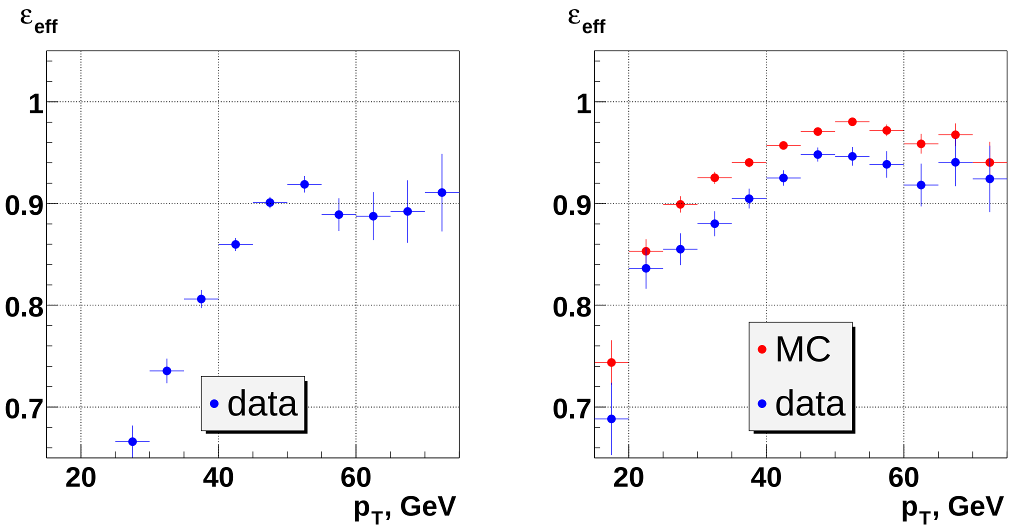

Figure 4.5: The track finding efficiency for high p_T isolated leptons in $Z \longrightarrow ee$ (left) and $Z \longrightarrow \mu\mu$ (right) events.

Chapter 5

b-tagging

The goal of the jet tagging is to separate jets originating from light quarks (*u*,*d*,*s*) and gluons (“light” jets) from jets originating from heavy quarks (*b* and *c*). As *b*-jets are of particular interest, the jet tagging will be often referred to as *b*-tagging. The output from a jet tagging procedure is a single logical value which is set to *true* if the jet is tagged and to *false* otherwise.

b-tagging efficiency ε_{btag} is defined as the ratio of the number of tagged *b*-jets to the total number of *b*-jets in a sample. If jets are considered in bins of jet parameters, such as transverse energy E_T and pseudo rapidity η, *b*-tagging efficiency becomes a function of these parameters: $\varepsilon_{btag} \equiv \varepsilon_{btag}(E_T, \eta)$. *b-jet tag rate function* is a probability for a given *b*-jet to be tagged. According to the weak law of large numbers, the *b*-tagging efficiency approaches the tag rate function as the sample size increases, so both will be referred to as ε_{btag}. The same kind of functions can be defined for *c*- and light jets. In the latter case, the probability to tag a light jet is called *mis-tagging rate*.

The *b*-tagging efficiency and mis-tagging rate are directly related to each other. The goal is to maximize *b*-tagging efficiency while preserving mis-tagging rate as low as possible. By varying the parameters of a *b*-tagging algorithm one can gain in efficiency by the price of increasing mis-tagging rate. The dependence of the mis-tagging rate on the *b*-tagging efficiency is called *performance curve*.

Both *b*-tagging efficiency and mis-tagging rate depend on jet characteristics. The jet tagging probabilities will be considered as functions of jet E_T and η. The dependence is assumed to be factorizable, so that $\varepsilon(E_T,\eta) = C\varepsilon(E_T)\varepsilon(\eta)$. The normalization factor C is calculated so that the total number of predicted tags obtained as a sum of products of the number of events in each (E_T,η) bin N_{ij} and $\varepsilon(E_T,\eta)$ is equal to the total number of tagged events in the sample N^{tag}:

$$\begin{aligned}
&N^{tag} = \sum_{ij}\varepsilon(E_T^i,\eta^j)N_{ij}\\
&E_T^i = E_T^{min} + (E_T^{max} - E_T^{min})(i+0.5)\\
&\eta^j = \eta^{min} + (\eta^{max} - \eta^{min})(j+0.5).
\end{aligned} \tag{5.1}$$

The factorizability is cross-checked by comparing the actual number of tagged events versus jet E_T and η to the value predicted from the tag rate function. This cross-check is called *closure test*.

The *b*-tagging efficiency and mis-tagging rate is different in the data and the Monte Carlo simulation due to various detector effects not properly taken into account in the simulation. Therefore the analysis relies as much as possible on efficiencies measured in data and corrected by scale factors derived from Monte Carlo.

In the rest of the chapter, the algorithm used for the *b*-tagging is described, and its performance on various Monte Carlo and data samples is evaluated. The details of the performance evaluation procedure and description of samples can be found in [53].

5.1 The *b*-tagging algorithm description

The *b*-tagging procedure described below relies on the fact that heavy flavor particles have significant life time (1.54 ps for a B_0 meson, corresponding to a mean flight path of 462 μm [21] that is further increased if the particle has significant momentum). Therefore products of *b*-decays are displaced with respect to the point of proton-antiproton collision, further referred to as a primary vertex. One possible way to address the problem is to attempt to reconstruct secondary vertices inside a jet [54]. This approach requires very good understanding of the vertex reconstruction performance and high secondary vertex reconstruction efficiency. In addition, many *b*-decays involving neutral particles cannot be reconstructed in that way.

The explicit reconstruction of secondary vertices is avoided in the method which is described below. For each track in a jet, a new parameter called signed impact parameter significance is introduced:

$$S = sd_0/\sigma(d_0), \tag{5.2}$$

where

- d_0 is the track DCA (distance of closest approach) to the beam. The latter is defined as a straight line parallel to the z axis of the detector with (x,y) position as the one of the reconstructed primary vertex;
- $\sigma(d_0)$ is the DCA error (square root of the diagonal element of the full 5×5 track error matrix at the DCA point);
- s is the sign of the projection of the DCA point onto the jet axis in transverse plane (Fig. 5.1, left).

The basic idea of the method called Counting Signed Impact Parameter (CSIP) tagging [55] is that tracks originated from secondary vertices inside the jet cone have a positive projection of their DCA point onto the jet axis, while tracks coming from the primary vertex have a zero projection. In presence of measurement errors this transforms to the S distribution which is symmetric around zero, with a variance of one. Cutting on the positive side of the S distribution one can separate tracks from b- and c-decays from the primary tracks.

The distribution of reconstructed tracks in S in Monte Carlo is shown in Fig. 5.1, right. A clear excess of tracks with large positive S from b-jets with respect to the same distribution for tracks from light jets is observed.

The steps of CSIP are as follows:

1. select "good" tracks inside the jet (within $\Delta R < 0.5$ from the reconstructed jet axis);
2. a jet is tagged if it has at least two tracks with $S > 3$ or three tracks with $S > 2$.

All "good" tracks are required to originate within 1 cm in z from the primary vertex. In addition, quality cuts are applied. As it will be shown below, the mis-tagging rate is dominated by mis-reconstructed tracks and fakes. In order to optimize the choice of tagging tracks, all tracks were divided into categories according to their fit χ^2/NDF, number of CFT hits, and number of SMT hits. For all categories, the fake rate was estimated as the fraction of tracks with $S < -3$. This fraction was then required to not exceed 0.08. This left tracks with the following characteristics:

- for tracks with $\chi^2/NDF < 3$: all tracks with at least 2 SMT hits;
- for tracks with $3 < \chi^2/NDF < 9$: tracks with at least 4 SMT hits and more than 12 CFT hits, or tracks with at least 5 SMT hits and either no CFT hits or more

than 10 CFT hits;

- tracks with $\chi^2/NDF > 9$ are not allowed.

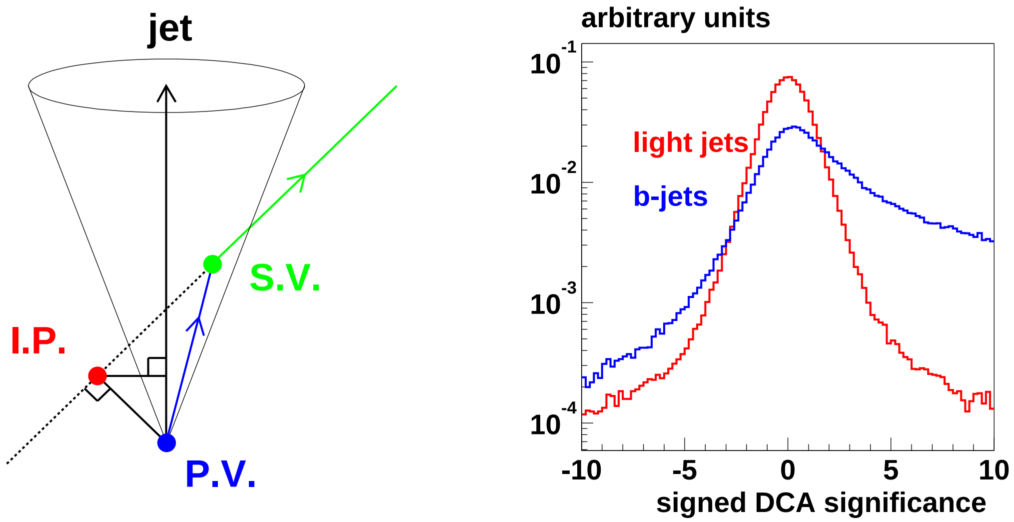

Figure 5.1: Illustration of the CSIP algorithm. Left: sketch of CSIP, right: S distribution for tracks from b- and light jets.

5.2 Sources of mis-tags

Light jets are tagged by CSIP not due to tracks from b decays but due to other tracks with large impact parameters. The primary sources of these tracks are:

- $K_S \rightarrow \pi^+\pi^-$ and $\Lambda \rightarrow p\pi^-$ decays;
- interactions in the material (primarily γ conversions $\gamma \rightarrow e^+e^-$, but also products of nuclear interactions and bremsstrahlung electrons);

- fake tracks (built from hits from other tracks and/or noise).

The presence of these tracks leads to asymmetric distribution in S for light jets as shown in Fig. 5.1.

A simple cut that helps to get rid of most of these tracks is the cut on an absolute value of track DCA: $|d_0| < 0.2$ cm. As K_S and Λ have relatively big decay length (2.7 cm and 7.9 cm, respectively) compared to B-hadrons, and interactions occur in the detector material, i.e. beyond the beam pipe radius (1.9 cm), this cut is very effective.

In addition, CSIP makes use of an algorithm called V^0 filter that reconstructs (and tells CSIP to ignore) tracks from K_S and Λ decays and γ conversions (generally referred to as V^0 decays). The V^0 filter works as follows. Invariant masses of all pairs of opposite sign tracks with $S > 3$ are examined. No cuts on p_T of tracks are applied. If invariant mass of two tracks is within ± 22 MeV mass window around the nominal K_S mass, both tracks are removed from the list of good tracks. As for Λ, mass window of ± 7 MeV around the nominal Λ mass is used to remove the tracks from Λ decays. Examples of the reconstructed K_S and Λ's on data are shown in Fig. 5.2.

For the γ conversions, the tracks in a pair have to satisfy the following additional requirements:

- pull of the angle between tracks in $(r-z)$-plane less than 3;

- distance between trajectories in $(r-\phi)$-plane less than 30 μm;

- invariant mass of two tracks less than 25 MeV.

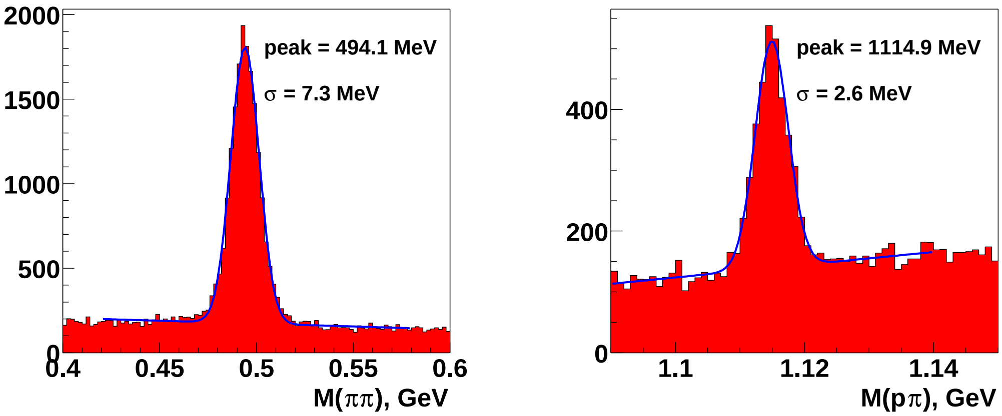

Figure 5.2: Reconstructed K_S (left) and Λ (right) in data.

The remaining mis-tagging rate is dominated by mis-reconstructed tracks from the primary vertex (with $S >3$), as it is shown in Fig. 5.3, left. The next to largest contribution is fake tracks. Other sources include “1-leg” K_S, Λ and conversions (cases when only one of the two decay products has been reconstructed as a track and therefore it is not possible to detect a decay) as well as “2-leg” ones (constituting the V^0 reconstruction inefficiency), and contributions from other sources which are difficult to reconstruct (e.g. τ decays). Among these categories, only primary tracks contribute symmetrically to the distribution Fig. 5.1. For the rest, the fraction of tracks with $S > S_{cut}$ is much larger than the fraction of tracks with $S < -S_{cut}$, as it is shown in Fig. 5.4, where the ratio of these fractions is plotted for different track types as a function of S_{cut}. As a result, the positive tag rate for light jets is always higher than the negative tag rate. The ratio of the two rates is known as a scale factor due to long lived particles, denoted SF_{ll}.

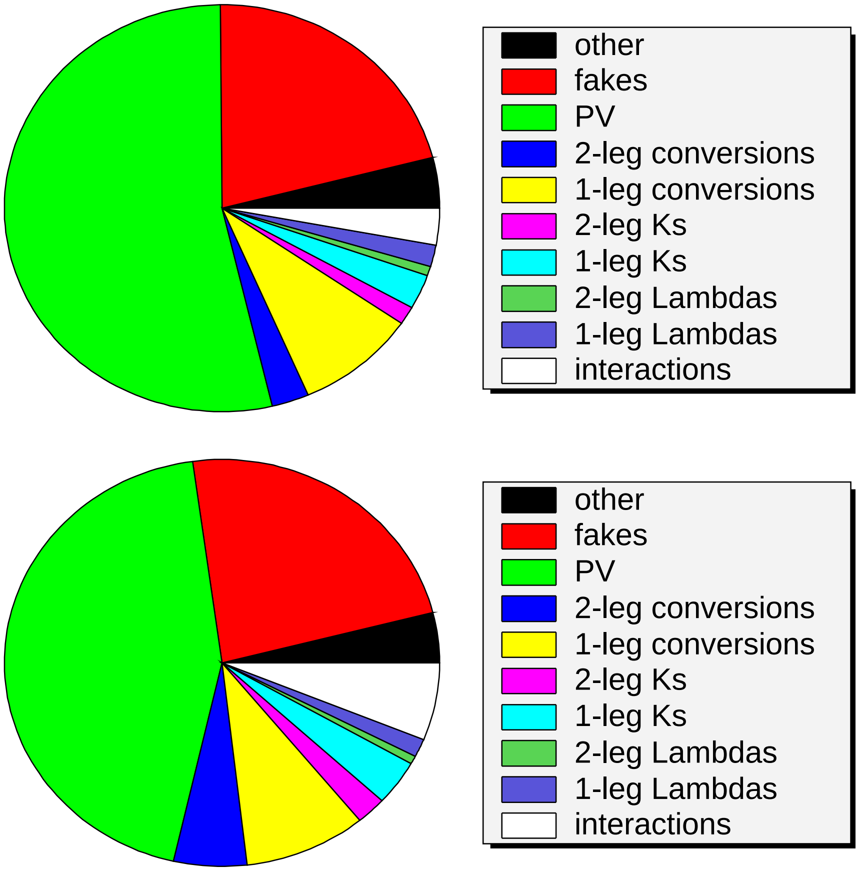

Figure 5.3: Origin of tracks contributing to the negative (upper) and positive (lower) mis-tags in W+4 jets events.

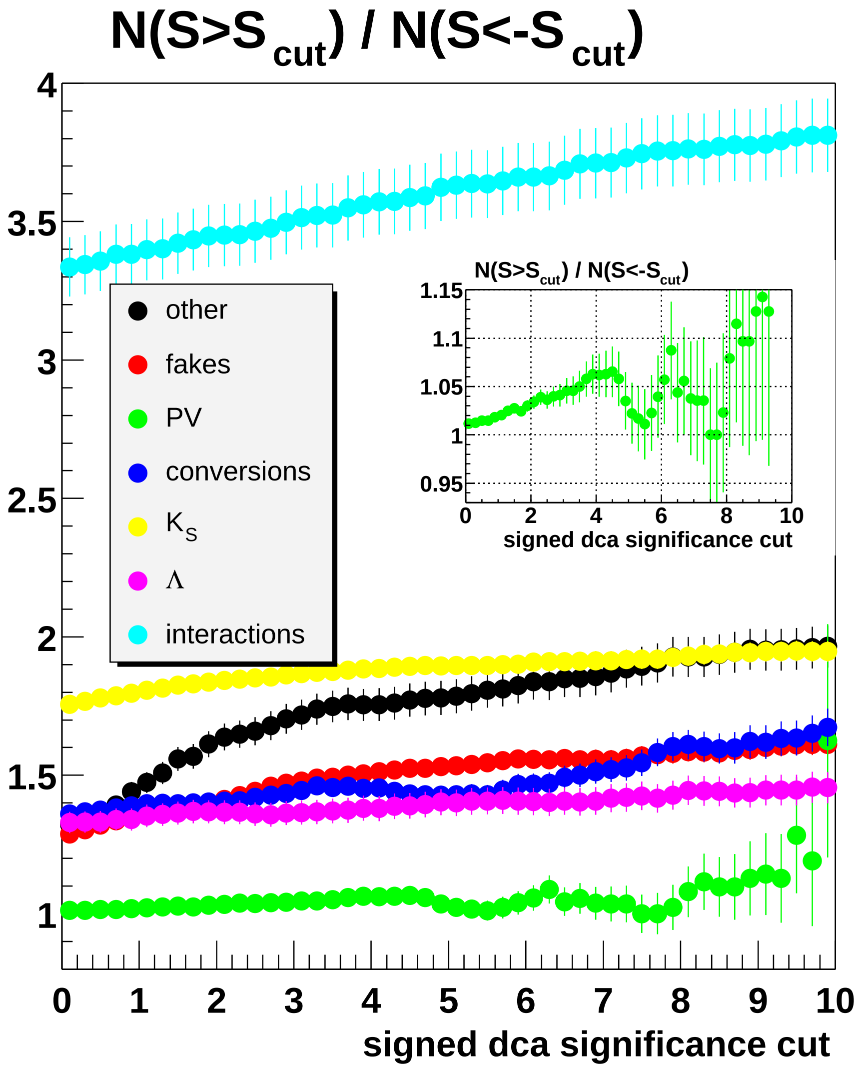

Figure 5.4: Ratio of tracks with $S > S_{cut}$ to tracks with $S < -S_{cut}$ for different track categories as a function of S_{cut}.

5.3 Taggability

The *b*-tagging efficiency and mis-tagging rate depends on the jet quality and data sample. A fake jet made of noisy cells in the calorimeter or a high p_T photon recognized as a jet has no tracks pointing to it and therefore cannot be tagged. The *b*-tagging efficiency is therefore conveniently split in two factors:

$$\varepsilon_{btag}^{raw} = \varepsilon_{tagg}\varepsilon_{btag}, \tag{5.3}$$

where ε_{tagg} (*taggability*) is a probability for a jet to be taggable, and ε_{btag} is a probability for a taggable jet to be tagged.

The definition for taggability is based on a concept of track-jets. A track-jet is an object built out of tracks in a way similar to how a calorimeter jet is built of cells. To find track-jets, one begins with a track of highest p_T. Other tracks are attached to the track-jet if their ΔR distance to the track-jet axis (weighted vector sum of directions of all tracks contributing to the track-jet) is less than 0.5. The tracks are probed in descending p_T order, and the track-jet axis is redefined at each step. After a track-jet is built, the remaining tracks undergo the same procedure until no more tracks are left. A track-jet consists of at least two tracks, the highest p_T track (“seed”) being required to have $p_T >$1 GeV, and other tracks must have $p_T >$0.5 GeV. All tracks must originate close to the primary vertex and have SMT hits.

A jet at η_j,φ_j is considered taggable if there is a track-jet at η_{tj},φ_{tj} within $\Delta R < 0.5$ from the jet axis. The taggability is very different in Monte Carlo and in real data as it is shown in Fig. 5.5, left, where taggability in W+light jet Monte Carlo is compared to taggability in EMqcd data (a multijet sample triggered by a high p_T electromagnetic object). However, as shown in Fig. 5.5, right, the average number of tracks per taggable jet is very well reproduced in Monte Carlo, which suggests that most of effects of low quality jets are incorporated into the taggability. This does not mean that the b-tagging efficiency is the same in data and Monte Carlo, because the quality of tracks is different.

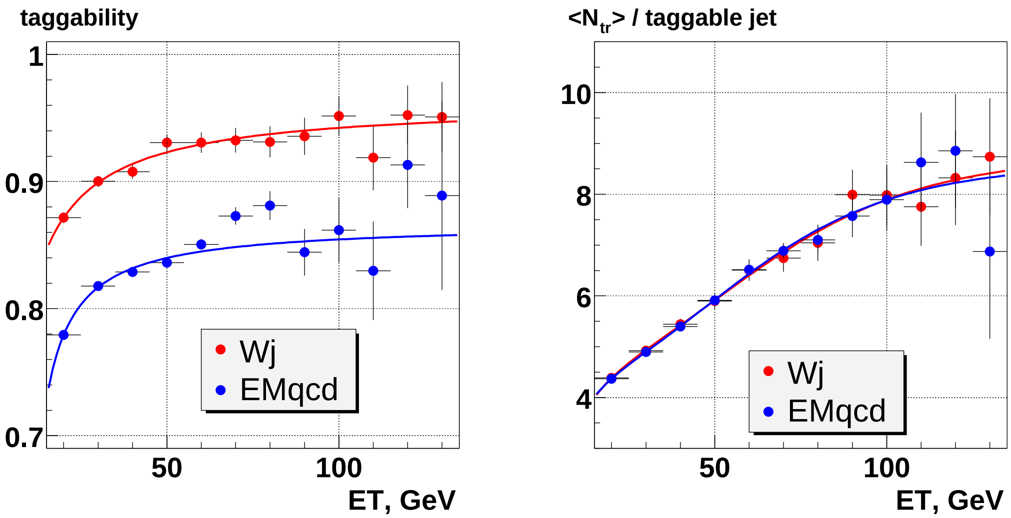

Figure 5.5: Left: taggability as a function of jet E_T in Monte Carlo (W+light jet) and data (EMqcd). Right: average number of tracks per taggable jet in the same samples.

The larger mass of b- and c- quarks compared to the light ones results in higher average track multiplicity for the same E_T. Therefore a higher taggability is expected for heavy flavor jets. This has been demonstrated with the Monte Carlo code. As shown in Fig. 5.6, the difference is most pronounced at low jet energies and vanishes as the energy increases. The flavor dependence of taggability has been derived on a QCD Monte Carlo sample (Fig. 5.6). The taggability used in the analysis is derived on the EMqcd data sample and parameterized *vs* jet E_T and η.

In the rest of the text, ε_{btag} will always refer to the *b*-tagging efficiency with respect to taggable jets. The same applies to mis-tagging rate.

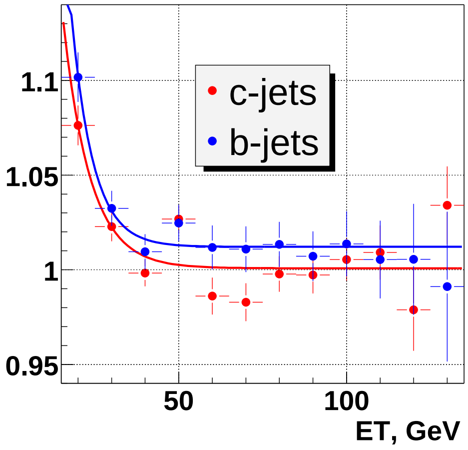

Figure 5.6: The ratio of the *b*- and *c*- to light jet taggability as a function of jet E_T.

5.4 *b*- and *c*-tagging efficiency in Monte Carlo

The *b*- (*c*-) tagging efficiency in Monte Carlo is (trivially) defined as probability to tag a *b*- (*c*-) jet. Here a formal definition of a *b*/*c* jet is needed. The jet flavor is determined by matching the direction of the reconstructed jet to the heavy flavor hadrons within the cone $\Delta R < 0.5$. A jet is considered to be a *b*-jet if the cone contains at least one *b*-hadron; otherwise, it is considered to be a *c*-jet if the cone contains at least one *c*-hadron. The rest are called light jets.

The *b*-tagging efficiency obtained on $t\bar{t}$ and $Z \rightarrow b\bar{b}$ samples [53] is shown in Fig. 5.7 as a function of jet E_T and η. Significant difference in one-dimensional *b*-tagging efficiencies between the samples is explained by different E_T and η spectra of *b*-jets as demonstrated in Fig. 5.7 (upper plot). *b*-jets in $t\bar{t}$ events are more energetic and more central compared to *b*-jets in $Z \rightarrow b\bar{b}$ events resulting in higher efficiency both versus jet E_T and η.

5.5 *b*-tagging efficiency in data

As opposed to the Monte Carlo case, the *b*-tagging efficiency in data can only be determined on a data sample enriched in *b*-content. The sample used for these purposes is the muon-in-jet data, where a large fraction of events is expected to originate from QCD heavy flavor production with subsequent semileptonic decays of *b*-quarks. The *b*-content of the sample can be further increased by requiring a muon to have a large ($>$1 GeV) transverse momentum with respect to jet axis (p_T^{rel}). The preselection of jets with high p_T^{rel} is by itself a *b*-tagging procedure and will be referred to as soft lepton tagging (SLT).

Three methods to determine the *b*-tagging efficiency in data have been considered. The first method, p_T^{rel} fit [56], relies on known (from Monte Carlo) distributions of the muon transverse momentum p_T^{rel} with respect to the jet axis for muons from light, *c*-, and *b*-jets (*templates*). The fit to the distribution of p_T^{rel} in data with a sum of three templates with weights to be determined (shown in Fig. 5.8) gives relative fractions of events with *b*-, *c*-, and light jets. The idea is to fit p_T^{rel} distribution in data before and after the tagging, thus obtaining the absolute number of *b*-jets in a sample. The ratio of the number of *b*-jets after and before tagging gives the *b*-tagging efficiency. The fits can be performed in jet E_T and η bins, which will result in *b*-tagging efficiency as a function of jet E_T (η).

By looking at p_T^{rel} templates one can see that *c*- and light templates look very similar. As a consequence, fit is not stable with respect to the relative fraction of *c*- to light jets. In other words, SLT puts together *c*- and light jets and separates them from *b*-jets (unlike CSIP which groups *c*-jets with *b*-jets). In order to avoid this instability, the ratio of the fraction of *c*-jets to the fraction of light-jets in the data is fixed to a value known from Monte Carlo (f_c/f_l =0.56). The same fraction after *b*-tagging is calculated assuming fixed ratio of c-tagging to mis-tagging efficiency (10). The uncertainty in these numbers together with uncertainty in the shape of p_T^{rel} templates contributes to the systematic error of Method 1, also called ST *vs* NT (Single Tag *vs* No Tag).

Method 2 is a variation of Method 1 which attempts to reduce its uncertainties by increasing the b content in the sample. To do that, each event is required to have exactly two jets, one of them being muonic, and the jet opposite to the muonic one being tagged by CSIP. The rest of the procedure (applied to the muonic jet) is exactly the same as in Method 1. Again, the b-tagging efficiency is obtained as the ratio of the number of b-jets after and before tagging. The fraction of b-jets in a double-tagged sample is close to 100%, and dependence of the b-tagging efficiency on f_c/f_l is mostly gone. Essentially, the fractions of b-jets obtained from the p_T^{rel} fit work as a correction to the ratio of double-tagged to single-tagged events. The statistics is lower compared to Method 1 but still enough to obtain the b-tagging efficiency as a function of jet E_T (η). This method will be referred to as DT *vs* ST (Double Tag *vs* Single Tag).

Method 3, called System 8 [57], is different from the first two in a sense that it relies solely on data. Two data samples with different b-fractions (“signal” and “background”) are considered, to which one applies two different b-tagging procedures (CSIP and SLT). For each sample four numbers are obtained: the number of jets before tagging; the number of jets tagged by CSIP; the number of jets tagged by SLT; and the number of jets tagged by both algorithms. If the signal sample has n jets of which n_b are b-jets and n_l are non-b- (c- and light) jets, and the background sample has p jets (p_b b-jets and p_l non-b-jets), then

$$\begin{aligned}
&n = n_b + n_l \\
&p = p_b + p_l \\
&n^{CSIP} = n_b \varepsilon^{CSIP}_{btag} + n_l \varepsilon^{CSIP}_{non-btag} \\
&p^{CSIP} = p_b \varepsilon^{CSIP}_{btag} + p_l \varepsilon^{CSIP}_{non-btag} \\
&n^{SLT} = n_b \varepsilon^{SLT}_{btag} + n_l \varepsilon^{SLT}_{non-btag} \\
&p^{SLT} = p_b \varepsilon^{SLT}_{btag} + p_l \varepsilon^{SLT}_{non-btag} \\
&n^{both} = n_b \varepsilon^{CSIP}_{btag} \varepsilon^{SLT}_{btag} + n_l \varepsilon^{CSIP}_{non-btag} \varepsilon^{SLT}_{non-btag} \\
&p^{both} = p_b \varepsilon^{CSIP}_{btag} \varepsilon^{SLT}_{btag} + p_l \varepsilon^{CSIP}_{non-btag} \varepsilon^{SLT}_{non-btag}.
\end{aligned} \tag{5.4}$$

This system of eight equations (hence the name of the method) has to be resolved against eight variables: n_b, n_l, p_b, p_l, and four tagging efficiencies. It can be solved analytically (it reduces to a cubic equation) but in practice it is more convenient to solve it using a likelihood fit (which provides errors on efficiencies in addition to efficiencies themselves).

The background sample is taken to be all muonic jets, and the signal sample (enriched in b-content) consists of muonic jets on events where second jet is tagged with CSIP (as in Method 2).

The *b*-tagging efficiency as a function of jet E_T and η obtained for all three methods is presented in Fig. 5.9. Good agreement is observed among the methods. Fig 5.10 shows the *b*-tagging efficiency measured on the muon-in-jet data as a function of jet E_T and η for various CSIP working points.

Each of described methods has its own sources of systematic errors that have to be studied in order to be propagated into the final result. The systematics for System 8 has been studied in most detail, and therefore it is chosen as a base method for the *b*-tagging efficiency measurement, the others being used as a cross-check.

The main sources of the systematics for System 8 are the following assumptions:

1. The two *b*-taggers (CSIP and SLT) are completely uncorrelated. That means that efficiency shown by a combined tagger is equal to a product of efficiencies of individual taggers:

$$\kappa_b = \frac{\varepsilon_{btag}^{CSIP\times SLT}}{\varepsilon_{btag}^{CSIP}\varepsilon_{btag}^{SLT}} \sim 1. \tag{5.5}$$

2. The probability to tag a *b*-jet in a di-jet event does not depend on whether or not the opposite jet is tagged:

$$\beta = \frac{\varepsilon_{btag}^{CSIP}(away = tagged)}{\varepsilon_{btag}^{CSIP}} \sim 1. \tag{5.6}$$

These assumptions can be checked on Monte Carlo. Both factors appear to be very close to 1 (Fig. 5.11) with uncertainly of 2%. This uncertainty is propagated to the efficiency reported by System 8 by modifying its equations to take into account κ_b and β factors. The systematic errors due to these uncertainties are shown on Fig 5.12.

5.6 Scale factor

Differences in the track finding efficiency in data and simulation as well as in the impact parameter resolutions lead to the differences in the *b*-tagging efficiency in data and Monte Carlo. A correction factor *SF* is necessary to relate the b-tagging efficiency in data and Monte Carlo:

$$\varepsilon_{data} = \varepsilon_{MC} \times SF. \tag{5.7}$$

Here both ε_{data} and ε_{MC} were measured on semileptonic *b*-jets. The Monte Carlo semileptonic *b*-tagging efficiency was measured on $Z \to b\bar{b}$ and $t\bar{t}$ samples, where we required b-jets to have a muon inside ($\Delta R(b,\mu) < 0.5$). For the data we have used the b-tagging efficiency obtained with System 8. Fig. 5.13 shows the ratios of semileptonic *b*-tagging efficiency on data and $t\bar{t}$ (left) and $Z \to b\bar{b}$ (right) as functions of jet E_T and η. Scale factors are fairly flat in jet E_T, η. Fits by a constant versus jet E_T and η look consistent for all working points and for both Monte Carlo samples. The values of the scale factor obtained from jet E_T and η fits are brought together in

Table 5.1.

	$p_T > 0.5$	$p_T > 1$	$p_T > 1.5$	$p_T > 2$
fit E_T	0.785 ± 0.009	0.764 ± 0.009	0.745 ± 0.011	0.745 ± 0.012
fit η	0.785 ± 0.009	0.759 ± 0.009	0.741 ± 0.011	0.743 ± 0.012

Table 5.1: The scale factors obtained from a fit by a constant ($t\bar{t}$).

5.7 Mis-tagging rate

The mis-tagging rate (probability to tag a light jet) in data has been determined by two different methods.

Method 1 is based on a measurement of *negative tag rate* ε^- determined as a probability to tag a generic QCD jet using slightly modified tagging procedure: instead of requiring at least two tracks with $S > 3$ or three tracks with $S > 2$, one now requires at least two tracks with $S < -3$ or three tracks with $S < -2$. The preselection criteria for "good" tracks remain the same. Since the S distribution for light jets is fairly symmetric (see Fig 5.1, right), ε^- is a good approximation for ε_{light}. It has however to be corrected for two non-negligible effects:

- the positive light jet tag rate (*e.g.* regular mis-tagging rate ε_{light}) is higher than the negative one (ε^-_{light});
- the negative b-tagging efficiency is higher than the negative light jet tag rate. It can also be observed on Fig 5.1, where the S distribution for b jets goes higher

both for $S < 0$ and $S > 0$ (although effect at $S < 0$ is much less pronounced).

The first effect was discussed in detail in Section 5.2, and the scale factor SF_{ll} was introduced. The second effect is mostly due to mistakes in the sign of the DCA projection onto the jet axis. It is taken into account by introducing another scale factor SF_{hf}, the ratio of negatively tagged light jets to negatively tagged inclusive jets. These scale factors are found to be independent from the jet parameters and equal to $SF_{ll} = 1.575 \pm 0.034$, $SF_{hf} = 0.612 \pm 0.013$. The total correction factor $SF_{ll} \times SF_{hf} = 0.964 \pm 0.018$, is very close to 1, so the two effects essentially compensate each other. Finally, mis-tagging rate is obtained as $\varepsilon_{light} = SF_{ll} \times SF_{hf} \times \varepsilon^{-}$

The mis-tagging rate as a function of jet E_T and η obtained with Method 1 is shown in Fig. 5.14, upper.

Method 2 begins with positive tag rate ε^{+} measured on QCD data. Since not all of jets are light, ε^{+} is an overestimation for ε_{light}. If fractions of b- and c- jets in QCD are f_b and f_c, respectively, the positive tag rate can be written down as follows:

$$\varepsilon^{+} = \varepsilon_{light}(1 - f_b - f_c) + \varepsilon_{ctag} f_c + \varepsilon_{btag} f_b, \tag{5.8}$$

where

- ε_{btag} is b-tagging efficiency measured on data,

- ε_{ctag} is c-tagging efficiency measured on Monte Carlo and corrected to the data as $\varepsilon_{ctag}^{data} = \varepsilon_{ctag}^{MC} \times SF$

Inverting the equation, one gets

$$\varepsilon_{light} = \frac{\varepsilon^{+} - \varepsilon_{ctag} f_c - \varepsilon_{btag} f_b}{1 - f_b - f_c}. \tag{5.9}$$

The weak point of this method is use of f_b and f_c from Monte Carlo which are not reliable. The result obtained with Method 2 is compared to Method 1 in Fig. 5.14, lower. The two methods agree within 20% except for the low E_T region where Method 2 fails because it is based on subtraction of two large numbers, and when result is expected to be small, the relative error can become arbitrarily large. Therefore Method 1 is chosen as the base one, and Method 2 used as a cross-check.

The systematic errors associated with the mis-tagging rate are derived from the following sources:

1. The negative tag rate closure test (comparison of number of predicted and observed negatively tagged jets). The results of this test are shown in Fig. 5.15. There is a discrepancy at high jet E_T which is taken as systematic uncertainty.
2. The difference in negative tag rate between two samples used for its estimation (EMqcd and jettrig). It originates from the different average number of track per taggable jet in these samples. The overall effect is about 20% in average.

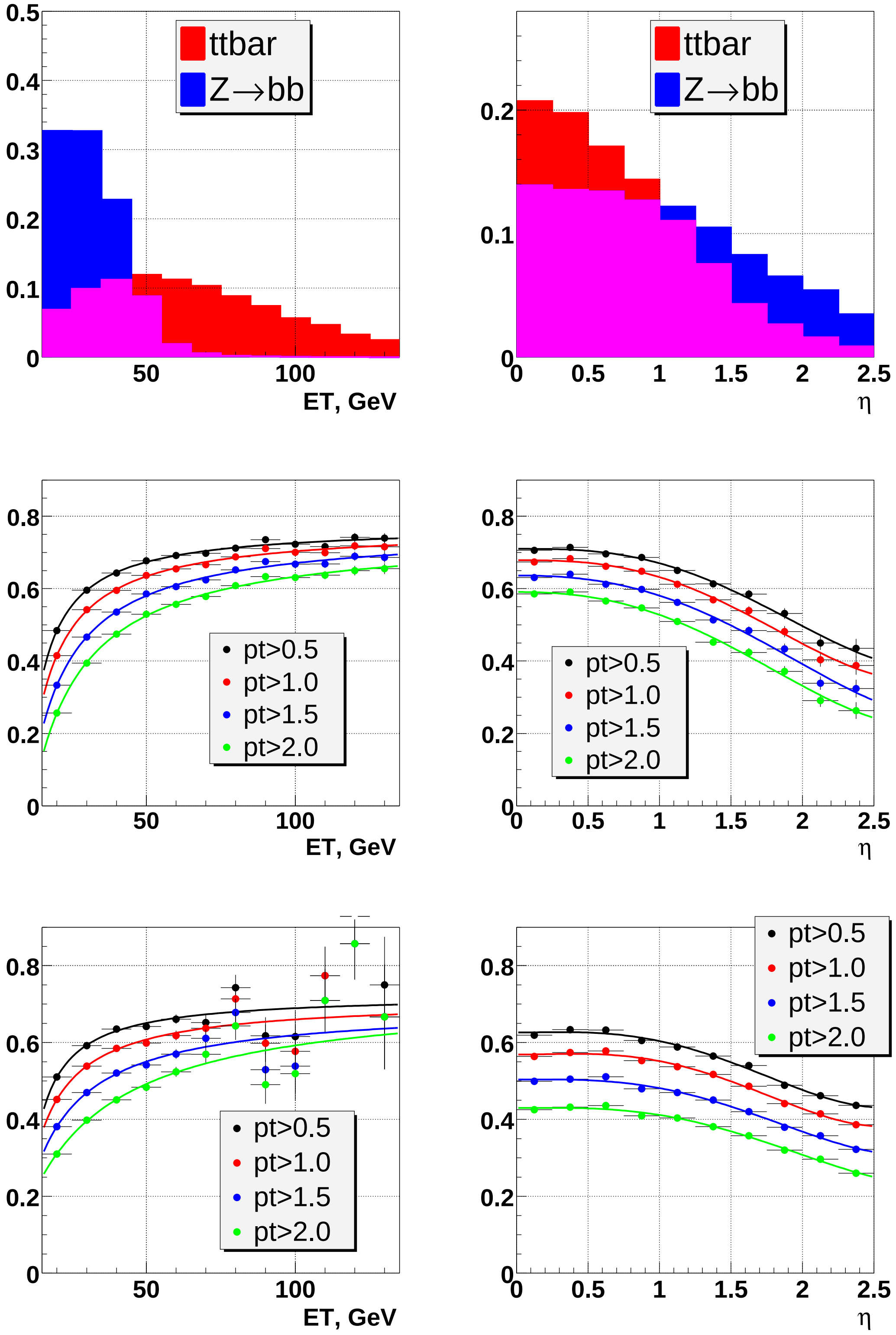

Figure 5.7: E_T and η distributions of *b*-jets in $t\bar{t}$ and $Z \to b\bar{b}$ events (upper), and *b*-tagging efficiency in $t\bar{t}$ (middle) and $Z \to b\bar{b}$ (lower) events.

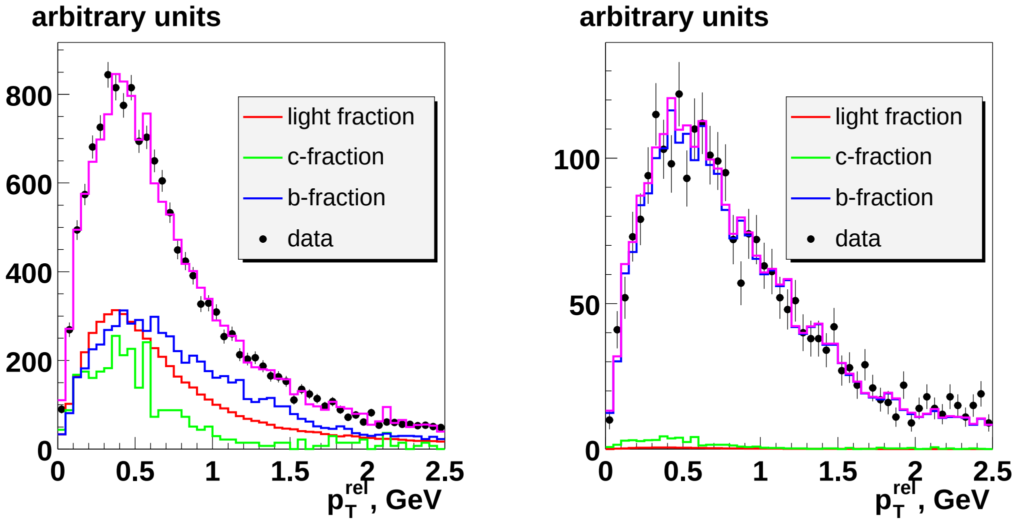

Figure 5.8: The fit to the distribution of p_T^{rel} in data with a sum of three templates (for light, c-, and b-jets) before (left) and after (right) the tagging.

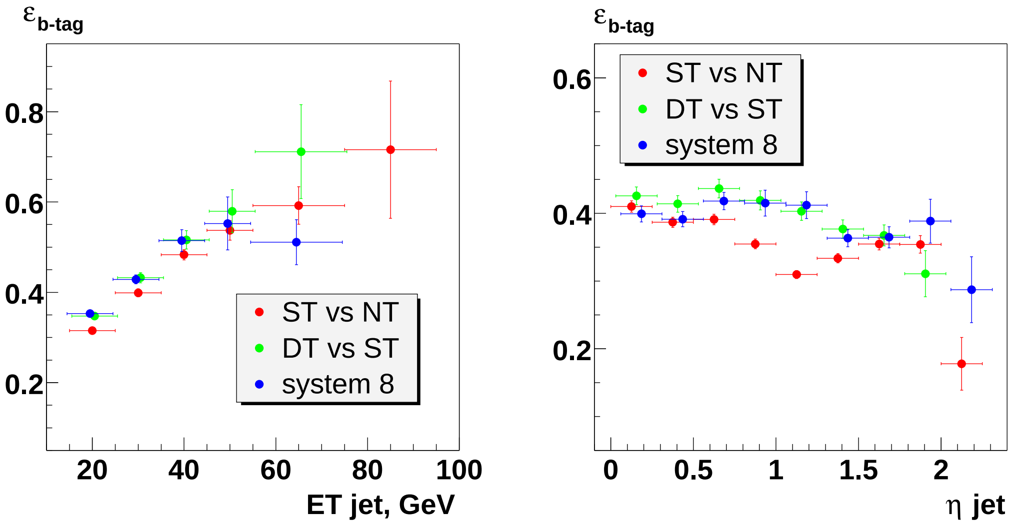

Figure 5.9: Semileptonic b-tagging efficiency as a function of jet E_T and η measured on data by three methods.

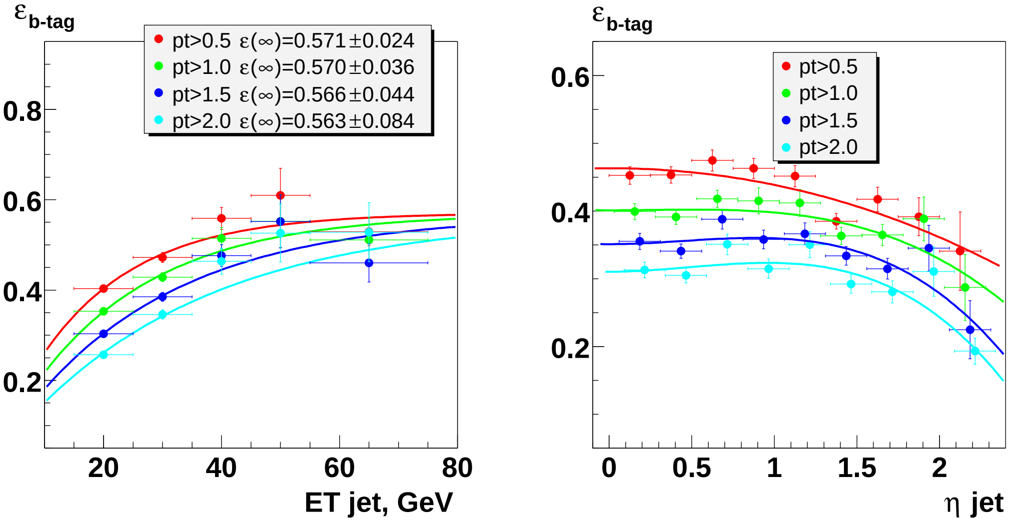

Figure 5.10: Semileptonic b-tagging efficiency as a function of jet E_T and η measured on μ-in-jets data for the four working points.

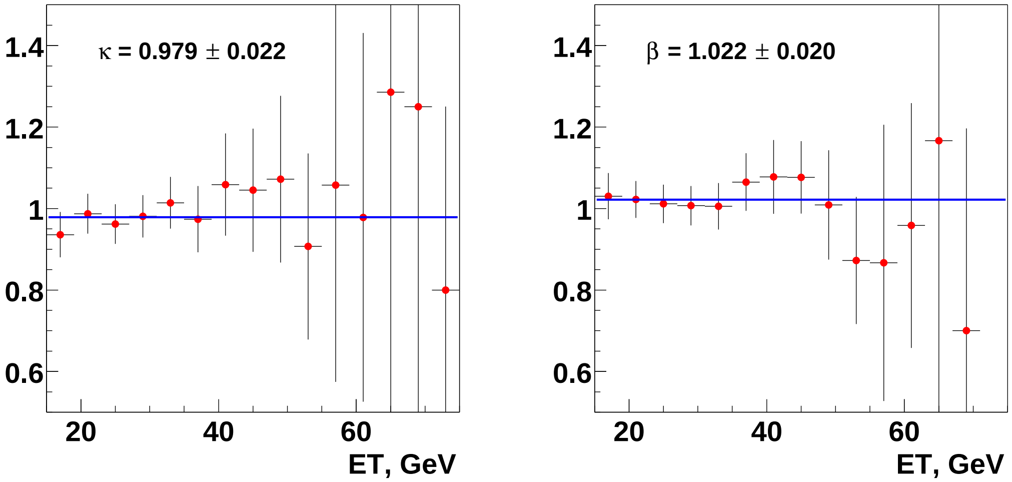

Figure 5.11: k_b (left) and β (right) as functions of jet E_T.

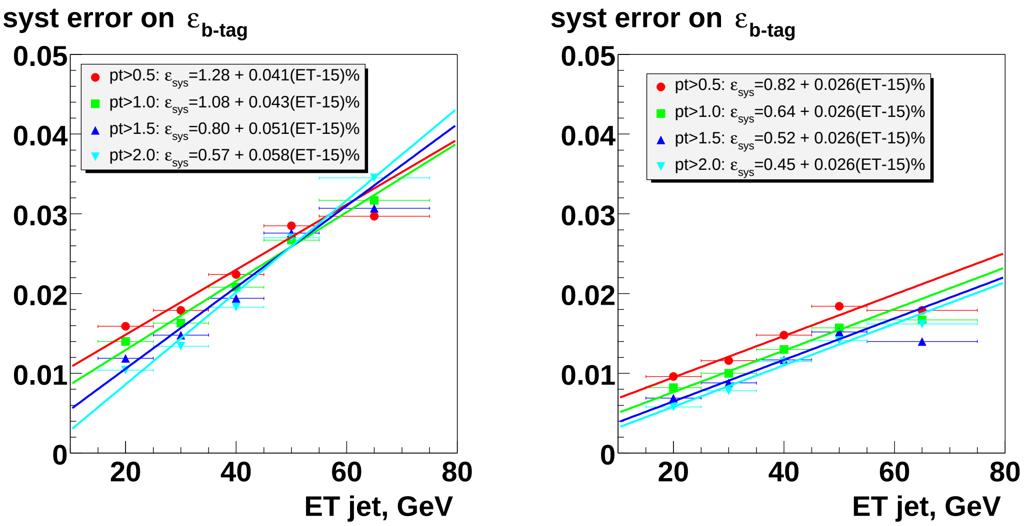

Figure 5.12: Systematic errors on b-tagging efficiency due to k_b (left) and β (right).

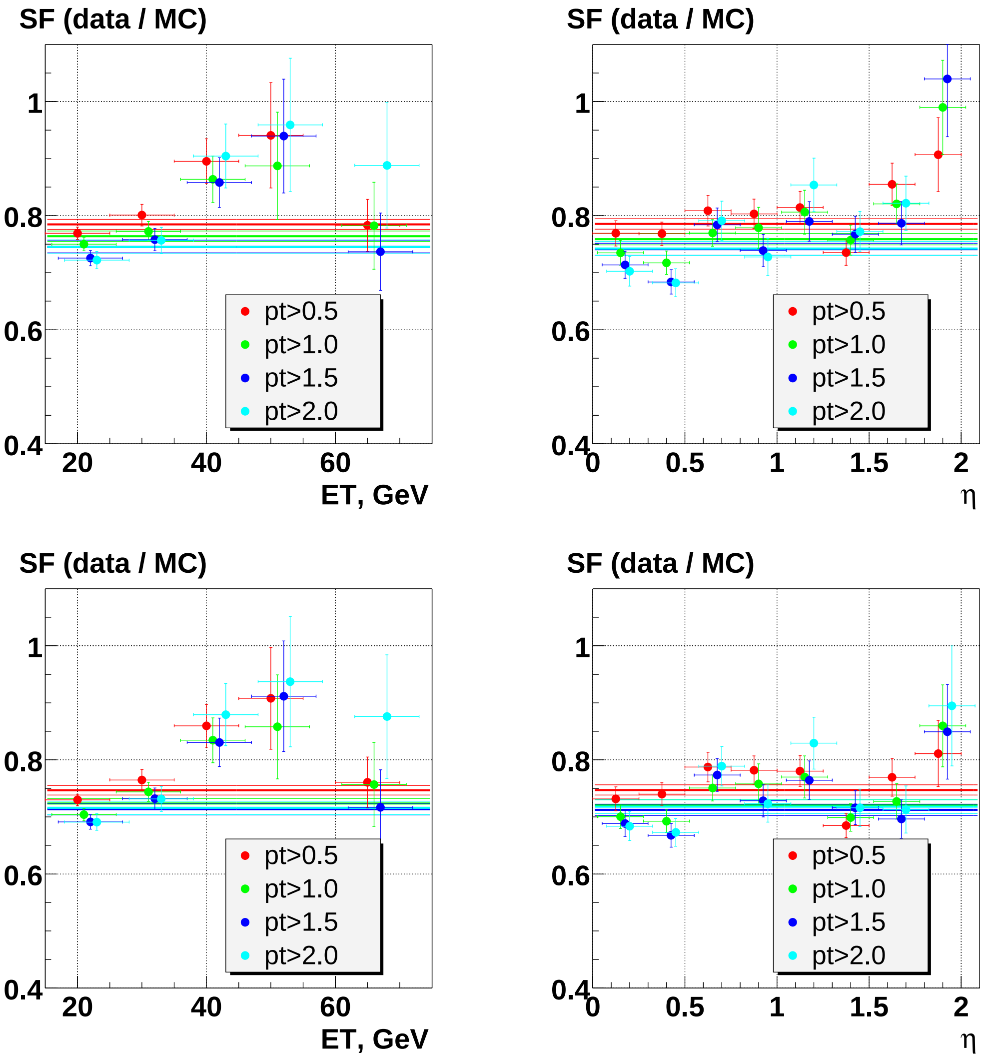

Figure 5.13: The scale factor as a function of jet E_T and η calculated using semileptonic b-tagging efficiency obtained on $t\bar{t}$ (upper) and $Z \to b\bar{b}$ (lower) Monte Carlo samples.

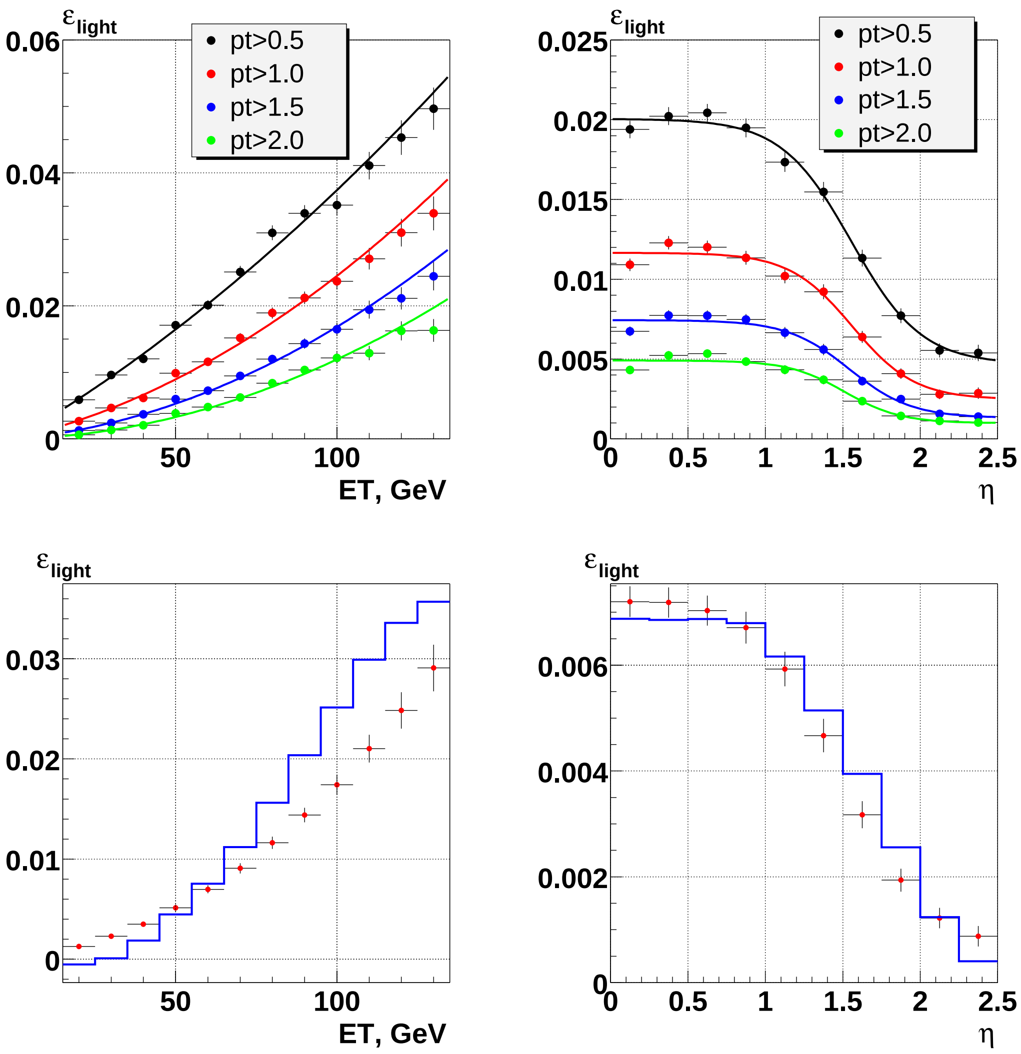

Figure 5.14: The mis-tagging rate vs jet E_T and η (upper) and comparison of results obtained with different methods (lower). On the lower plots, the red points and blue lines correspond to Methods 1 and 2, respectively.

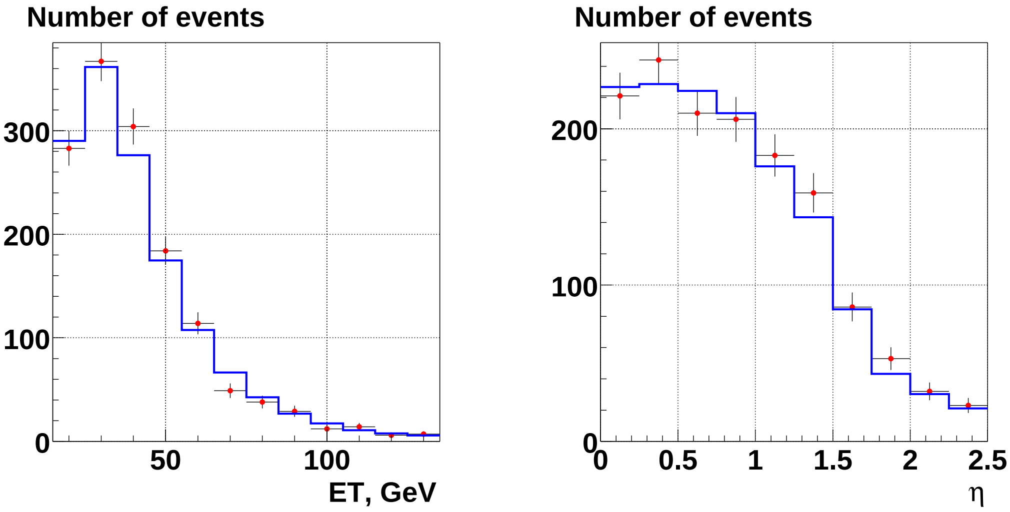

Figure 5.15: The number of negatively tagged events in EMqcd predicted by NTRF (blue lines) and actual negative tags (red points) vs jet E_T (left) and η (right).

Chapter 6

Analysis strategy

In this chapter, the principal steps in the measurement of $\sigma_{t\bar{t}}$ in the $t\bar{t} \to l$+jets channel are outlined, different approaches are discussed and a particular choice is motivated.

6.1 Event preselection

The events preselected for the study of the $t\bar{t} \to l$+jets channel are required to have a high p_T isolated lepton (muon or electron) and high missing transverse energy $\not\!\!E_T$ presumably arising from the undetected neutrino. These requirements aim to preselect a sample of W+jets candidate events, where W decays to a lepton and a neutrino. Fig. 6.1 shows Monte Carlo distributions of the momentum of the highest p_T lepton and $\not\!\!E_T$ in $t\bar{t}$ events and in non-W background.

The total number of preselected events is denoted by N. This is the starting point

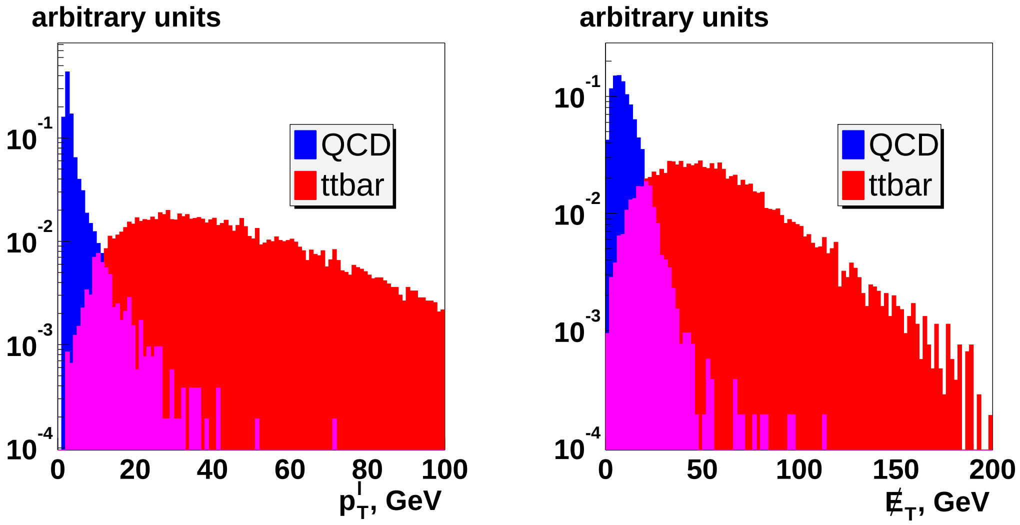

Figure 6.1: The momentum of the highest p_T lepton (left) and $\not{E}_T$(right) in $t\bar{t}$ events and in QCD.

of the more specific analysis. The sample includes three components: the $t\bar{t}$ (signal), W+jets, and the non-W fraction, with the corresponding number of events denoted by $N^{t\bar{t}}$, N^W, and N^{bkg}, respectively, so that $N = N^{t\bar{t}} + N^W + N^{bkg}$.

6.2 Distribution of events as a function of jet multiplicity

The next step is to look at the number of events with a particular jet topology. This is motivated by the fact that the W+jets events have a jet multiplicity that decreases rapidly with the number of jets n_j, while the jet multiplicity for signal has a peak at n_j =4 (two b-jets and two jets from the W that decays into $q\bar{q}\prime$). The signal is expected in events with at least three jets. With better statistics, it would be reasonable to consider only events with $n_j \geq 4$ because it provides a better signal to background ratio. However, with the small number of expected $t\bar{t}$ events, the $n_j = 3$ bin has been retained because it contains almost as much a signal as the $n_j \geq 4$ bin, and a tolerable background.

As a result of the different signal to background ratio, events in bins $n_j = 3$ and $n_j \geq 4$ are not added. Instead, their contribution is taken independently, as two factors in the overall likelihood expression. All three event components contribute to each jet multiplicity bins, so $N_i = N_i^{t\bar{t}} + N_i^W + N_i^{bkg}$.

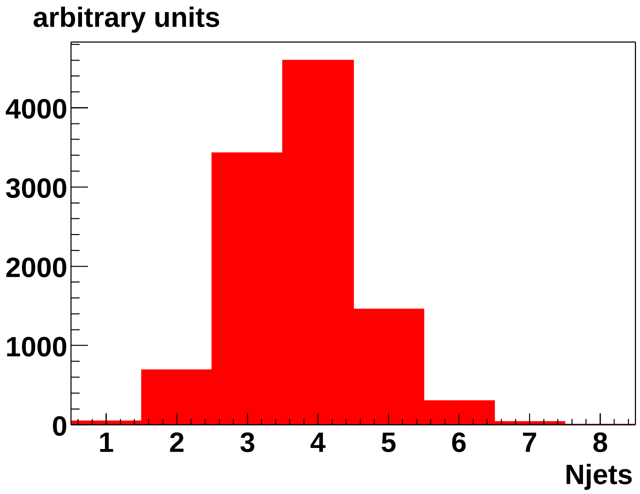

Figure 6.2: The number of jets in $t\bar{t}$ events.

	σ (pb)		σ (pb)		σ (pb)		σ (pb)
Wj	424.90	Wjj	126.81	$Wjjj$	32.48	$Wjjjj$	8.89
Wc	16.01	$Wc\underline{j}$	7.60	$Wc\underline{jj}$	2.38	$Wc\underline{jj}j$	0.64
		Wbb	4.61	$WbbJ$	2.00	$WbbJj$	0.81
		$Wc\bar{c}$	11.43	$Wc\bar{c}J$	4.68	$Wc\bar{c}Jj$	1.93

Table 6.1: W+jets processes and their cross sections. j stands for light jets, and J stands for non-b (light or c) jets.

6.3 *b*-tagging

The signal to background ratio improves dramatically after application of b-tagging. This is because most of the $t\bar{t}$ events have two b-jets, and therefore the probability to tag a $t\bar{t}$ event with at least one b-jet is rather high (50-60%). On the contrary, the W+jets background is dominated by events with light jets. The cross section for W production is association with jets of different flavor is shown in Table 6.1. It follows from the table, that about 90-95% of the jets in W+jets are light, and the same is true for the non-W component.

As there are two b-jets in a $t\bar{t}$ event, it makes sense to consider single-tagged and double-tagged events separately. The sample of double-tagged events is very pure, but it is small. The separation between single-tagged and double-tagged events provides a cross-check of how well the background is modeled.

The total number of events remaining in jet multiplicity bins after the b-tagging is applied is denoted by N_i^{tag}, and again, it can be split into three parts: $N_i^{tag} = N_i^{t\bar{t}\ tag} + N_i^{W\ tag} + N_i^{bkg\ tag}$.

6.4 The non-W background

The procedure used to calculate the number of non-W events, called the matrix method, is described in [58]. It relies on two samples: a “loose” and “tight” one, with different content of the W and non-W components. The tight sample is taken to be the signal one (the number of events $N_i^{tight} = N_i$), and the loose sample is obtained by relaxing the quality requirement on the high p_T lepton (the number of events N_i^{loose}). The method depends on two sets of numbers: ε_i^{sig} (probability to go from loose to tight for a W event) and ε_i^{bkg} (the same probability for a non-W event). Denoting the number of W events in the loose and tight sample as $N_i^{sig\ loose}$ and $N_i^{sig\ tight}$, and the number of non-W events in the loose and tight sample as $N_i^{bkg\ loose}$ and $N_i^{bkg\ tight}$, respectively, these numbers can be obtained by solving the following system of equations:

$$\begin{aligned}
N_i^{loose} &= N_i^{sig\ loose} + N_i^{bkg\ loose} \\
N_i^{tight} &= N_i^{sig\ tight} + N_i^{bkg\ tight} \\
N_i^{sig\ tight} &= \varepsilon_i^{sig} N_i^{sig\ loose} \\
N_i^{bkg\ tight} &= \varepsilon_i^{bkg} N_i^{bkg\ loose} .
\end{aligned} \tag{6.1}$$

At this step there is no distinction between $t\bar{t}$ and W+jets, so that $N_i^{sig} = N_i^{t\bar{t}} + N_i^{W}$. It is assumed that ε_i^{sig} is identical for $t\bar{t}$ and W+jets. It should be recognized that the matrix method reflects the overall fraction of W and non-W events, but it cannot separate them on event-by-event basis.

The application of the matrix method to the untagged sample is straightforward. The question is how to obtain the predicted number of non-W tagged events $\bar{N}_i^{bkg\ tag}$. Considering the order in which b-tagging and the matrix method are applied, there are two possibilities. The first approach is to calculate N_i^{bkg}, the number of non-W events before b-tagging, and given probability to tag a non-W event, $\bar{P}_i^{bkg\ tag}$, calculate $\bar{N}_i^{bkg\ tag}$ as

$$\bar{N}_i^{bkg\ tag} = N_i^{bkg}\bar{P}_i^{bkg\ tag}. \tag{6.2}$$

The probability to tag a non-W event is calculated on a control sample kinematically similar to the signal one, but with a depleted W component. The obvious choice is a signal sample with reversed tight requirement (events preselected so that EM objects *do not* pass tight requirement). Another possibility is a sample with upper $\not{E}_T$ cut that vetoes W's.

The second approach is to obtain $\bar{N}_i^{bkg\ tag}$ by applying the matrix method to the tagged event sample:

$$\begin{aligned}
N_i^{loose\ tag} &= N_i^{sig\ loose\ tag} + N_i^{bkg\ loose\ tag} \\
N_i^{tight\ tag} &= N_i^{sig\ tight\ tag} + N_i^{bkg\ tight\ tag} \\
N_i^{sig\ tight\ tag} &= \varepsilon_i^{sig\ tag} N_i^{sig\ loose\ tag} \\
N_i^{bkg\ tight\ tag} &= \varepsilon_i^{bkg\ tag} N_i^{bkg\ loose\ tag},
\end{aligned} \tag{6.3}$$

so that $\bar{N}_i^{bkg\ tag} = N_i^{bkg\ tight\ tag}$.

The former method is more precise because it is applied on untagged sample with high statistics. In the case of e+jets, it will be shown that both methods yield consistent results, so the first method is used as having superior precision. In the case of μ+jets however, the situation is more complicated. The non-W background in this case is enriched by contribution from heavy flavor, which is different from control samples described above. Therefore, for μ+jets the second method is used.

6.5 The W+jets background and $t\bar{t}$ signal

After the non-W background is estimated, the next step is to estimate the W and $t\bar{t}$ contributions. This can be done using, again, the matrix method, but this time by comparing untagged and tagged events:

$$\begin{aligned} N_i^{sig} &= N_i^W + N_i^{t\bar{t}} \\ N_i^{sig\ tag} &= N_i^{W\ tag} + N_i^{t\bar{t}\ tag} \\ N_i^{W\ tag} &= \bar{P}_i^{W\ tag} N_i^W \\ N_i^{t\bar{t}\ tag} &= \bar{P}_i^{t\bar{t}\ tag} N_i^{t\bar{t}}, \end{aligned} \tag{6.4}$$

where N_i^{sig} and $N_i^{sig\ tag}$ are obtained at the previous step. There are, in fact, two such systems of equations, referring to single-tagged ($t = 1$) and double-tagged ($t \geq 2$)

events. $\bar{P}_i^{W\ tag}$ is an average probability to tag a W+jets event defined as

$$\bar{P}_i^{W\ tag} = \sum_j F_i^j \bar{P}_i^{j\ tag}, \tag{6.5}$$

where F_i^j are the fractions of the relevant W+jets subprocesses, and $\bar{P}_i^{j\ tag}$ are their respective average event tagging probabilities. This step yields the expected number of tagged W events $N_i^{W\ tag}$.

6.6 The $t\bar{t}$ production cross section

Having all the numbers in hand, the $t\bar{t}$ production cross section is calculated using a maximum likelihood fit

$$\begin{aligned} L &= \prod_{l=e,\mu} \prod_{i=3,\geq 4} \prod_{t=1,\geq 2} L_i, \\ L_i &= \frac{e^{-\bar{N}_i^{tag}} (\bar{N}_i^{tag})^{N_i^{tag}}}{N_i^{tag}!}, \\ \bar{N}_i^{tag} &= \bar{N}_i^{t\bar{t}\ tag} + \bar{N}_i^{W\ tag} + \bar{N}_i^{bkg\ tag}. \end{aligned} \tag{6.6}$$

In the first formula, the first product is taken over $t\bar{t}$ observation modes (e+jets and μ+jets), the second product is taken over the two jet multiplicity bins, and the third product is taken over single-tagged and double-tagged events. The expected number of $t\bar{t}$ events $\bar{N}_i^{t\bar{t}\ tag}$ is related to the $t\bar{t}$ production cross section $\sigma_{t\bar{t}}$ by

$$\bar{N}_i^{t\bar{t}\ tag} = \sigma_{t\bar{t}}\, \mathcal{L}\, \varepsilon_i^{t\bar{t}}\, BR(t\bar{t} \rightarrow l\text{+jets}), \tag{6.7}$$

where $\mathcal{L}$ is integrated luminosity, $\varepsilon_i^{t\bar{t}}$ is the total signal selection efficiency and $BR(t\bar{t} \rightarrow l\text{+jets})$ is the appropriate branching ratio. The total signal selection efficiency is a product of probability to tag a $t\bar{t}$ event and preselection efficiency for untagged $t\bar{t}$ events $\varepsilon_i^{t\bar{t}\ sel}$ (that includes trigger efficiency and probability of a $t\bar{t}$ event to pass preselection cuts), so that $\varepsilon_i^{t\bar{t}} = \varepsilon_i^{t\bar{t}\ sel} \bar{P}_i^{t\bar{t}\ tag}$.

By maximizing L with respect to $\sigma_{t\bar{t}}$ one obtains the most likely value for $\sigma_{t\bar{t}}$ (together with its uncertainty), and this completes the calculation of the $t\bar{t}$ production cross section.

6.7 Summary of analysis components

Extracting the $t\bar{t}$ production cross section requires the following inputs:

- number of preselected lepton+jets events in jet multiplicity bins N_i,
- number of preselected tagged events N_i^{tag},
- number of preselected events with relaxed selection N_i^{loose},
- number of preselected tagged events with relaxed selection $N_i^{loose\ tag}$ (only for the μ+jets channel).

In order to calculate the $t\bar{t}$ cross section, the following are needed:

- for the matrix method: probability for a high p_T lepton that passed “loose” selections to pass additional “tight” criteria. These have to be determined separately for leptons from signal (ε_i^{sig}) and from non-W background (ε_i^{bkg});
- for the non-W background in the tagged sample: average probability to tag a non-W event $\bar{P}_i^{bkg\ tag}$;
- for the W background in the tagged sample: fraction of W+jets events with particular jet flavor configuration F_i^j and their respective average event tagging probabilities $\bar{P}_i^{j\ tag}$;
- for the predicted number of $t\bar{t}$ events in the tagged sample: average probability to tag a $t\bar{t}$ event $\bar{P}_i^{t\bar{t}\ tag}$, signal selection efficiency $\varepsilon_i^{t\bar{t}\ sel}$ (before b-tagging), and integrated luminosity $\mathcal{L}$.

The details of the calculation of the cross section are described in the next chapter.

Chapter 7

The cross section measurement

7.1 Monte Carlo samples

The $t\bar{t}$ signal and main background process (W+jets) have been generated using ALPGEN 1.2 [59] Monte Carlo generator with parton distribution functions (parameterizations describing parton properties inside the nucleon) CTEQ 6.1M [60]. This generator is dedicated to the study of multiparton processes, giving rise to several high E_T and well separated jets. It was used to calculate the leading-order matrix element for the different parton configurations (up to four in the final state). The ALPGEN generator has been interfaced to PYTHIA 6.2 [61] (CTEQ5L [62]) to simulate the underlying event, additional initial state radiation, and hadronization. The top quark mass was set to be of 175 GeV. Monte Carlo samples contain all lepton+jets final states, including taus with leptonic decays.

The WW, WZ, ZZ backgrounds are evaluated using samples generated with ALPGEN followed by PYTHIA. The single top samples were generated with COMPHEP [63] followed by PYTHIA, and $Z/\gamma^* \to \tau\tau$ samples were produced by PYTHIA. A detailed description of Monte Carlo samples can be found in [64].

All events have additional number of minimum bias $p\bar{p}$ events [65] superimposed. The number of added events is taken from a Poisson distribution with a mean of 0.8. The Monte Carlo samples are processed through the GEANT simulation of the DØ detector, *d0gstar*, the simulation of the detector response, *d0sim*, and full event reconstruction, *d0reco* [66].

7.2 Data set

The details of event preselection and discussion of the correction factors between the data and Monte Carlo can be found in [67]. Below, the principal steps of the event preselection chain are outlined.

7.2.1 Luminosity

The data used in this analysis were collected between June 2002 and September 2003. The total integrated luminosity of the data set is 168.7 pb^{-1} for e+jets and 158.4 pb^{-1}

for μ+jets. The total uncertainty on the integrated luminosity is estimated to be 6.5%. The details of luminosity calculation are explained in [68] and references therein.

7.2.2 Trigger

At the trigger level, the μ+jets channel relies on a trigger which requires one muon and one calorimeter tower with $E_T > 5$ GeV at Level 1, one medium quality muon at Level 2, and one jet with $E_T > 20$ GeV at Level 3. The e+jets channel trigger requires one calorimeter tower with EM $E_T > 10$ GeV and two calorimeter towers with total $E_T > 5$ GeV at Level 1, one EM object with an electromagnetic fraction of at least 0.85 and $E_T > 10$ GeV and two jets with $E_T > 10$ GeV, and one EM particle with $E_T > 15$ GeV and with a requirement on the shower-shape and two jets with $E_T > 15$ GeV at Level 3. At each level, the EM object is treated as a jet as well.

7.2.3 Primary vertex identification

The primary vertex is required to lie within the SMT fiducial volume ($|z_{PV}| < 60$ cm) and to have at least three tracks attached to it. This choice is motivated by the primary vertex quality needed for b-tagging.

7.2.4 Electron identification

Only EM objects in the central EM calorimeter ($|\eta^{det}| < 1.1$) are considered. The EM objects in the central calorimeter are defined as collections of towers around an initial ("seed") tower with high energy. An EM object is called a "loose" electron if it meets the following criteria:

- transverse momentum $p_T^{EM} > 20$ GeV;
- the ratio of the EM fraction of the energy to the total energy measured in the calorimeter $f_{emf} > 0.9$;
- EM isolation $f_{iso} = \frac{E_{total}(\Delta R<0.4) - E_{EM}(\Delta R<0.2)}{E_{EM}(\Delta R<0.2)} < 0.15$;
- the value of H-matrix (parameter derived from the energy profile in the calorimeter) HM8x$<$75;
- the EM object is matched to a central track originated within 1 cm from the primary vertex.

An electron is considered "tight" if on top of loose requirements it also has a likelihood $lh > 0.75$. This parameter is designed to identify isolated high p_T electrons. It includes χ^2 of the spacial match between the EM object and a central track, the ratio of transverse energy of the EM cluster to the track p_T, H-matrix, EM energy fraction, distance of closest approach of the track to the primary vertex, and ΔR distance to second closest track to the EM cluster.

7.2.5 Muon identification

The muons accepted for the analysis are required to meet the following criteria:

- transverse momentum $p_T^\mu >$20 GeV;
- the muon has segments in all three layers of the muon system (A, B, and C);
- medium quality, defined as a combination of particular number of hits in A and BC layers;
- the muon is far away from any jet ($\Delta R >$0.5);
- the muon satisfies a cosmic veto based on scintillator timing cuts;
- the muon is matched to a central track within 1 cm from the primary vertex which has DCA significance $<$3 and $\chi^2/NDF <$4.

Such a muon is called “loose”.

A muon is considered “tight” is on top of loose requirements it also satisfies more stringent isolation criteria:

- isolation from calorimeter energy: Halo(0.1,0.4)/$p_T^\mu <$0.08, where Halo(0.1,0.4) is the sum of the E_T of calorimeter clusters in a hollow cone 0.1$< \Delta R <$0.4

away from the muon;

- isolation from tracks: TrkConePt(0.5)/p_T^μ <0.06, where TrkConePt(0.5) is the sum of the p_T of all tracks within a cone ΔR <0.5 around the muon, excluding the muon track.

7.2.6 Jet identification

Jets are reconstructed using cone algorithm with ΔR <0.5. There are further requirements aimed to remove EM objects and suppress jets from instrumental background. They include:

- the ratio of the EM fraction of the energy to the total energy measured in the calorimeter $0.05 < f_{emf} < 0.95$;
- fraction of the energy measured in the coarse hadronic calorimeter $f_{CH} < 0.4$;
- hot cell ratio HotF<10, defined as the ratio of the highest to the next-to-highest E_T cell in the cluster;
- the number of calorimeter towers containing 90% of the jet energy n90>1

In addition, a jet is required to have sufficient energy deposited at Level 1 calorimeter trigger system.

The energy measured in the calorimeter is corrected for the underlying event, noise, response, and showering effects.

Jets considered in the analysis have corrected E_T >15 GeV and $|\eta|$ <2.5.

7.2.7 Additional selection cuts

In both channels a second lepton veto is applied. That means that except the selected high p_T lepton there must be no other loose lepton with p_T >15 GeV.

To suppress the non-W background, both channels apply a triangular cut selection. In the case of e+jets, the requirement is

$$\begin{aligned} &\not{E}_T > 20 \text{ GeV} \\ &\Delta\varphi(\not{E}_T, EM) > 1.7 - 1.7\not{E}_T/80 \text{ GeV}. \end{aligned} \tag{7.1}$$

In the case of μ+jets, the condition is more complicated and involves highest E_T jet as well as $\not{E}_T$:

$$\begin{aligned} &\not{E}_T > 17 \text{ GeV} \\ &1.2 - 1.2\not{E}_T/38 \text{ GeV} < \Delta\varphi(\not{E}_T, \mu) < 1.3 + (\pi - 1.3)\not{E}_T/24 \text{ GeV} \\ &\Delta\varphi(\not{E}_T, jet) < 2.2 + (\pi - 2.2)\not{E}_T/26 \text{ GeV}. \end{aligned} \tag{7.2}$$

In both channels, these cuts were optimized using a grid search technique [69] improving the QCD rejection to minimize systematics due to the QCD background.

	W+1jet	W+2jets	W+3jets	W+$\geq$4jets
N_i	6321	2348	586	174
N_i^{loose}	8765	3980	1262	394
N_i^{tag}	101	85	43	34
$N_i^{loose\ tag}$	141	157	77	50
$N_i^{double\ tag}$		6	4	5
$N_i^{loose\ double\ tag}$		7	6	8

Table 7.1: Number of events in the e+jets channel: preselected events, preselected events with relaxed selection, tagged events, tagged events with relaxed selection, double tagged events, double tagged events with relaxed selection.

	W+1jet	W+2jets	W+3jets	W+$\geq$4jets
N_i	5130	2077	511	119
N_i^{loose}	7763	3503	1013	247
N_i^{tag}	80	70	39	18
$N_i^{loose\ tag}$	146	123	68	34
$N_i^{double\ tag}$		5	3	3
$N_i^{loose\ double\ tag}$		5	3	4

Table 7.2: Number of events in the μ+jets channel: preselected events, preselected events with relaxed selection, tagged events, tagged events with relaxed selection, double tagged events, double tagged events with relaxed selection.

7.2.8 The input numbers of events

The input numbers of events preselected according to above criteria are given in Tables 7.1, 7.2. The $t\bar{t} \rightarrow l$+jets selection efficiency in jet multiplicity bins is given in Table 7.3.

	W+1jet	W+2jets	W+3jets	W+$\geq$4jets
e+jets	0.05±0.01	0.84±0.04	3.50±0.08	6.48±0.10
μ+jets	0.03±0.01	0.69±0.03	3.13±0.07	6.35±0.10

Table 7.3: Preselection efficiencies (%) in the e+jets and μ+jets channels (statistical errors only).

7.3 Probabilities for the matrix method

The probabilities ε_{sig} for a loose electron (muon) from W decay to pass tight definition are determined on a $Z \to e^+e^-$ ($Z \to \mu^+\mu^-$) sample. For e+jets ε_{sig} is measured for $Z \to e^+e^-$ events with at least one additional jet. The efficiency is found to be fairly constant over jet multiplicity bins. In the case of μ+jets, ε_{sig} is measured separately in each jet multiplicity bin. The values measured in data are corrected for the difference in the angular distribution of leptons from $t\bar{t}$ and from Z.

The same probability ε_{bkg} for loose muons from the non-W background is calculated on a sample that is preselected in the same way as the signal sample except that the missing energy cuts are replaced by the condition $\not{E}_T < 10$ GeV and E_T^W ($\not{E}_T$ without muon correction) $<$25 GeV. In the case of e+jets, ε_{bkg} is measured on a sample enriched by fake electrons. This sample is obtained by requiring the EM object to match a trigger EM object within $|\Delta\varphi| < 0.4$, $|\Delta\eta| < 0.4$, and also requesting at least one jet back-to-back with the EM object ($|\Delta\varphi(EM, jet)| > 2.5$) with low fraction of EM energy component ($f_{EM} < 0.7$) with at least five tracks inside a $\Delta R < 0.5$ cone around the jet axis. ε_{bkg} is determined from a fit to a constant at low values of ${\not{E}_T}^{cal}$.

	W+1jet	W+2jets	W+3jets	W+$\geq$4jets
ε_{sig}	0.876±0.010			
ε_{bkg}, v8-11	0.078±0.001	0.074±0.002	0.080±0.005	0.074±0.010
ε_{bkg}, v12	0.127±0.005	0.120±0.007	0.139±0.016	0.108±0.034

Table 7.4: Probabilities to go from loose to tight definition for electrons from W and non-W background.

	W+1jet	W+2jets	W+3jets	W+$\geq$4jets
ε_{sig}	0.866±0.008	0.850±0.007	0.835±0.011	0.819±0.018
ε_{bkg}	0.097±0.007	0.090±0.008	0.082±0.015	0.075±0.023

Table 7.5: Probabilities to go from loose to tight definition for muons from W and non-W background.

Due to change of the EM trigger algorithm between different trigger versions, ε_{bkg} has changed. The latest EM trigger does a better job in selecting real electrons, and thus steals separation power from the off-line algorithm. Therefore ε_{bkg} has to be determined separately for these two trigger versions (denoted v8-11 and v12 after trigger version numbers). ε_{sig} is found to be unaffected by this change.

The values of ε_{sig} and ε_{bkg} for both channels are brought together in Tables 7.4, 7.5.

7.4 Probability to tag a non-W event

The probability to tag a non-W event $\bar{P}_i^{bkg\ tag}$ is determined only for the e+jets channel. It is calculated as average probability to tag an event which passed all signal loose preselection cuts plus inverted EM likelihood cut ($lh < lh_{cut}$). It does not depend significantly on the likelihood cut value (Fig. 7.1) because most of events have

	W+1jet	W+2jets	W+3jets	W+$\geq$4jets
$\bar{P}_i^{bkg\ tag}$	2.53±0.49	5.46±0.77	2.62±0.56	1.09±0.36
matrix method	2.60±1.65	5.21±1.58	3.07±1.42	0.94±0.90

Table 7.6: The number of non-W events in the tagged e+jets sample calculated using average event tagging probability and from the matrix method on tagged events.

lh close to either 0 or 1. The values of the number of tagged non-W events computed using $\bar{P}_i^{bkg\ tag}$ at $lh_{cut} = 0.5$ are compared to those obtained using matrix method on tagged events. The results are consistent as it is shown in Table 7.6.

7.5 Fractions of W+jets events with particular heavy flavor configuration

The W+jets samples of events with particular parton configurations listed in Table 6.1 have to be further re-arranged in groups of particular jet flavor combinations. This must be done in order to avoid situations when a light jet acquires a b- or c-flavor due to emission of heavy flavor quarks implemented in the PYTHIA fragmentation model. As these cases are already taken into account by ALPGEN, this leads to double-counting (overestimation of fraction of events with heavy flavored jets).

The W+jets events are classified based on the number of heavy flavor (b- or c-) jets according to the following scheme:

- W+light jets: events without b- or c-jets;

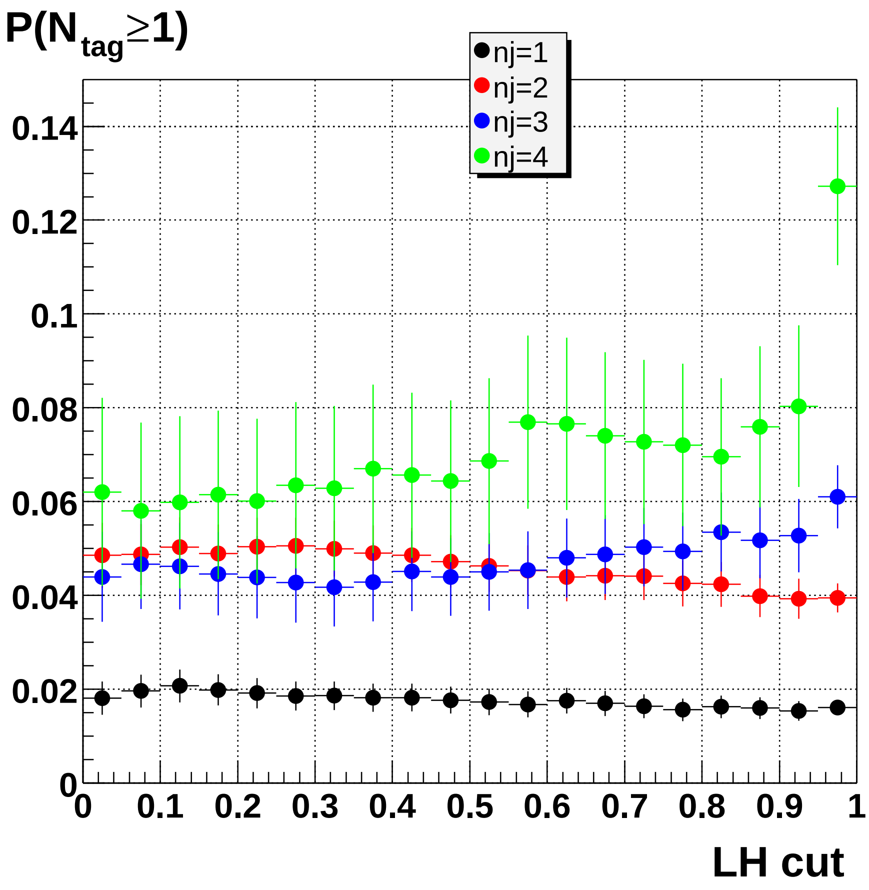

Figure 7.1: An average probability to tag a non-W e+jets event as a function of the likelihood upper cut for different jet multiplicities.

- Wc: events with one c-jet due to single c-production;
- $W(cc)$: events with one c-jet due to double c-production where two c-quarks ended up in the same jet or one of c-jets went out of acceptance;
- Wcc: events with two c-jets (and possibly a third c-jet);
- $W(bb)$: events with one b-jet (there is no single b production, so all of these events are due to double b-production where two b-quarks ended up in the same jet or one of b-jets went out of acceptance);
- Wbb: events with two b-jets (and possibly a c-jet).

The fractions of events from these categories in each of the jet multiplicity bin are shown in Tables 7.7, 7.8. The events which went to these tables have passed all selection criteria, and also were weighted according to the trigger efficiency and (in the case of μ+jets) muon ID efficiency. Therefore, the numbers are slightly different for the e+jets and μ+jets channels. The quoted errors are due to limited Monte Carlo statistics only.

	W+1jet	W+2jets	W+3jets	W+≥4jets
W+light	93.7±2.8	87.8±2.8	83.7±3.4	82.5±2.5
$W(c\bar{c})$	1.10±0.05	2.27±0.08	3.78±0.22	4.5±1.5
$W(b\bar{b})$	0.69±0.02	1.23±0.04	1.98±0.08	2.23±0.75
Wc	4.50±0.17	6.77±0.27	7.13±0.36	5.25±0.35
$Wc\bar{c}$		1.11±0.08	2.08±0.16	3.39±0.46
$Wb\bar{b}$		0.87±0.05	1.32±0.09	2.18±0.17

Table 7.7: Fractions of different W+jets flavor subprocesses (%) contributing to each jet multiplicity bin in e+jets channel.

	W+1jet	W+2jets	W+3jets	W+≥4jets
W+light	93.6±3.1	87.8±2.8	84.8±3.2	83.3±2.3
$W(c\bar{c})$	1.03±0.05	2.22±0.08	3.75±0.21	3.7±1.3
$W(b\bar{b})$	0.65±0.03	1.19±0.04	1.75±0.07	1.86±0.67
Wc	4.71±0.19	6.99±0.27	6.26±0.31	5.26±0.33
$Wc\bar{c}$		1.00±0.08	1.95±0.14	3.30±0.42
$Wb\bar{b}$		0.81±0.04	1.52±0.09	2.54±0.17

Table 7.8: Fractions of different W+jets flavor subprocesses (%) contributing to each jet multiplicity bin in μ+jets channel.

7.6 Probability to tag a W-event

The probability $P_n^{j\ tag}(t)$ to have t tagged jets in a W+$n$jets event with jet flavor configuration $j = \{J_1, \ldots, J_n\}$ is evaluated as

$$\begin{aligned} P_n^{j\ tag}(t \geq 1) &= 1 - \prod_{k=1}^{n} (1 - \varepsilon_{J_k}(E_{Tk}, \eta_k)) \\ P_n^{j\ tag}(t = 1) &= \sum_{m=1}^{n} \varepsilon_{J_m}(E_{Tm}, \eta_m) \prod_{k \neq m} (1 - \varepsilon_{J_k}(E_{Tk}, \eta_k)) \\ P_n^{j\ tag}(t \geq 2) &= P_n^{j\ tag}(t \geq 1) - P_n^{j\ tag}(t = 1), \end{aligned} \tag{7.3}$$

where ε_J, $J = l, c, b$ are probabilities to tag a light, c, or b-jet, respectively, parameterized as functions of jet E_T and η. The average W+$n$jets event tagging probability $\bar{P}_n^{j\ tag}$ is then obtained by averaging $P_n^{j\ tag}$ over all events in the respective Monte Carlo sample. The trigger bias is taken into account by weighting each event by the trigger efficiency ε_i^{trig}:

$$\bar{P}_n^{j\ tag} = \frac{\left\langle P_n^{j\ tag} \varepsilon_i^{trig} \right\rangle}{\left\langle \varepsilon_i^{trig} \right\rangle}. \tag{7.4}$$

In the case of μ+jets, each event is additionally weighted with muon ID efficiency as it depends on muon η.

The calculated event tagging probabilities are put together in Tables 7.9, 7.12.

7.7 Probability to tag a $t\bar{t}$ event

The average probability to tag a $t\bar{t}$ event $P_n^{t\bar{t}\ tag}(t)$ is calculated in the same way as for W+$n$jets events. Here it must be mentioned that although the preselection is aimed at measurement of $t\bar{t} \to l$+jets, an alternative channel, $t\bar{t}\to$dileptons, is also detected (but with much lower efficiency due to the second lepton veto). If accompanied by extra jets, this channel contributes to the third and even forth jet multiplicity bin. As a consequence, $\varepsilon_i^{t\bar{t}} BR(t\bar{t} \to l+\text{jets})$ in Eq. 6.7 has to be replaced by

$$\varepsilon_i^{t\bar{t}\to l+\text{jets}} BR(t\bar{t} \to l+\text{jets}) + \varepsilon_i^{t\bar{t}\to ll} BR(t\bar{t} \to ll), \tag{7.5}$$

and two sets of probabilities have to be calculated: one for $t\bar{t} \to l$+jets and another one for $t\bar{t}\to$dileptons. Both probabilities are rather high since they are determined by a presence of two b-jets. The calculated event tagging probabilities are put together in Tables 7.10, 7.13.

7.8 Other backgrounds and their tagging probabilities

In addition to the dominant background processes (W+jets and non-W events) discussed so far there are other processes which contribution is much smaller than from those two. These processes include:

- single top quark production;
- W/Z pair production;
- $Z \rightarrow \tau^+\tau^-$;
- Z+jets.

Z+jets are very much suppressed with respect to W+jets (there is no physical source of high $\not{E}_T$ in these events). Otherwise these processes are very similar, so all effects due to presence of Z+jets events are already taken into account by considering the W+jets background.

Other mentioned backgrounds are subtracted from the sample based on their theoretical cross sections and average event tagging probabilities. In other words, the numbers of observed events before and after tagging, N_i and N_i^{tag}, are replaced by

$$\begin{aligned} N_i &\rightarrow N_i - \textstyle\sum_b \sigma_b \, \mathcal{L} \, \varepsilon_i^{b\ sel} \\ N_i^{tag} &\rightarrow N_i^{tag} - \textstyle\sum_b \sigma_b \, \mathcal{L} \, \varepsilon_i^{b\ sel} \overline{P}_i^{b\ tag}, \end{aligned} \tag{7.6}$$

where $\mathcal{L}$ is integrated luminosity, $\varepsilon_i^{b\ sel}$ are event selection efficiencies of background processes, $\overline{P}_i^{b\ tag}$ are relevant average event tagging probabilities, and the sum is taken over all background processes. The accuracy with which the cross sections are known does not affect the final result due to very small contribution from these processes.

	e+jets				μ+jets			
	W+1jet	W+2jets	W+3jets	W+≥4jets	W+1jet	W+2jets	W+3jets	W+≥4jets
W+light	0.67±0.03	1.18±0.04	1.82±0.06	2.56±0.06	0.82±0.04	1.39±0.05	2.02±0.07	2.67±0.06
$W(c\bar{c})$	8.2±0.6	7.6±0.3	7.6±0.6	6.8±3.2	8.8±0.8	7.8±0.3	8.1±0.6	6.9±2.8
$W(b\bar{b})$	34.3±1.8	31.5±1.1	31.4±1.2	33.1±9.5	35.5±2.5	31.8±1.2	31.7±1.3	28.0±10.3
Wc	8.1±0.5	8.1±0.4	9.0±0.5	9.8±0.7	8.9±0.6	8.7±0.4	8.9±0.5	9.8±0.7
$Wc\bar{c}$		13.7±1.0	14.0±0.9	14.0±2.2		14.4±1.2	14.2±1.0	14.4±2.2
$Wb\bar{b}$		43.1±2.7	42.4±3.0	42.7±3.8		43.7±3.1	42.6±2.7	42.2±3.2
W+jets	1.32±0.04	2.69±0.05	3.97±0.08	5.1±0.2	1.50±0.05	2.89±0.06	4.07±0.09	5.1±0.2

Table 7.9: Probabilities (%) for 1 tag in W+jets events after matching and full preselection.

	e+jets				μ+jets			
	W+1jet	W+2jets	W+3jets	W+≥4jets	W+1jet	W+2jets	W+3jets	W+≥4jets
$t\bar{t} \to l$+jets	28.6±5.1	42.1±1.9	44.9±1.0	45.8±0.7	31.0±7.1	40.8±2.0	44.2±1.0	45.4±0.8
$t\bar{t} \to ll$	41.2±1.4	46.0±0.8	46.2±1.0	46.1±1.6	40.6±1.5	46.0±0.8	46.1±1.0	46.0±1.7

Table 7.10: Probabilities (%) for 1 tag in $t\bar{t}$ events after matching and full preselection.

The average event tagging probabilities for events from single top quark production in t- and s-channels, W/Z pair production, and $Z \to \tau^+\tau^-$ are listed in Tables 7.11, 7.14.

	e+jets				μ+jets			
	W+1jet	W+2jets	W+3jets	W+≥4jets	W+1jet	W+2jets	W+3jets	W+≥4jets
tb	38.1±0.9	45.5±0.6	45.2±1.0	45.2±2.1	38.0±0.9	45.3±0.6	45.6±1.1	45.0±2.3
tqb	31.4±0.7	36.9±0.5	39.7±0.8	41.7±1.3	31.4±0.7	36.7±0.6	39.5±0.8	41.1±1.3
$WW \to l\nu$jj	2.93±0.10	4.59±0.11	4.6±0.3	4.6±0.8	3.85±0.13	4.58±0.11	4.9±0.3	4.6±0.7
$WZ \to l\nu$jj	12.9±0.5	14.3±0.4	15.0±0.9	9.7±1.7	12.4±0.5	12.2±0.3	9.8±0.5	13.9±2.2
$WZ \to$jjll	3.9±0.5	4.9±0.4	5.1±0.6	6.9±1.5	3.05±0.11	4.35±0.11	4.9±0.3	3.5±0.6
$ZZ \to$jjll	14.3±1.5	18.5±1.3	16.0±1.5	14.2±2.7	14.4±0.7	13.9±0.4	14.9±0.8	14.5±2.1
$Z \to \tau^+\tau^-$	1.73±0.10	2.5±0.2	6.9±1.9	2.1±0.8	1.85±0.09	1.97±0.14	3.0±0.4	3.9±1.6

Table 7.11: Probabilities (%) for 1 tag in background events after matching and full preselection.

	e+jets			μ+jets		
	W+2jets	W+3jets	W+≥4jets	W+2jets	W+3jets	W+≥4jets
W+light	<0.01	0.01±0.01	0.03±0.01	<0.01	0.01±0.01	0.03±0.01
$W(c\bar{c})$	0.05±0.01	0.09±0.01	0.09±0.04	0.05±0.01	0.11±0.01	0.07±0.03
$W(b\bar{b})$	0.32±0.01	0.59±0.02	1.2±0.3	0.39±0.01	0.63±0.03	0.25±0.09
Wc	0.04±0.01	0.10±0.01	0.16±0.01	0.05±0.01	0.10±0.01	0.15±0.01
$Wc\bar{c}$	0.57±0.04	0.65±0.04	0.71±0.11	0.62±0.05	0.69±0.05	0.76±0.12
$Wb\bar{b}$	10.4±0.6	10.0±0.7	10.6±0.9	10.5±0.7	10.6±0.7	10.1±0.8
W+jets	0.11±0.01	0.19±0.01	0.31±0.02	0.11±0.01	0.21±0.01	0.32±0.02

Table 7.12: Probabilities (%) for ≥2 tags in W+jets events after matching and full preselection.

	e+jets			μ+jets		
	W+2jets	W+3jets	W+≥4jets	W+2jets	W+3jets	W+≥4jets
$tt \rightarrow l$+jets	6.4±0.3	12.2±0.3	15.5±0.3	5.9±0.3	11.5±0.3	15.1±0.2
$t\bar{t} \rightarrow ll$	12.1±0.2	13.2±0.3	14.0±0.5	12.1±0.2	13.0±0.3	13.5±0.5

Table 7.13: Probabilities (%) for ≥2 tags in $t\bar{t}$ events after matching and full preselection.

	e+jets			μ+jets		
	W+2jets	W+3jets	W+≥4jets	W+2jets	W+3jets	W+≥4jets
tb	12.4±0.2	12.6±0.3	12.6±0.6	12.1±0.2	12.6±0.3	12.7±0.6
tqb	1.54±0.02	5.79±0.11	8.4±0.3	1.49±0.02	5.50±0.11	8.1±0.3
$WW \rightarrow l\nu$jj	0.02±0.01	0.03±0.01	0.08±0.01	0.02±0.01	0.04±0.01	0.04±0.01
$WZ \rightarrow l\nu$jj	2.73±0.07	3.1±0.2	1.5±0.3	2.33±0.05	1.66±0.09	2.8±0.4
$WZ \rightarrow$jjll	0.03±0.01	0.06±0.01	0.09±0.02	0.02±0.01	0.04±0.01	0.03±0.01
$ZZ \rightarrow$jjll	3.1±0.2	3.0±0.3	2.9±0.6	2.59±0.07	3.2±0.2	2.6±0.4
$Z \rightarrow \tau^+\tau^-$	0.35±0.03	1.7±0.5	0.01±0.01	<0.01	0.19±0.03	0.06±0.02

Table 7.14: Probabilities (%) for ≥2 tags in background events after matching and full preselection.

7.9 Sources of systematic uncertainties

Factors contributing to the systematic error of the $t\bar{t}$ cross section measurement can be separated into two categories:

- uncertainties on the event preselection efficiency,
- uncertainties on the event tagging probability.

In addition, there is uncertainty for the QCD background evaluation. Uncertainties due to jet energy scale, jet energy resolution, jet ID, and top quark mass affect both preselection efficiency and event tagging probability. The systematic uncertainties changing the preselection efficiency are applied to signal, and those on the event tagging probability are applied to both signal and background.

Statistically, there are effects which are considered fully uncorrelated between e+jets and μ+jets channels and which are fully correlated. In case when uncertainties are uncorrelated between the channels, their effect on the combined cross section is estimated separately for the e+jets and μ+jets case and resulting values are added in quadrature, so that the error on the combined cross section can be smaller than uncertainties for the individual channels. In the case of correlated errors, the effect is in between the values for the individual channels.

The following sources of systematic errors have been considered:

- Jet energy scale.

The uncertainty on the jet energy scale is obtained by varying the jet energy scale correction by 1σ, where σ is taken to be

$$\sigma = \sqrt{\sigma^2_{stat,\ data} + \sigma^2_{syst,\ data} + \sigma^2_{stat,\ MC} + \sigma^2_{syst,\ MC}}. \tag{7.7}$$

The effect on both preselection efficiency and event tagging probability is estimated simultaneously.

- Jet energy resolution.

  This uncertainty is calculated by varying the jet energy by 1σ of the jet energy resolution.

- Jet ID.

  The uncertainty on the jet identification is obtained as difference between jet reconstruction and identification efficiency in data and Monte Carlo.

- Top quark mass.

  The uncertainty on the top quark mass is determined as difference with respect to results obtained for a top quark mass 170 GeV and 180 GeV (so it assumes a ±5 GeV top quark mass variation). This requires Monte Carlo samples generated assuming a different top quark mass. Because these samples are statistically independent, the uncertainty is calculated as an interpolation of preselection efficiencies and event tagging probabilities for five top quark mass points (160, 170, 175, 180, and 190 GeV) and then evaluated at 170 GeV and 180 GeV.

- Trigger efficiency.

  The uncertainty on the trigger efficiency is estimated by varying the efficiency parameterization by 1σ, where σ is obtained by adding in quadrature variations for trigger efficiencies at Levels 1, 2, 3 for jets, EM (e+jets), and muons (μ+jets).

- Primary vertex selection efficiency.

  This uncertainty is calculated from the statistical uncertainty on the efficiency measured in the preselected sample without applying the cuts on the electron likelihood and z of the electron (e+jets), or the DCA significance and z of the muon (μ+jets).

- Lepton preselection efficiency.

  Uncertainties on the $t\bar{t}$ preselection efficiency specific to the channel are listed below.

  Sources of systematic uncertainties specific to e+jets:

  - EM reconstruction,

  - EM ID,
  - EM track efficiency,
  - EM likelihood,
  - cut on z of an electron track with respect to the primary vertex.

  Sources of systematic uncertainties specific to μ+jets:

  - muon track efficiency,
  - muon ID,
  - muon isolation,
  - cuts on muon track parameters (DCA significance, z with respect to the primary vertex, track fit χ^2).

- Matrix method.

  The uncertainty on the matrix method is obtained by varying ε_{sig} and ε_{bkg} by one standard deviation. The results of the two variations are added in quadrature. The errors are assumed to be totally uncorrelated between the channels.

- Tagging probability in Monte Carlo.

  The uncertainty on the tagging probability in Monte Carlo is taken from the statistical error of the two-dimensional parameterization due to the finite Monte Carlo statistics.

- Taggability in data.

  The uncertainty on the taggability in data is taken from the statistical error of the two-dimensional parameterization. In addition, a 5% absolute error is assigned as derived from the difference between e+jets and μ+jets taggability normalization factors.

- Flavor dependence of taggability.

  The uncertainty on the flavor dependence of the taggability is derived from the difference between flavor dependence obtained on QCD and W+jets Monte Carlo samples.

- Model dependence of tagging probability.

  This uncertainty is calculated by replacing the Monte Carlo parameterizations derived on $t\bar{t}$ samples with those derived on $Z \rightarrow b\bar{b}/c\bar{c}$. The b-tagging inclusive efficiency, c-tagging inclusive efficiency, and b-tagging semileptonic efficiency (contributing to the data/Monte Carlo scale factor) are modified simultaneously.

- b-tagging efficiency in data.

  The uncertainty on the b-tagging efficiency on data is derived from the systematic error obtained for System 8 method. The major contributions are uncertainties due to assumption of decorrelation of CSIP and SLT taggers

(κ_b) and decorrelation between tagging probabilities for two *b*-jets (β). Both factors have been evaluated on $Z \to b\bar{b} \to \mu$ Monte Carlo and found to be κ_b =0.98±0.02 and β =1.02±0.02. This uncertainties are propagated to the event tagging probabilities.

- Negative tag rate function.

  The uncertainty on the negative tag rate function is derived from the systematic error which is estimated from the difference on the negative tag rate function obtained on two samples with different trigger requirements.

- Scale factors SF_{ll} and SF_{HF}.

  The uncertainty on the light scale factor $SF_l = SF_{ll} \times SF_{HF}$ is obtained from the fit error resulting from the limited Monte Carlo statistics.

- Difference between SF_b and SF_c.

  An estimation based on the difference in the average number of tracks per jet suggests that the SF_c/SF_b can be as low as 0.84. This difference is introduced as a (one-sided) systematic error on the *c*-tagging efficiency and propagated to the event tagging probabilities.

- W+jets fractions.

  The uncertainty on W+jets fractions is arising from the limited Monte Carlo statistics. The statistical errors on the fractions of events with different jet flavor composition are shown in Tables 7.7, 7.8. For less likely flavor signatures (e.g. $W(bb)$) this uncertainty can be quite large.

Chapter 8

The result

8.1 Observed tag rates in the lepton+jets sample

The expected number of signal and background events (including their statistical and systematic uncertainties) assuming $\sigma_{t\bar{t}}$ =7 pb and the number of tagged events observed in the lepton+jets date sample are summarized in Tables 8.1, 8.2 and Figs. 8.1, 8.2. The actual number of tagged events is in a good agreement with the prediction. In the control bins (n_j =1, 2) with small contribution from the $t\bar{t}$ signal, this agreement suggests that the method is capable of accurately predicting the background. The agreement in the signal bins (n_j =3, $\geq$4) implies that actual $t\bar{t}$ cross section is close to the value predicted by the theory.

	e+jets				μ+jets			
	1jet	2jets	3jets	≥4jets	1jet	2jets	3jets	≥4jets
W+light	38.4±1.7	22.5±0.9	7.6±0.5	2.6±0.3	37.4±2.0	23.3±1.0	7.6±0.5	1.7±0.3
$W(c\bar{c})$	5.6±0.4	3.09±0.15	0.95±0.09	0.3±0.2	4.5±0.4	2.76±0.14	0.97±0.09	0.19±0.08
$W(b\bar{b})$	14.5±0.8	8.2±0.3	2.9±0.2	0.8±0.3	10.9±0.8	7.0±0.3	2.2±0.2	0.4±0.2
Wc	22.5±1.3	11.9±0.6	3.2±0.2	0.64±0.09	20.5±1.5	11.5±0.6	2.5±0.2	0.39±0.07
$Wc\bar{c}$		4.5±0.3	2.3±0.2	0.61±0.12		3.8±0.3	1.9±0.2	0.35±0.08
$Wb\bar{b}$		8.3±0.6	2.8±0.3	1.1±0.2		6.8±0.5	2.9±0.2	0.81±0.14
W+jets	81.0±2.3	58.6±1.3	19.6±0.7	6.2±0.5	73.2±2.7	55.2±1.4	18.0±0.7	3.9±0.4
QCD	2.6±1.7	5.2±1.5	3.0±1.4	0.8±0.8	5.9±1.8	4.2±1.5	2.0±1.1	1.0±0.7
tb	0.23±0.01	1.01±0.01	0.34±0.01	0.08±0.01	0.17±0.01	0.83±0.01	0.29±0.01	0.06±0.01
tqb	0.41±0.01	1.46±0.02	0.89±0.02	0.36±0.01	0.33±0.01	1.16±0.02	0.75±0.02	0.32±0.01
$t\bar{t} \to ll$	0.68±0.02	3.53±0.06	2.26±0.05	0.79±0.03	0.50±0.02	2.81±0.05	2.04±0.04	0.71±0.03
$WW \to l\nu jj$	0.25±0.01	1.03±0.03	0.16±0.01	0.02±0.01	0.28±0.01	0.98±0.02	0.17±0.01	0.02±0.01
$WZ \to l\nu jj$	0.31±0.01	0.95±0.02	0.17±0.01	0.01±0.01	0.26±0.01	0.83±0.02	0.13±0.01	0.02±0.01
$WZ \to jjll$	<0.01	<0.01	<0.01	<0.01	0.02±0.01	0.07±0.01	0.02±0.01	<0.01
$ZZ \to jjll$	<0.01	0.04±0.01	0.02±0.01	<0.01	0.05±0.01	0.16±0.01	0.05±0.01	<0.01
$Z \to \tau^+\tau^-$	0.22±0.01	0.24±0.02	0.08±0.02	0.02±0.01	0.42±0.02	0.32±0.02	0.18±0.02	0.03±0.01
background	85.7±2.8	72.0±2.0	26.5±1.5	8.3±1.0	81.1±3.2	66.5±2.1	23.6±1.3	6.1±0.8
syst.	+7.2-8.0	+5.1-5.5	±2.3	±1.1	+6.6-7.5	+4.8-5.4	±2.0	+0.9-1.0
$t\bar{t} \to l$+jets	0.07±0.01	1.72±0.08	7.7±0.2	14.4±0.2	0.04±0.01	1.23±0.06	6.25±0.15	13.1±0.2
total	85.8±2.8	73.7±2.0	34.2±1.5	22.7±1.0	81.1±3.2	67.8±2.1	29.9±1.3	19.2±0.8
syst.	+7.3-8.0	+5.3-5.7	+2.4-2.6	+1.9-3.3	+6.6-7.6	+5.0-5.5	±2.2	+1.7-2.9
tags	101	79	39	29	80	65	36	15

Table 8.1: Summary of observed and predicted number of events with 1 tag.

	e+jets			μ+jets		
	2jets	3jets	≥4jets	2jets	3jets	≥4jets
W+light	0.08±0.01	0.05±0.01	0.03±0.01	0.09±0.01	0.06±0.01	0.02±0.01
$W(c\bar{c})$	0.02±0.01	0.01±0.01	<0.01	0.02±0.01	0.01±0.01	<0.01
$W(b\bar{b})$	0.08±0.01	0.05±0.01	0.03±0.01	0.09±0.01	0.04±0.01	<0.01
Wc	0.06±0.01	0.04±0.01	0.01±0.01	0.06±0.01	0.03±0.01	<0.01
$Wc\bar{c}$	0.19±0.01	0.11±0.01	0.03±0.01	0.16±0.01	0.09±0.01	0.02±0.01
$Wb\bar{b}$	2.01±0.13	0.66±0.06	0.27±0.04	1.64±0.12	0.71±0.06	0.19±0.03
W+jets	2.45±0.14	0.92±0.06	0.38±0.04	2.07±0.12	0.95±0.06	0.25±0.03
QCD	0.0±0.4	0.1±0.4	0.2±0.4	-0.1±0.3	-0.1±0.2	0.0±0.2
tb	0.27±0.01	0.10±0.01	0.02±0.01	0.22±0.01	0.08±0.01	0.02±0.01
tqb	0.06±0.01	0.13±0.01	0.07±0.01	0.05±0.01	0.10±0.01	0.06±0.01
$t\bar{t} \to ll$	0.92±0.02	0.65±0.01	0.24±0.01	0.74±0.01	0.58±0.01	0.21±0.01
$WW \to l\nu jj$	<0.01	<0.01	<0.01	<0.01	<0.01	<0.01
$WZ \to l\nu jj$	0.18±0.01	0.03±0.01	<0.01	0.16±0.01	0.02±0.01	<0.01
$WZ \to jjll$	<0.01	<0.01	<0.01	<0.01	<0.01	<0.01
$ZZ \to jjll$	<0.01	<0.01	<0.01	0.03±0.01	0.01±0.01	<0.01
$Z \to \tau^+\tau^-$	0.03±0.01	0.02±0.01	<0.01	<0.01	0.01±0.01	<0.01
background	3.9±0.4	2.0±0.4	0.9±0.4	3.2±0.4	1.7±0.3	0.6±0.2
syst.	±0.7	±0.4	±0.4	±0.6	±0.3	±0.3
$t\bar{t} \to l$+jets	0.26±0.01	2.08±0.05	4.88±0.08	0.18±0.01	1.62±0.04	4.36±0.07
total	4.2±0.4	4.0±0.4	5.8±0.4	3.4±0.4	3.3±0.3	4.9±0.3
syst.	±0.9	±0.9	+1.3-1.5	+0.8-0.7	±0.7	+1.1-1.3
tags	6	4	5	5	3	3

Table 8.2: Summary of observed and predicted number of events with ≥2 tags.

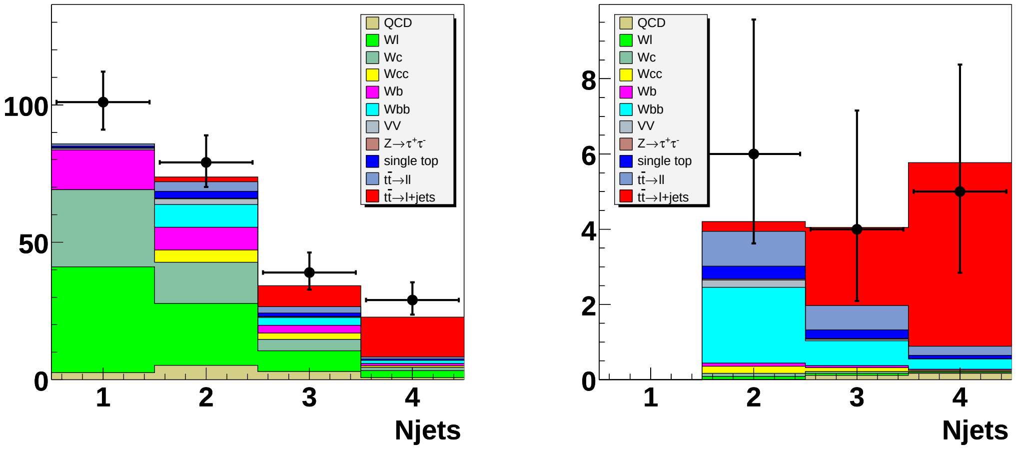

Figure 8.1: Summary plot of observed (dots) and predicted events with 1 (left) and ≥ 2 (right) tags in the e+jets channel.

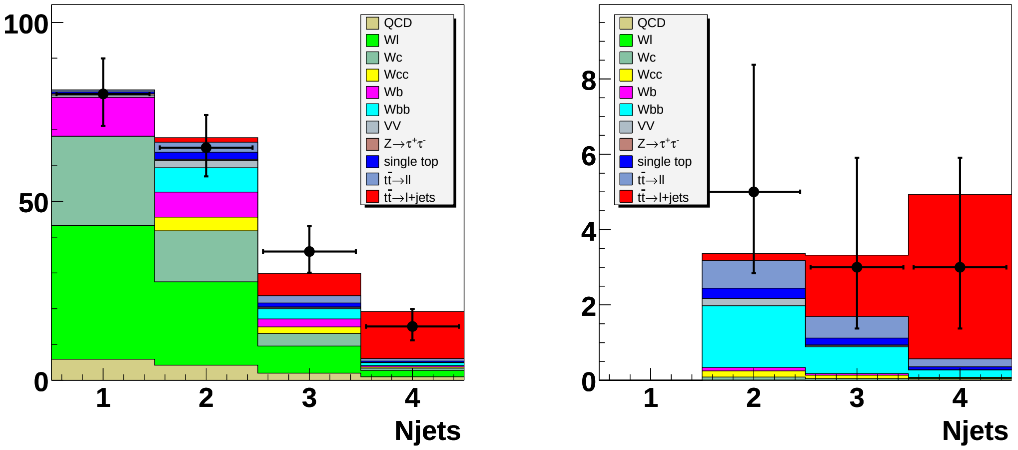

Figure 8.2: Summary plot of observed (dots) and predicted events with 1 (left) and ≥ 2 (right) tags in the μ+jets channel.

8.2 The cross section

The $t\bar{t}$ production cross section is estimated by using the likelihood method. For each individual channel, four bins are considered (single- and double-tagged events in the $n_j = 3$ and $n_j \geq 4$ jet multiplicity bins).

The likelihood function used to obtain the statistical uncertainty on the cross section is shown in Fig. 8.3. The summary of systematic uncertainties in the cross section for each lepton+jets channel and the combination is given in Table 8.3. The dominating systematic uncertainties originate from the jet energy scale and measurement of the *b*-tagging efficiency in data.

The result for each individual channel is:

$$\begin{aligned} \mathrm{e+jets} &: \quad \sigma_{t\bar{t}} = 9.08^{+1.80}_{-1.64}\,(\mathrm{stat})\,^{+1.95}_{-1.15}\,(\mathrm{syst})\,\pm 0.59\,(\mathrm{lumi})\,\mathrm{pb}; \\ \mu\mathrm{+jets} &: \quad \sigma_{t\bar{t}} = 5.57^{+1.68}_{-1.48}\,(\mathrm{stat})\,^{+1.39}_{-0.93}\,(\mathrm{syst})\,\pm 0.36\,(\mathrm{lumi})\,\mathrm{pb}; \end{aligned}$$

and for the combination:

$$\mathrm{lepton+jets} : \quad \sigma_{t\bar{t}} = 7.47^{+1.22}_{-1.14}\,(\mathrm{stat})\,^{+1.65}_{-1.03}\,(\mathrm{syst})\,\pm 0.49\,(\mathrm{lumi})\,\mathrm{pb}.$$

	e+jets	μ+jets	combined
Jet energy scale	-0.478+1.534	-0.453+0.995	-0.474+1.246
Jet energy resolution	-0.051	-0.075+0.046	-0.068+0.017
Jet ID	+0.522	+0.477	+0.500
Top mass	-0.137+0.184	-0.087+0.116	-0.114+0.153
EM L1 Trigger	-0.007		+0.004
EM L3 Trigger	$<$0.002		$<$0.002
Muon L1 Trigger		+0.017-0.022	+0.008-0.010
Muon L2 Trigger		+0.005-0.011	+0.002-0.005
Jet L1 Trigger	+0.012-0.019	+0.006-0.012	+0.007-0.012
Jet L2 Trigger	$<$0.002	$<$0.002	$<$0.002
Jet L3 Trigger	+0.023-0.095	+0.035-0.131	+0.021-0.081
Primary vertex selection efficiency	$\mp$0.081	$\mp$0.102	$\mp$0.076
Lepton preselection efficiency	$\mp$0.153	$\mp$0.228	$\mp$0.167
Matrix method, ε_{sig}	$\mp$0.013	$\mp$0.012	$\mp$0.009
Matrix method, ε_{bkg}	$\mp$0.005	$\mp$0.065	$\mp$0.026
b-tagging probability in MC	$\mp$0.054	$\mp$0.040	$\mp$0.034
c-tagging probability in MC	$\mp$0.075	$\mp$0.064	$\mp$0.051
Semileptonic b-tagging probability in MC	$\pm$0.301	$\pm$0.223	$\pm$0.187
Taggability in data	-0.089	-0.038	-0.046
Flavor dependence of taggability	-0.022	-0.017	-0.019
Decay model dependence of P^{tag}	+0.168	+0.121	+0.147
b-tagging efficiency in data	$\mp$0.925	$\mp$0.676	$\mp$0.815
Negative tag rate function	$\mp$0.180	$\mp$0.186	$\mp$0.185
Light tag scale factors	$\mp$0.040	$\mp$0.042	$\mp$0.041
SF_c/SF_b	+0.261	+0.227	+0.249
W+jets fractions	$\mp$0.202	$\mp$0.132	$\mp$0.171
total	+1.953-1.152	+1.391-0.933	+1.647-1.027

Table 8.3: Summary of systematic uncertainties ($\Delta\sigma_{t\bar{t}}$, pb).

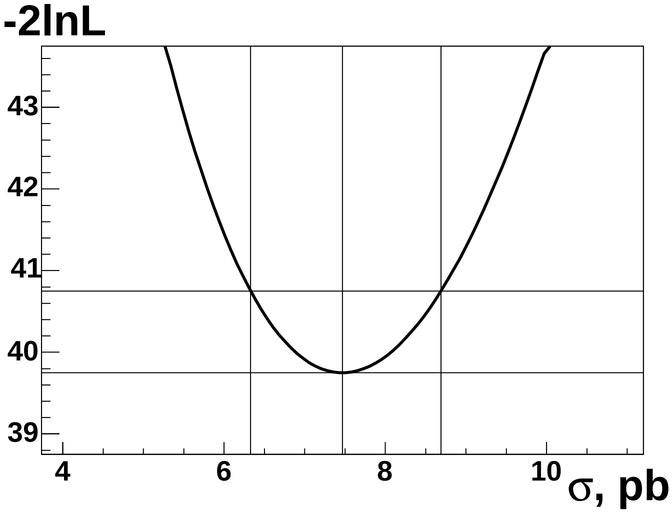

Figure 8.3: Likelihood function used to obtain the statistical uncertainty on the $t\bar{t} \rightarrow l+$jets cross section.

8.3 Cross-checks

In order to cross-check the method, the distributions of various event variables in the actual data sample were compared to the Monte Carlo prediction. Two types of variables have been considered: those proportional to the energy present in the event (*e.g.* sum over all jet transverse energies, $H_T = \sum E_T^j$), and those related to the topological properties of the event. Among the latter, of a special interest are sphericity and aplanarity, calculated as follows. The normalized momentum tensor M is defined as:

$$M_{ij} = \frac{\sum_k p_i^k p_j^k}{\sum_k |p^k|^2}, \tag{8.1}$$

where $\overline{p^k}$ is the momentum of a reconstructed object k (the sum is taken over the jets and a high p_T lepton), i and j are Cartesian coordinates. Given $\lambda_1 \geq \lambda_2 \geq \lambda_3$ are its eigenvalues, the sphericity S is defined as $S = 1.5(\lambda_2 + \lambda_3)$ (0$\leq S \leq$1), and the aplanarity A as $A = 1.5\lambda_3$ (0$\leq A \leq$0.5). The $t\bar{t}$ events are more isotropic as is typical for the decay of a heavy object, and therefore have higher values of S and A.

As an example, Fig. 8.4 shows the comparison plots for the reconstructed transverse W mass and sphericity for the combination of the e+jets and μ+jets channels in the $n_j \geq$4 jet multiplicity bin. The contribution from the $t\bar{t}$ has been normalized to the measured cross section. The observed distributions are in a good agreement with the prediction (for distributions in Fig. 8.4, the Kolmogorov test probability [70] is found to be KT=0.92 and 0.97, respectively).

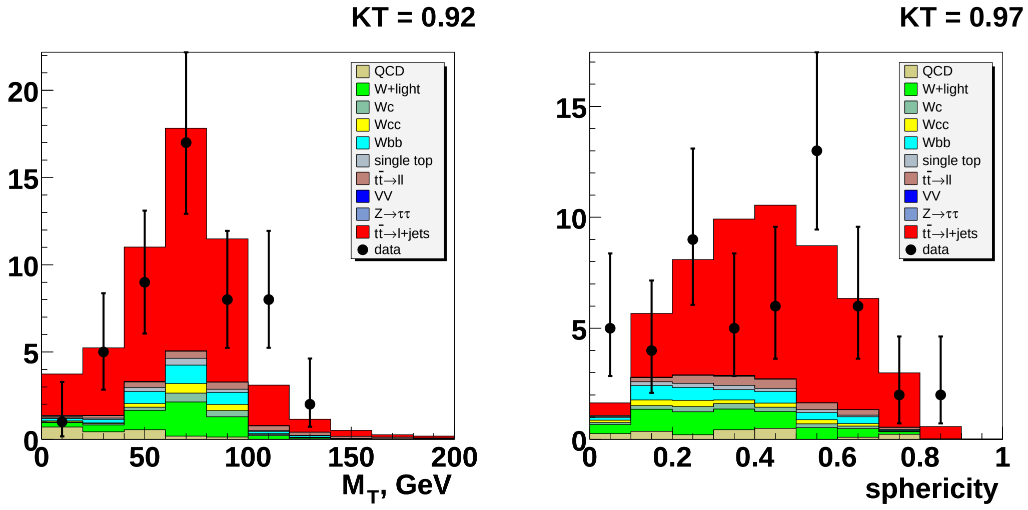

Figure 8.4: Distribution of transverse W mass (left) and sphericity (right) for the tagged lepton+jets sample (dots) and for the Monte Carlo prediction in the $n_j \geq 4$ jet multiplicity bin.

Chapter 9

Conclusion

A measurement of the $t\bar{t}$ production cross section in $p\bar{p}$ collisions at $\sqrt{s} = 1.96$ TeV has been presented. The analysis is based on the application of life-time based Counting Signed Impact Parameter b-tagging algorithm to the lepton+jets preselected samples, corresponding to integrated luminosities of 168.7 pb^{-1} and 158.4 pb^{-1} in the case of the e+jets and μ+jets channels, respectively. The resulting cross section measured in the lepton+jets channel is found to be

$$\sigma_{t\bar{t}} = 7.47^{+1.22}_{-1.14}\,(\mathrm{stat})\,^{+1.65}_{-1.03}\,(\mathrm{syst})\,\pm 0.49\,(\mathrm{lumi})\,\mathrm{pb}.$$

in a good agreement with the Standard Model prediction. This is the first $t\bar{t}$ production cross section measurement in DØ using the b-tagging technique, and one of the first DØ analyses employing *b*-tagging. Many methods have been probed for the first time as the analysis progressed. With the available sample, the statistical error is already comparable with the systematic uncertainty. As the amount of data collected by the Tevatron experiments increases, decreasing the systematic uncertainty becomes a crucial factor. A better understanding of the apparatus and calibration methods will allow to improve the measurement so that even small deviations from the theoretical prediction can be detected, and the Standard Model be further probed in the region it has never been tested before.

In a perspective, the top production studies at the Tevatron are the basis for the future high energy physics projects like Large Hadron Collider at CERN which will essentially be a top factory. There the $t\bar{t}$ production will be both a perfect calibration channel and dominating background to many exciting physic processes, including production of a Higgs boson. The study of these processes may eventually reveal that the Standard Model, which is so well confirmed by many analyses including the one presented in this thesis, is just a modest subset of another great model that answers the most difficult questions on the building principles of the Universe.

Bibliography

[1] S. Weinberg, “A Model Of Leptons,” Phys. Rev. Lett. **19**, 1264 (1967).

[2] A. Salam, “Elementray Particle Physics,” Almquvist and Wiksells, Stockholm (1968).

[3] S. L. Glashow, J. Iliopoulos and L. Maiani, “Weak Interactions With Lepton - Hadron Symmetry,” Phys. Rev. D **2**, 1285 (1970).

[4] M. K. Gaillard, P. D. Grannis and F. J. Sciulli, “The standard model of particle physics,” Rev. Mod. Phys. **71**, S96 (1999) [arXiv:hep-ph/9812285].

[5] M. Kobayashi and T. Maskawa, “CP Violation In The Renormalizable Theory Of Weak Interaction,” Prog. Theor. Phys. **49**, 652 (1973).

[6] S. W. Herb *et al.*, “Observation Of A Dimuon Resonance At 9.5-Gev In 400-Gev Proton - Nucleus Collisions,” Phys. Rev. Lett. **39**, 252 (1977).

[7] D. Schaile and P. M. Zerwas, “Measuring the weak isospin of B quarks,” Phys. Rev. D **45**, 3262 (1992).

[8] G. L. Kane and M. E. Peskin, “A Constraint From B Decay On Models With No T Quark,” Nucl. Phys. B **195**, 29 (1982).

[9] C. Albajar *et al.* [UA1 Collaboration], “Beauty Production At The Cern P Anti-P Collider,” Phys. Lett. B **256**, 121 (1991) [Erratum-ibid. B **262**, 497 (1991)].

[10] J. J. Lodder and H. J. De Blank, “Recalculation of W and Z radiative corrections and a top quark mass estimate,” arXiv:hep-ph/9405264.

[11] C. Rubbia [UA1 Collaboration], “Physics Results Of The Ua1 Collaboration At The Cern Proton - Anti-Proton Collider,” CERN-EP/84-135 *Invited talk given at Int. Conf. on Neutrino Physics and Astrophysics, Dortmund, West Germany, Jun 11-16, 1984*

[12] F. Abe *et al.* [CDF Collaboration], “A Lower limit on the top quark mass from events with two leptons in p anti-p collisions at s**(1/2) = 1.8-TeV,” Phys. Rev. Lett. **68**, 447 (1992).

[13] F. Abe *et al.* [CDF Collaboration], “A Limit on the top quark mass from proton - anti-proton collisions at s**(1/2) = 1.8-TeV,” Phys. Rev. D **45**, 3921 (1992).

[14] F. Abe *et al.* [CDF Collaboration], “Evidence for top quark production in anti-p p collisions at s**(1/2) = 1.8-TeV,” Phys. Rev. Lett. **73**, 225 (1994) [arXiv:hep-ex/9405005].

[15] F. Abe *et al.* [CDF Collaboration], “Observation of top quark production in anti-p p collisions,” Phys. Rev. Lett. **74**, 2626 (1995) [arXiv:hep-ex/9503002].

[16] S. Abachi *et al.* [D0 Collaboration], “Observation of the top quark,” Phys. Rev. Lett. **74**, 2632 (1995)

[17] LHC Study Group, “The Large Hadron Collider : conceptual design,” CERN-AC-95-05 LHC (1995).

[18] P. W. Higgs, “Broken Symmetries, Massless Particles And Gauge Fields,” Phys. Lett. **12**, 132 (1964).

[19] M. Gluck, J. F. Owens and E. Reya, “Gluon Contribution To Hadronic J / Psi Production,” Phys. Rev. D **17**, 2324 (1978).

[20] E. Laenen, J. Smith and W. L. van Neerven, “Top quark production cross-section,” Phys. Lett. B **321**, 254 (1994) [arXiv:hep-ph/9310233].

[21] K. Hagiwara *et al.* [Particle Data Group Collaboration], “Review Of Particle Physics,” Phys. Rev. D **66**, 010001 (2002).

[22] M. Cacciari, S. Frixione, M. L. Mangano, P. Nason and G. Ridolfi, “The t anti-t cross-section at 1.8-TeV and 1.96-TeV: A study of the systematics due to parton densities and scale dependence,” JHEP **0404**, 068 (2004) [arXiv:hep-ph/0303085].

[23] N. Kidonakis and R. Vogt, “Top quark production at the Tevatron at NNLO,” arXiv:hep-ph/0309045.

[24] T. Sjostrand and P. M. Zerwas, “On the interplay between top decay and top fragmentation,” CERN-TH-6313-91 *Presented at the Final Meeting of the Working Groups on E+ E- at 500 GeV, Hamburg, Germany, Sep 2-3, 1991* [arXiv:hep-ex/9503003].

[25] L. M. Lederman, “The Tevatron,” Sci. Am. **264**, 26 (1991).

[26] S. Abachi *et al.* [D0 Collaboration], “The D0 Detector,” Nucl. Instrum. Meth. A **338**, 185 (1994).

[27] S. Prototopescu, “Coordinate System And Units For D0 Software,” http://www-d0online.fnal.gov/www/groups/cap/quick_guide/Coordinate_System.htm

[28] J. Ellison [D0 Collaboration], “The D0 detector upgrade and physics program,” *Prepared for 15th International Workshop on High-Energy Physics and Quantum Field Theory (QFTHEP 2000), Tver, Russia, 14-20 Sep 2000*

[29] R. Yamada, "The Magnetic Design And Field Measurement Of Fermilab Collider Detectors: Cdf And D0,"

[30] B. Squires *et al.*, "Design Of The 2-Tesla Superconducting Solenoid For The Fermilab D0 Detector Upgrade," Adv. Cryog. Eng. **39A**, 301 (1994). FERMILAB-CONF-90-036

[31] D. Hedin [D0 Collaboration], "The D0 muon system and early results on its performance," FERMILAB-CONF-92-305 *Contributed to 26th International Conference on High Energy Physics (ICHEP 92), Dallas, TX, 6-12 Aug 1992*

[32] V. Abramov *et al.*, "Forward Muon System For The D0 Detector Upgrade," Nucl. Instrum. Meth. A **419**, 660 (1998).

[33] A. Askew, "Parametrizing the Local Muon Resolution in p13 Data for PMCS," DØ note 4314 (2003).

[34] J. Christenson [D0 Collaboration], "The D0 Calorimeter: An Overview," *Given at 3rd International Conference on Calorimetry in High-energy Physics, Corpus Christi, TX, 29 Sep - 2 Oct 1992*

[35] L. Groer [D0 Collaboration], "D0 calorimeter upgrades for Tevatron Run II," FERMILAB-CONF-00-322-E *Prepared for 9th Conference on Calorimetry in High Energy Physics (CALOR 2000), Annecy, France, 9-14 Oct 2000*

[36] J. Coss, *et al.*, “Jet Energy Scale and Resolution for p13 Data and Monte Carlo,” DØ note 4115 (2003).

[37] K. Del Signore [D0 Collaboration], “Forward and central preshower detectors for the D0 upgrade,” *Prepared for SCIFI97: Conference on Scintillating and Fiber Detectors, South Bend, Indiana, 2-6 Nov 1997*

[38] The DØ Upgrade Central Fiber Tracker. Tecnical Design Report (1997).

[39] E. Kajfasz [D0 Collaboration], “D0 silicon microstrip tracker for Run IIa,” Nucl. Instrum. Meth. A **511**, 16 (2003) [arXiv:hep-ex/0112014].

[40] D. Adams *et al.* [D0 Collaboration], “VLPC characterization for the D0 upgrade,” arXiv:hep-ex/9410011.

[41] R. Demina, A. Khanov, “Acceptance of SMT for various F-disk options,” DØ note 3730 (2000).

[42] L. Landau, “On the energy loss of fast particles by ionization,” J. Phys. USSR 8 201 (1944).

[43] R. Demina, *et al.*, “Charge distribution in SMT Clusters,” DØ note 3981 (2002).

[44] R. Demina, *et al.*, “Verification of the Lorentz angle value using SMT data,” DØ note 3945 (2002).

[45] M. Roco, “Analysis of SMT Beam Tests Data,” DØ note 3405 (1998).

[46] A. Khanov, “SMT clustering,” report on DØ workshop at Oklakhoma, 10 July 2002.

[47] G. Lutz and A. S. Schwarz, “Silicon Devices For Charged-Particle Track And Vertex Detection,” Ann. Rev. Nucl. Part. Sci. **45**, 295 (1995).

[48] S. M. Sze, “The Physics of Semiconductor Devices,” 2nd edition, Wiley Interscience (1981).

[49] A. Khanov, “HTF: histogramming method for finding tracks. The algorithm description,” DØ note 3778 (2000).

[50] P. V. C. Hough, “Machine Analysis of Bubble Chamber Pictures,” Int. Conf. on High Energy Accelerators and Instrumentation, CERN (1959).

[51] R. Fruhwirth, “Application of Kalman filtering to track and vertex fitting,” Nucl. Instrum. Meth. A **262**, 444 (1987).

[52] D. Alton, *et al.*, “Measurement of $Z \to e^+e^-$ and $W \to e^\pm\nu$ Production Cross Sections at the Tevatron With the DZero Detector,” DØ note 4131 (2003).

[53] R. Demina, *et al.*, “Measurement of b-tagging efficiency and mis-tagging rates with CSIP method,” DØ note 4432 (2004).

[54] A. Schwartzman and M. Narain, “b-quark jet identification via Secondary Vertex Reconstruction,” DØ note 4080 (2003).

[55] R. Demina, A. Khanov, F. Rizatdinova, “b-tagging with Counting Signed Impact Parameter method,” DØ note 4049 (2002).

[56] A. Maciel and A. Sznajder, “Flavor Content Discrimination in a Muon Tagged Jet Sample using PtRel,” DØ note 3704 (1999).

[57] B. Clément *et al.*, “SystemD or how to get signal, backgrounds and their efficiencies with real data,” DØ note 4159 (2003).

[58] B. Abbott *et al.* [D0 Collaboration], “Extraction of the width of the W boson from measurements of sigma(p anti-p → W + X) x B(W → e nu) and sigma(p anti-p → Z + X) x B(Z → e e) and their ratio,” Phys. Rev. D **61**, 072001 (2000) [arXiv:hep-ex/9906025].

[59] L. Mangano, M. Moretti, F. Piccinini, R. Pittau and A. D. Polosa, “ALPGEN, a generator for hard multiparton processes in hadronic collisions,” JHEP **0307**, 001 (2003) [arXiv:hep-ph/0206293].

[60] D. Stump, J. Huston, J. Pumplin, W. K. Tung, H. L. Lai, S. Kuhlmann and J. F. Owens, “Inclusive jet production, parton distributions, and the search for new physics,” JHEP **0310**, 046 (2003) [arXiv:hep-ph/0303013].

[61] T. Sjostrand, L. Lonnblad and S. Mrenna, “PYTHIA 6.2: Physics and manual,” arXiv:hep-ph/0108264.

[62] H. L. Lai *et al.* [CTEQ Collaboration], “Global QCD analysis of parton structure of the nucleon: CTEQ5 parton distributions,” Eur. Phys. J. C **12**, 375 (2000) [arXiv:hep-ph/9903282].

[63] A. Pukhov *et al.*, “CompHEP: A package for evaluation of Feynman diagrams and integration over multi-particle phase space. User’s manual for version 33,” arXiv:hep-ph/9908288.

[64] Top Physics Working Group, “D0 Top Analyses and Data Sample for the Winter Conference 2004,” DØ note 4419.

[65] Mike Hildreth, Avto Kharchilava, “On Minimum bias events,” talk on Matrix Element / Monte Carlo Tuning Workshop at Fermilab, October 2002. http://cepa.fnal.gov/patriot/mc4run2/MCTuning/mcworkshop100402.pdf

[66] J. Womersley [D0 Collaboration], “The D0 Monte Carlo,” FERMILAB-CONF-92-306 *Contributed to 26th International Conference on High Energy Physics (ICHEP 92), Dallas, TX, 6-12 Aug 1992*

[67] Top Physics Working Group, “Measurement of the ttbar Xsec in the lepton+jets channels at sqrt(s) = 1.96 TeV (topological),” DØ note 4422.

[68] Prolay Kumar Mal *et al.*, “D0 Luminosity in Run 2: Reconstructed,” DØ note 4438.

[69] N. Amos, C. Stewart, P. Bhat, C. Cretsinger, E. Won, W. Dharmaratna and H. B. Prosper, “The random grid search: A simple way to find optimal cuts,” *Prepared for International Conference on Computing in High-energy Physics (CHEP 95), Rio de Janeiro, Brazil, 18-22 Sep 1995*

[70] W. T. Eadie, D. Drijard, F. James, M. Roos, and B. Sadoulet, “Statistical Methods in Experimental Physics,”, North-Holland (1971).